Relaxation Processes in Semiconductor Quantum Dots

A thesis submitted for the degree of

Doctor of Philosophy

at the University of Leicester

by

Darren Chaney

Department of Physics and Astronomy

University of Leicester

September 2004

Relaxation Processes in Semiconductor Quantum Dots

by

Darren Chaney

Abstract

In this thesis we investigate the relaxation mechanisms that occur in quantum dots (QDs). First we consider energy relaxation in single particle self-assembled QDs by means of an Auger process. For the first time, relaxation rates are compared for dots of a realistic truncated pyramid shape and for the more elementary dot models considered previously. We find that the fast (pico-second) relaxation necessary for quantum dot based optoelectronics applications is made possible by dot electrons scattering with electrons located in the surrounding bulk material. We show that this relaxation mechanism is dominant by two orders of magnitude over the two-dimensional wetting layer scattering mechanism that has been considered in previous calculations.

Exact numerical diagonalisation is used to calculate the two-particle self-assembled QD wave functions. The small size of the QD means that the two electrons in the dot are found to be only weakly interacting. We find the relaxation rate for states of total spin 0 to be larger than the spin 1 rate by a factor of approximately 2. This is due to the double occupancy of the spin 0 spatial states.

We also consider the much slower spin flip relaxation in electrostatic QDs. We include the spin-orbit mixing that results from the bulk inversion asymmetry of the crystal lattice in calculating the exact two-particle states. We find that the spin orbit mixing causes anti-crossings to appear in the energy spectrum and deduce a new conservation rule related to this. We find an oscillation capable of slowing the relaxation time from microseconds to tenths of a second. This oscillation results from the vertical finite well confinement of the QD. It is found to depend on both magnetic field and the QD thickness and is of particular interest for quantum information applications where long-lived excited states are desirable.

Publication List

D. Chaney, M. Roy, P. A. Maksym and F. Long, "*The Effect of Self-Assembled Quantum Dot Geometry on Auger Relaxation Rate*", *Proceedings of the 26th International Conference on the Physics of Semiconductors* , **H257** (2002).

D. Chaney, M. Roy, P. A. Maksym, "*Efficient Calculation of Electron States in Self-assembled Quantum Dots: Application to Auger Relaxation*", to be published in *Proc. NATO ARW on Quantum Dots*, (2005).

Contents

List of Figures

List of Tables

Acknowledgements

I would like to express my thanks to all the members of the Condensed Matter Physics group at Leicester University for making my time there so enjoyable, and to my family for their continued support. Special thanks are due to Dr Peter Maksym for many fruitful discussions, and for his excellent supervision and guidance during the course of this work.

Chapter 1

Introduction

In recent years, there has been a lot of activity devoted to understanding the properties of the zero-dimensional systems known as quantum dots. This attention is motivated partly by a fundamental interest in the physics of low dimensional systems but also by the possibility of applications in areas such as optoelectronics and quantum computing [1]. In this thesis, we will investigate the relaxation mechanisms that occur in two distinct quantum dot systems. We will first consider fast energy relaxation in self-assembled quantum dots by means of an Auger process [2]. We compare the relaxation rates calculated for several different self-assembled quantum dot models and for the first time present results for dots of a realistic truncated pyramid shape. We find that the fast relaxation necessary for quantum dot based laser applications results from the dot electrons scattering with electrons located in the surrounding bulk material. We believe that this mechanism is discussed here for the first time and show that it is dominant over the two-dimensional wetting layer scattering that has been considered previously. Secondly, we will consider the much slower spin-flip relaxation processes in electrostatic quantum dots. We find a magnetic field dependent oscillation in the relaxation rate that results from the vertical confinement of the quantum dot. These oscillations are of particular interest for quantum information applications where long-lived excited states are desirable. We do not consider relaxation through photon emission since it is blocked by conservation of momentum.

Self-assembled quantum dots are small semiconductor islands formed during Stranski-Krastanow growth [3]. They are able to confine both electrons and holes, which mean they are of particular interest in optoelectronics applications, especially since it has been predicted that the temperature dependence of the laser threshold current will be virtually eliminated in zero-dimensional systems [4]. In order to achieve the population inversion needed for laser applications, carriers are usually either injected electrically or pumped optically into an excited energy state in the quantum dot. They must then relax down to the conduction band edge before the radiative recombination necessary for laser emission can take place. A fast relaxation process is therefore crucial if self-assembled quantum dots are to be a suitable candidate for efficient laser applications.

However, the allowed relaxation processes in self-assembled quantum dots have been the source of much controversy due to the so-called phonon bottleneck which was first proposed by U. Bockelmann and G. Bastard [5] and later by H. Benisty *et al.* [6]. These authors suggested that if there is a mismatch between the longitudinal optic phonon energy and the discrete energy spectrum of the quantum dot, phonon emission might be blocked. Therefore, phonon relaxation might not be able to provide the fast relaxation necessary for the proposed applications. However, experimental results [7, 8] have not indicated any such slowing of the relaxation rate even when the energy levels of the dot were separated by a few tens of meV.

It has been shown by D. Morris *et al.* [8] that an alternative mechanism capable of providing fast carrier relaxation at suitably high injected carrier densities is an Auger process. In this process, the dot electron is able to transfer some of its energy to an electron outside the dot via the Coulomb interaction. Auger relaxation rates have been calculated in the dipole approximation by A. V. Uskov *et al.* [9] for single particle systems where the dot electron scatters with an electron located in a two-dimensional wetting layer. However, we find that the dipole approximation is unlikely to be valid for quantum dots of any realistic size.

Many of the previous calculations relating to carrier relaxation in self-assembled dots [9, 10] have been restricted to simple models that do not reflect the geometry of the real system. This is due to complexity of the calculation and the difficulty of determining the exact size and shape of a self-assembled quantum dot. Recent scanning-tunnelling microscopy experiments have allowed the size, shape and composition to be more clearly determined [11, 12, ?, 14]. These experiments have indicated that self-assembled dots are likely to be of truncated pyramid shape and contain a composition gradient. In the past, the electronic states for pyramid shaped dots of uniform composition have been calculated using methods such as numerical solutions to the Schrödinger equation [15] and the diagonalisation of the Hamiltonian matrix with a basis set of plane waves [16]. In this work we will calculate the Auger relaxation rates with wave functions for a truncated pyramid shaped dot based on recent experiments by D. M. Bruls *et al.* [14]. These results will be compared with the relaxation rate calculated with a more elementary dot model of cylindrical symmetry and harmonic oscillator confinement. The truncated pyramid dot wave functions used in this work are calculated with a basis set of harmonic oscillator functions by M. Roy and P. A.

Maksym [17]. To the best of the authors knowledge, this is the first time these realistic quantum states have been used to calculate Auger relaxation rates in self-assembled quantum dots. We also find that the simple harmonic oscillator model that has been considered in previous calculations [9, 10] does not lead to accurate relaxation rates.

The Auger relaxation mechanism, since it relies on the Coulomb interaction between charged carriers, will be susceptible to influence by other carriers in the system. Screening by carriers in the surrounding bulk material for example, will affect the strength of the Coulomb interaction and therefore the relaxation rate. Another source of influence on the Auger relaxation rate would be the inclusion of a second electron confined within the dot, an effect that has not been considered previously. We calculate the two-particle wave functions exactly and find that the small size of the self-assembled dots considered here means that the Coulomb interaction between the dot electrons is relatively small compared to the energy of the individual particles. The electrons in the dot can therefore be considered only weakly interacting, having only a marginal effect on the relaxation rate.

The second type of quantum dot considered in this work is the electrostatic quantum dot. A thin InGaAs layer, which contains the dot, is sandwiched between two asymmetric AlGaAs barrier layers. Drain and source contacts of n-doped GaAs are provided above and below the barrier layers. A pillar is etched out of the heterostructure and a side gate is formed around the InGaAs layer in the pillar to provide the lateral confinement of the quantum dot. The side gate can also be used to change the number of electrons confined in the dot by varying the bias voltage. This type of dot has been reviewed by L. P. Kouwenhoven *et al.* [18]. Similar dots have been used in recent experiments to measure the single particle relaxation rates without a spin-flip and the two particle relaxation rates with a spin-flip by T. Fujisawa *et al.* [19, 20, 21]. Quantum dots have received a great deal of attention recently due to their potential applications in quantum computing [22, 23, 24]. Each quantum bit (qubit) is allowed to be in any state of a quantum two-level system. If practical quantum computing is to be realised, any useful qubit operations must be completed much faster than the decoherence time of the quantum state. As a prerequisite to a long decoherence time, those states must also be relatively long lived.

For transitions in a two-electron dot between states of total spin 1 and states of total spin 0, a spin-flip must occur before relaxation can take place. This could provide a long-lived excited state since spin-flip relaxation is usually slow. The slow spin-flip relaxation of an excited state will be an unlikely process in single electron dots since there would be nothing to stop the electron taking the faster route of relaxation without a spin-flip. When the work on spin-flip processes contained in this thesis was started, spin-flip relaxation in two-electron quantum dots had not been previously discussed theoretically.

In an ideal system, spin-flip relaxation is blocked by conservation of spin. However, real quantum dots are not ideal systems and a spin-orbit mixing term in the Hamiltonian makes spin-flip relaxation possible. A. V. Khaetskii and Y. V. Nazarov [25, 26, 27] considered several mechanisms that would allow a spin-flip in their treatment of single particle relaxation rates. Khaetskii *et al.* found that the dominant mechanism responsible for allowing spin-flip relaxation is spin-mixing. This causes the spin-up state to contain a small admixture of spin-down states and *vice versa.* The bulk inversion asymmetry of the crystal lattice gives rise to one such spin mixing mechanism which is sometimes known as the Dresselhaus mechanism. We include the Dresselhaus mechanism in our calculation of the exact two-particle quantum states. The Dresselhaus spin-orbit mixing mechanism is found to have an interesting effect on the two-particle energy spectrum. Where the singlet and triplet energy states previously crossed as the magnetic field is increased, the inclusion of the Dresselhaus term in the system Hamiltonian causes some of the crossings to become anti-crossings.

In the work on spin-flip relaxation presented in this thesis, we find an oscillation in the relaxation rate that is dependent on both magnetic field and the thickness of the electrostatic dot. The oscillation is found to be caused by the perpendicular finite well confinement of the heterostructure and can reduce the slow (microsecond) relaxation time by several orders of magnitude. This is of particular interest for applications where a long lived excited state is necessary.

1.1 Synopsis of the Thesis

In chapter 2 we present a review of the background information relevant to the material presented later in this thesis. We describe the quantum dot structures considered in this work and discuss the models that are used in later chapters. A review of the methods used to devise some of those models is also given. Finally, we discuss the method used to calculate the many body states employed later in this work.

In chapter 3, we investigate the relaxation of an excited electron in a single particle self-assembled quantum dot by means of an Auger process. The electron confined in the dot is able to relax by transferring some of its energy to an external electron via the Coulomb interaction. We consider two mechanisms where the external electron is located in either a two dimensional layer called the wetting layer located directly beneath the dot or in the surrounding three-dimensional bulk material. The relative density of the electrons located in the wetting layer and the three dimensional bulk material will play a crucial role in determining whether wetting layer or bulk scattering is the dominant relaxation mechanism. We use the experimental results of B. Liu *et al.* [28] to relate these densities, which allows the relaxation rates for both mechanisms to be compared. It is found that the bulk scattering mechanism is consistently dominant for the parameters used in this work. We also compare relaxation rates calculated in the dipole approximation and exactly for both mechanisms and find that the dipole approximation is unlikely to be valid for any realistic dot confinement. To illustrate the physics involved in the Auger relaxation process, we consider a relatively simple model of cylindrical shape and a soft-walled harmonic oscillator confinement potential. Our main results concern two truncated pyramid shaped dot models inspired by the experimental observations of Bruls *et al.* [14]. One of the truncated pyramid models is of pure InAs and the other is InGaAs and has a composition gradient that varies linearly from 60% Indium at the bottom to 100% Indium at the top. The effect of dot shape and composition on the relaxation rate is examined and parameter fitting methods for the more elementary harmonic oscillator model are considered.

In chapter 4 we consider Auger relaxation in a two-particle quantum dot and explore the new physics that arises from the Coulomb interaction between the confined electrons. The inclusion of a "spectator" electron is expected to modify the Auger mechanism and may therefore have an impact on the relaxation rates. This follows the discussion on single particle Auger relaxation given in chapter 3. We again consider the two relaxation mechanisms where the dot electron scatters with electrons located in either the wetting layer or the surrounding bulk material. We also use the same dot models as in chapter 3 allowing a direct comparison to be made. In addition to the screening of the Auger mechanism between the dot electrons and the external electrons, the screening of the Coulomb interaction between the two dot electrons when calculating the two-particle states is also considered. However, it is found that the two dot electrons are only weakly interacting in the self-assembled dots considered here. Since including the screening between the two dot electrons is extremely computationally expensive and only mildly affects the relaxation rate, this screening mechanism is neglected in the majority of our results.

We change direction slightly in chapter 5 and consider phonon-assisted spin-flip relaxation processes in two electron electrostatic quantum dots. We discuss several different mechanisms that are capable of providing the spin-orbit mixing necessary for spin-flip relaxation in quantum dots and draw on previous work in this field to identify the Dresselhaus mechanism as being dominant. A novel method for calculating the Dresselhaus spin-orbit interaction matrix elements is presented. We include the Coulomb interaction between the two dot electrons and calculate the energy spectrum as a function of magnetic field. The inclusion of the Dresselhaus spin-orbit mixing mechanism, is found to produce anti-crossings in the energy spectrum that are not present when spin-orbit mixing is neglected. We discuss the origin of these anti-crossings by considering a single particle system and find a new commutator relation and conservation rule, which is extended to include the two-particle system.

We then calculate the relaxation rate for two different phonon-coupling mechanisms. These are the deformation potential mechanism, which is a result of the band bending caused by the emitted phonon and the piezoelectric potential caused by the electric polarisation resulting from the strain produced by the emitted phonon. We also include the effects of screening on the piezoelectric relaxation rate later in chapter 5. We consider the non-interacting two particle system in order to explain the emergence of oscillations in the relaxation rate which are found to be dependent on both the magnetic field and the thickness of the quantum dot. These oscillations are caused by the vertical finite well confinement of the quantum dot and are capable of reducing the spin-flip relaxation rate by several orders of magnitude. We calculate the spin-flip relaxation rate for triplet-singlet transitions and Zeeman sub-level transitions. Of the two relaxation mechanisms considered here, we find that the deformation potential mechanism is dominant for all transitions except those with a sufficiently small energy gap. The spin-orbit mixing also produces some abrupt changes in the magnitude of the relaxation rates at the various magnetic fields that correspond to the anti-crossings in the energy spectrum. We explain this behaviour by introducing the concept of quasi-quantum numbers based on the expectation values for spin and angular momentum. We also compare the method and results presented here with previous theoretical and experimental work.

Finally, in chapter 6 we summarise and conclude the work of this thesis. Additionally, some suggestions for future work are made.

Chapter 2

Background

2.1 Quantum Dot Structures

In 1981, A. I. Ekimov and A. A. Onuschenko [29] published the first experimental observation of quantum confinement effects in CuCl crystals embedded in Silicate glass. Shortly after this ground breaking work, R. Rossetti and L. Bruls [30] presented the first studies of the luminescence properties of CdS colloids. This work provided the first experimental confirmation that the physical properties of zero-dimensional systems were strikingly different from their bulk counterparts. Since that time, zero-dimensional systems have become a significant and highly active area of research. Recent advances in experimental technique and improvements in the quality of samples available for study have provided many exciting opportunities for the study of these novel systems.

One of the first methods used to fabricate artificial quantum dots was a combination of electron beam lithography and reactive ion etching applied to a quantum well. M. A. Reed *et al.* [31] applied a polymer mask to a two-dimensional quantum well and used electron beam lithography to mark out the pattern of the dot. A gold mask was then applied to the pattern before a reactive ion etch was used to remove the unscreened material. This exposed a pillar that contained the quantum dot. Reed *et al.* reported fabrication of a cuboid shaped dot approximately 250nm square and $2-5$nm high, containing several hundred electrons. This was the first observation of the photoluminescence spectra for total quantisation by a fabrication-imposed potential. Similar experiments were carried out by J. Cibert *et al.* [32] who manufactured a cuboid shaped quantum dot and measured its luminescence properties. T. P. Smith III *et al.* [33] were successful in reducing the number of confined electrons to around 27. Smith *et al.* used capacitance spectroscopy to measure the energy levels of a quantum dot manufactured in a similar way to that of Reed *et al.*

A modulated electric field can also be used to localise electrons in a quantum well. T. J. Thornton *et al.* [34] used a split gate 15μm long and 0.6μm wide deposited onto a two-dimensional quantum well to confine electrons to a narrow channel. U. Meirav, *et al.* [35] also used the split gate method to form a narrow channel but were able to interrupt the channel by two barriers to confine electrons in all three spatial dimensions. Meriav *et al.* succeeded in measuring oscillations in the conductance corresponding to the addition of single electrons to the dot system.

A different method was used by Ch. Sikorski and U. Merkt [36] who produced an etched array of InSb islands by using a photoresist and a holographic periodic intensity pattern from an Ar laser. They capped the array with a NiCr film followed by a layer of SiO_2 and another NiCr film to act as a gate contact. An applied voltage between the gate and the InSb substrate produced a modulated electric field that could be used to confine fewer than 5 electrons in all three spatial dimensions. A similar technique was used by T. Demel *et al.* [37] to produce quantum dots containing 25 electrons from an AlGaAs/GaAs heterostructure. However, the goal of single electron confinement was finally achieved when B. Meurer, D. Heitmann, and K. Ploog [38] were able to produce a quantum dot containing one electron using a holographic fabrication technique similar to that of Sikorski and Merkt [36].

Rather than the arrays of electrostatic dots produced previously, R. C. Ashoori *et al.* [39] fabricated a single electrostatic dot from an AlGaAs/GaAs/AlGaAs heterostructure. The heterostructure was capped with 30nm of GaAs, on to this they applied a 1μm diameter CrAu disk and used a 30nm dry etch to leave a small GaAs island that had been masked by the disk. This island would then be used to provide the modulation of the electric field in a similar way to Refs. [36, 37, 38] mentioned in the previous paragraph. Onto the island was placed a 2μm diameter CrAu cap. The quantum dot was formed in the GaAs region of the heterostructure directly under the island by an electric field applied to the CrAu cap. The electric field could then be manipulated to confine anywhere between one and several thousand electrons. Ashoori *et al.* succeeded in fabricating this device onto a chip, which also contained a standard capacitor and a high electron-mobility transistor that was used to detect the capacitance signal from the dot.

In a vertical quantum dot device, the quantum dot itself is located in the centre of a pillar, sandwiched between two barrier layers. This type of dot provides a system where the number of confined electrons can be widely varied and their dynamics observed by manipulating the gate and contact voltages. The first transport measurements performed on this system were reported by S. Tarucha *et al.* [40] who measured the Coulomb oscillations produced by filling the electronic states. A comprehensive review of the properties of this type of dot is given by

L. P. Kouwenhoven *et al.* [18]. One of the pillar type quantum dots reviewed by Kouwenhoven is considered in chapter 5 (see figure 5.1). This type of pillar dot is actually a three-terminal field-effect transistor. Transient current spectroscopy experiments based on this type of vertical quantum dot device were performed by T. Fujisawa *et al.* [19, 20, 21] who were able to measure both direct energy relaxation rates and spin flip relaxation rates. Fujisawa's experiment provides the inspiration for the calculations presented in chapter 5.

The late 1980's and early 1990's, saw the appearance of self-assembled quantum dots (SAQD) as they have now became known. SAQDs are formed by molecular beam epitaxy in the Stranski-Krastanow growth mode [3] that occurs in systems with a high interface energy and a large lattice mismatch. The high interface energy promotes layer-by-layer growth so that the first few monolayers (typically 1.6-2.0) form an even two-dimensional film known as the wetting layer (WL). After this critical thickness has been deposited, the high strain energy is lowered by the onset of interfacial misfit dislocations that nucleate the formation of small islands. These islands are referred to as self-assembled quantum dots.

Initial studies of these structures were performed by several groups, for example D. J. Eaglesham and M. Cerullo [41] reported the growth of Ge islands on a Si (100) surface. Later, C. W. Snyder *et al.* [42], D. Leonard *et al.* [11] and J. Oshinowo *et al.* [43] all made similar structures by depositing $In_xGa_{1-x}As$ on a GaAs (100) substrate.

The exact size, shape and composition of self-assembled quantum dots has proven to be extremely difficult to determine. D. Leonard *et al.* [11] used transmission electron microscopy (TEM) and cross-sectional TEM (X-TEM) to examine uncapped $In_{0.5}Ga_{0.5}As$ dots grown on a GaAs substrate. These authors found the islands to be approximately 30nm in diameter but indicated that the actual size may be smaller since it was the strain field and not the dot itself that was being measured. S. Ruvimov *et al.* [12] and M. Grundmann *et al.* [44] used TEM and X-TEM to study InGaAs and InAs quantum dots which they reported to be of pyramid shape with a 12nm square base. N. Liu *et al.* [?] used cross-sectional scanning tunnelling microscopy (X-STM) to image stacked $\mathrm{In}_{0.5}\mathrm{Ga}_{0.5}\mathrm{As}$ SAQDs embedded in a GaAs matrix. They suggested that these dots have a truncated pyramidal shape with a trapezoidal base and an Indium rich central core of inverted pyramid or cone shape. More recently, D. M. Bruls *et al* [14] again used X-STM techniques to study InAs dots in a GaAs matrix. They reported a square based truncated pyramid shape with a graded Indium composition increasing linearly in the growth direction. The SAQD model proposed by D. M. Bruls *et al.* [14] provides the basis for some of the work presented in chapters 3 and 4.

2.2 Quantum Dot Models

We will now introduce the models used to represent the two different types of quantum dot discussed in this work. They are the self-assembled quantum dot and the electrostatic quantum dot.

The electrostatic quantum dot has been found to have cylindrical symmetry and has a lateral confinement potential that is very nearly parabolic [40]. One theoretical approach, originally devised to explore Landau diamagnetism [45] in free electrons was first formulated by V. Fock [46] and C. G. Darwin [47], and is widely used to describe this type of quantum dot. The parabolic confining potential accurately describes the electrostatic dot and takes into account the possibility of a perpendicular external magnetic field. The Fock-Darwin states for electron motion confined to a plane are given by the complete set:

$$R(r)\Phi(\phi) = \sqrt{\frac{n!}{\pi\lambda^2(|l|+n)!}} \left(\frac{r}{\lambda}\right)^{|l|} L_n^{|l|}\left(\frac{r^2}{\lambda^2}\right) \exp\left(-\frac{r^2}{2\lambda^2} - il\phi\right), \tag{2.1}$$

where $L_n^{|l|}(x)$ are the associated Laguerre polynomials and the wave functions are characterised by the quantum numbers $n = 0, 1, 2\ldots$ and $l = 0, \pm 1, \pm 2\ldots$ and the length parameter:

$$\lambda = \sqrt{\frac{\hbar}{m^*_{QD}\Omega}} \tag{2.2}$$

The length parameter is related to the characteristic oscillator frequencies

$$\Omega = \sqrt{\omega^2 + \left(\frac{\omega_c}{2}\right)^2}, \tag{2.3}$$

where $\hbar\omega$ is the confinement energy, $\omega_c = \frac{eB}{m^*_{QD}}$ is the cyclotron frequency, m^*_{QD} is the effective mass of the quantum dot carrier, e is the electronic charge and B is the external magnetic field applied in the z direction.

The electrostatic quantum dot considered in chapter 5 is fabricated from a quantum well. We therefore include a perpendicular confinement given by a finite well, but will reserve our discussion of the exact form of the z dependent factor of the wave functions until the relevant point of chapter 5.

For modelling the wave functions of a self-assembled quantum dot however, we will use an harmonic oscillator confinement potential in the z direction. In this case the wave functions have the form:

$$\sqrt{\frac{n!}{\pi^{\frac{3}{2}}\lambda_z\lambda^2 2^m m!(|l|+n)!}} \left(\frac{r}{\lambda}\right)^{|l|} L_n^{|l|}\left(\frac{r^2}{\lambda^2}\right) H_m\left(\frac{z}{\lambda_z}\right) \exp\left(-\frac{r^2}{2\lambda^2} - \frac{z^2}{2\lambda_z^2} - il\phi\right), \tag{2.4}$$

where $\lambda_z = \sqrt{\frac{\hbar}{m^*_{QD}\omega_z}}$, ω_z is the oscillator frequency in the z direction and H_m are the Hermite polynomials. We will refer to the states with this form of z dependent wave function as the harmonic oscillator (HO) states.

The energy spectrum relating to the HO states of expression 2.4 is given by:

$$E_{nlm} = (2n + |l| + 1)\,\hbar\Omega + \left(m + \frac{1}{2}\right)\hbar\omega_z - \frac{l}{2}\hbar\omega_c. \tag{2.5}$$

One method of fitting the parameters of the HO model to a real SAQD, is to choose Ω so that $\hbar\Omega = \Delta E$, where ΔE is the energy difference between any two SAQD levels. All other levels will be incorrectly predicted due to the equal spacing of the HO energy levels, a feature not found in real SAQDs. Once the energy gap has been matched, the vertical confinement energy ($\hbar\omega_z$) can be used to match the lower energy level of the transition being considered (see Eq. 2.5). Although we can match any two energy levels in this way, the length scales (Eq. 2.2) produced by this procedure do not always accurately reflect the size of a real SAQD. However, if it is the lowest lying energy levels that are matched, the length scales are usually quite close. Despite these apparent problems, the HO model has the significant benefit of its relative simplicity and can be used to qualitatively predict at least some of the physics of the SAQD.

Real self-assembled quantum dots however, do not generally have the cylindrical symmetry or the parabolic confinement potential of the HO model. In section 2.1, we saw that initial studies suggested that SAQDs were of a pyramid shape. The electronic structure of pyramidal InAs quantum dots has been calculated by several groups including that of M. Grundmann *et al.* [15] who used a numerical finite difference solution to the Schrödinger equation. M. A. Cussack *et al.* [16] modelled similar pyramidal dots by diagonalising the system Hamiltonian with a plane wave basis set. However, recent experiments [14] have shown that a SAQD is of truncated pyramid shape. In this work we will use the truncated pyramid SAQD single particle wave functions calculated by M. Roy and P. A. Maksym [17]. They found that the bound electronic states in a SAQD may be calculated more efficiently using a HO basis set than with the more commonly used plane wave basis set. Roy and Maksym [17] calculated the bound states of physically realistic SAQD models within the effective-mass approximation. Their calculation includes the position dependence of the effective-mass and most importantly the effect of the strain field within the system. The strain can drastically modify both the shape and the depth of the potential well. The single-particle states are calculated by expanding the exact wave function Ψ in terms of a HO (Eq. 2.4) basis set ψ_i and the complex amplitudes b_i:

$$\Psi = \sum_i b_i \psi_i, \tag{2.6}$$

where i labels the individual states in the HO basis set. The eigenvectors and eigenvalues are found by exact numerical diagonalisation of the Hamiltonian (see Roy *et al.* [17]), which is given by:

$$\hat{H} = \frac{1}{2}\left(-i\hbar\nabla + e\mathbf{A}\right) M^{-1} \left(-i\hbar\nabla + e\mathbf{A}\right) + V(\mathbf{r}), \tag{2.7}$$

where M is the effective mass tensor and $\mathbf{A}$ is the vector potential of the magnetic field ($B = \nabla \times \mathbf{A}$). The confinement potential, $V(\mathbf{r}) = V_0(\mathbf{r}) + V_c(\mathbf{r})$, is the sum of the band offset $V_0(\mathbf{r})$ and a second contribution $V_c(\mathbf{r})$ which results from the material strain.

An extra parameter z_{off} is used to offset the wave function from the origin of the coordinate system (defined as the centre of the dot) such that $z \rightarrow z - z_{off}$ in Eq. 2.4. The length scales λ and λ_z (see Eq. 2.2 etc.) are initially chosen to give the ground HO basis function a similar spatial extent to the actual localised state of the dot. The rate of convergence can then be improved by minimising the energy of the HO ground state confined in the dot potential with respect to z_{off} and the two length parameters.

Material	$In_xGa_{1-x}As$	InAs	InAs
Base (nm)	18 × 18	18 × 18	21 × 14
Top (nm)	10.6 × 10.6	10.6 × 10.6	11.5 × 7
Height (nm)	5	5	5
$\hbar\omega_0$ (meV)	170	170	190
$\hbar\omega_z$ (meV)	570	640	620
z_{off} (nm)	-0.25	-0.40	-0.56
E_0 (meV)	-225	-259	-246
E_1 (meV)	-155	-186	-185

Table 2.1: Parameters for the truncated pyramid self-assembled quantum dot models used in this work, from M. Roy *et al.* [48]. State energies are measured relative the conduction band edge of GaAs.

We will now introduce the specific self-assembled quantum dot models we will use in this work. In chapters 3 and 4 we consider two square based dots of truncated pyramid shape inspired by observations made by Bruls *et al.* [14]. The first is a graded material dot that has a composition of $In_xGa_{1-x}As$ where x varies linearly from 0.6 at the base to 1 at the top. The second is a truncated pyramid model of pure InAs. In chapter 3 we also consider a rectangular based dot of pure InAs. Details of the parameters used to calculate the self-assembled dot models are given in table 2.1 where $\hbar\omega_0$ and $\hbar\omega_z$ are the radial and vertical confinement energies respectively. These confinement energies relate to the length parameters λ and λ_z (see Eq. 2.2), z_{off} is the offset parameter described above. E_0 is the energy of the ground state and E_1 is the energy of the first excited state given relative to the GaAs conduction band edge.

2.3 Many Body Interactions

In many systems of interest, analytical solutions to the many particle Schrödinger equation are not possible unless approximations can be made. It may be possible to obtain reasonable results by neglecting the interaction of the electrons in the system or by treating it as a perturbation. However, approximations should be avoided in systems where the error introduced would be unacceptable or where the consequences of the interaction are not well understood.

In chapters 4 and 5, we consider quantum dots where we include a second "spectator" electron and wish to know what effect this has on the relaxation process. To do this we must take the interaction between the electrons into account when we calculate the two particle states of the system. The Hamiltonian of the many particle system is of the form:

$$\hat{H} = \sum_{i=1}^{N} \hat{h}(\mathbf{r}_i) + \frac{1}{2}\sum_{i=1}\sum_{\substack{j=1 \\ j\neq i}}^{N} v(\mathbf{r}_i, \mathbf{r}_j), \tag{2.8}$$

where the first term describes the individual electrons in the system and the second term describes the Coulomb interaction between them. In chapter 5, we also include the Dresselhaus spin-orbit mixing term (see section 5.2.1).

We expand the two particle wave functions in terms of non-interacting two particle states such that the eigenfunctions of the system are given by:

$$\Psi = \sum_{n} \frac{a_n}{\sqrt{2}} \left[\Phi_{n1}(\mathbf{r}_1)\,\Phi_{n2}(\mathbf{r}_2) \pm \Phi_{n1}(\mathbf{r}_2)\,\Phi_{n2}(\mathbf{r}_1)\right], \tag{2.9}$$

where $\Phi_i(\mathbf{r})$ are the single particle orthonormal basis states, usually the single particle states of the system being considered. This expansion leads to a matrix representation of the Hamiltonian. Calculation of the matrix elements for this Hamiltonian poses a significant challenge that requires the development of special numerical integration routines. Details of the individual matrix elements will be given in the relevant chapters. The complex amplitudes of the eigenvector components (a_n) are found by the exact diagonalisation of the system Hamiltonian. This is performed numerically by a "black box" routine supplied by the Numerical Algorithms Group [49]. We use a restricted basis set, the extent of which is determined by a convergence test, details of which will be given in subsequent chapters.

Chapter 3

Auger Relaxation in Self-Assembled Quantum Dots

In this chapter, we investigate relaxation of excited electrons in a self-assembled quantum dot (QD) by means of an Auger-like process. The Auger process in an atom starts when an inner shell electron is removed and the vacancy is then filled by a second electron relaxing from a higher shell. The energy released causes a third electron, the Auger electron, to be ejected from the atom. In the system considered here, we assume that an electron has been captured into an excited state in the dot and is able to relax by transferring its energy to an external electron via the Coulomb interaction. We consider mechanisms where the external electron is either located in the two-dimensional (2D) wetting layer (WL) or in the surrounding three-dimensional (3D) bulk material. The relative electron densities of the wetting layer and bulk, are expected to play a crucial role in determining which mechanism is dominant. We use experimental results [28] to relate these two densities, which will allow the rates of these two mechanisms to be compared.

The chapter is organised as follows. First in section 3.1 we provide a review of some of the previous work in this field before going on to calculate relaxation rates for both the wetting layer and bulk scattering mechanisms for a general QD in sections 3.2 and 3.3. Relaxation rates are calculated both exactly and in the dipole approximation for both mechanisms. In section 3.5, we illustrate the physics involved in the relaxation process by considering a dot model with a harmonic oscillator (HO) confinement (expression 2.4). We will compare the dipole and exact results for both relaxation mechanisms. It has been suggested that the dipole approximation may be valid for the self-assembled QD system [9], however we find this to be inaccurate. This inaccuracy is attributed to the increasing separation of the dot energy levels as the confinement is increased.

In section 3.5.4, we turn our attention to the various more realistic self-assembled quantum dot models introduced in chapter 2. These models are inspired by the experimental observations of D. M. Bruls *et al.* [14] and E. E. Vdovin *et al.* [50] and the quantum states are calculated by M. Roy *et al.* [17]. We compare the effect of dot shape and composition on relaxation rate and attempt to find parameter fitting methods that allow the more elementary HO model to be used to predict these rates. Finally in section 3.5.5, we provide a discussion of the results and the conclusions drawn.

3.1 Previous Work

It has long been known that one of the dominant carrier relaxation mechanisms in bulk semi-conductors is phonon emission. However, it was first proposed by U. Bockelmann and G. Bastard [5] and later by H. Benisty *et al.* [6] that the discrete energy levels in a QD might impose constraints on allowed relaxation mechanisms. The discrete QD energy levels and the weak energy dispersion of longitudinal optic phonons prompted suggestions that by energy conservation, unless the energy levels in the quantum dot were separated by the phonon energy ($\hbar\omega$), or multiples thereof, phonon relaxation will be strongly suppressed. This effect is known in the literature as the phonon bottleneck and has been somewhat controversial since experimental results [7] have not indicated any slowing of the relaxation rates.

A theoretical treatment of electron relaxation in quantum dots was presented by U. Bockelmann [51] who considered acoustic phonons coupling to electrons via the deformation potential. Bockelmann used a parabolic confinement in the radial plane with a finite well confinement in the axial direction consistent with electrostatic dots. Bockelmann calculated the relaxation rate as a function of radial confinement energy and found a peak rate of approximately $7.8 \times 10^9\text{s}^{-1}$ at a confinement energy of approximately 2.0meV.

The phonon relaxation rates are still low compared to experimentally measured rates, which are consistently of the order of $10^{10} - 10^{11}\text{s}^{-1}$ [8, 52]. This discrepancy has inspired much work dedicated to finding mechanisms that are capable of explaining this apparent shortfall. Multi-phonon mechanisms have been investigated by T. Inoshita and H. Sakaki [53] and later by X. Li *et al.* [54] who similarly considered coupling longitudinal optic phonons from the dot with bulk acoustic phonons. This treatment predicts a relaxation rate of approximately 10^{10}s^{-1} centred on the LO phonon energy. However, this still does not account for relaxation from the complete spectrum of energies found in quantum dots and is too slow to account for the picosecond relaxation times found in experiments [8].

Due to the difficulty of detecting phonon emission from quantum dots, few experiments to do this have ever been attempted. One such experiment to observe phonon emission from a quantum dot sample was performed by P. Hawker *et al.* [55]. These authors used a bolometric detector to observe strong acoustic phonon emission from stacked QD samples. However, the authors comment that it is not possible to definitively state the mechanism that gives rise to the observed phonon signal. Since phonon emission is known to be the dominant mechanism for electron relaxation in bulk semi-conductors, it is conceivable that the dot electrons might relax via some other mechanism and the resulting hot external electron quickly decays via phonon emission. The authors speculate that it may be an Auger process in the dot indirectly giving rise to the observed acoustic phonon signal.

If phonon relaxation is unable to account for relaxation over the full range of energies encountered in quantum dots, other mechanisms must be considered. It has been suggested that relaxation via an Auger mechanism might be a possible candidate for efficient carrier relaxation in QDs. Electrons in an excited state in the QD scatter with electrons located in the continuum states in either the bulk or the WL via a Coulomb interaction resulting in an energy transfer from the electron in the dot to an external electron. As the density of the bulk or WL electrons is increased it might be expected that the Auger mechanism will become dominant over other mechanisms.

U. Bockelmann and T. Egeler [56] discussed Auger relaxation in cuboid shaped quantum dots. Their dot model used infinite barriers in the lateral directions and a finite well in the axial direction. They considered scattering with a two dimensional electron-hole plasma and calculated picosecond relaxation rates for a plasma density of $2 \times 10^{11}\text{cm}^{-2}$.

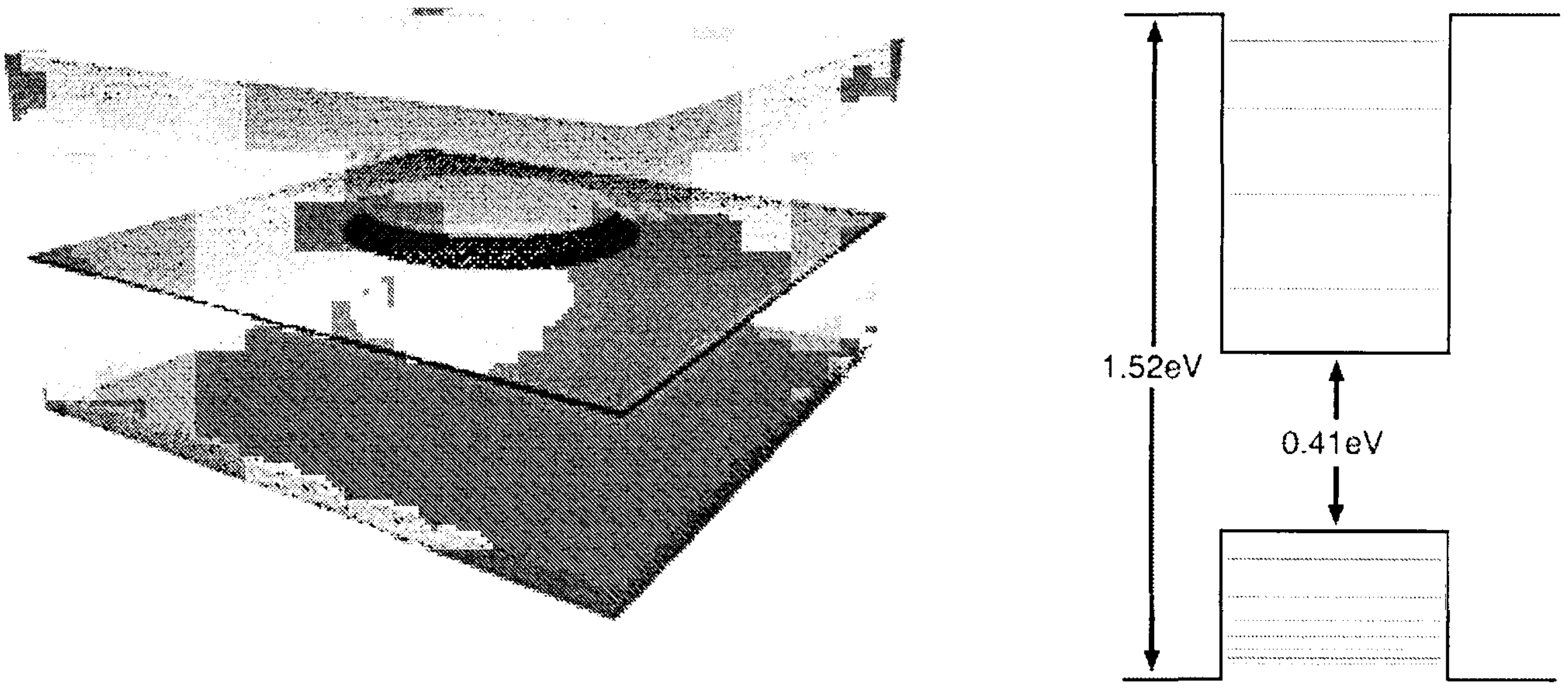

Figure 3.1: Left: schematic of a cylindrical model QD on top of the wetting layer. Both are embedded in bulk material. Right: corresponding energy diagram for an unstrained InAs dot embedded in a GaAs matrix.

Auger rate calculations have also been performed by A. V. Uskov *et al.* [9] for a cuboid dot with infinite barriers. Uskov *et al.* used the dipole approximation to derive analytical expressions in the unscreened, low temperature limit. They assumed that the Coulomb potential between dot and external carriers is slowly varying over the size of the QD and therefore the interaction potential can be expanded as $U(\mathbf{r}-\mathbf{r}_0) \approx U(\mathbf{r}) - \mathbf{r}_0 \cdot \nabla U(\mathbf{r})$. The calculation was also limited to scattering with carriers confined in the 2D WL on which the self-assembled quantum dot is placed (see figure 3.1). For a two-dimensional carrier density of $10^{11} - 10^{12}\text{cm}^{-2}$, Uskov *et al.* reported electron relaxation rates of $10^{11} - 10^{12}\text{s}^{-1}$.

Despite the recent work carried out on Auger relaxation processes, the author is unaware of any previous calculations regarding the validity of the dipole approximation. In addition, Auger relaxation calculations have been performed for scattering with electrons confined in the 2D WL [9, 56] but the author is unaware of any prior calculations for scattering with 3D bulk electrons. Similarly, the effect of QD geometry on Auger relaxation rate has also been unexplored. Existing Auger rate calculations are restricted to simplified QD models that, as discussed in chapter 2, do not have the precise geometry or energy characteristics of real self-assembled quantum dots. The validity of the dipole approximation, the 3D scattering mechanism and the effect of QD geometry are all discussed in this work.

3.2 Two Dimensional Auger Relaxation

In this section, we consider scattering of electrons confined in a QD by electrons located in the 2D WL. It is assumed that electrons have been inserted into the bulk material, where some will be captured into the wetting layer. A single electron is assumed to be confined in the first excited state in the quantum dot. We wish to keep the discussion completely general in this section and will provide a discussion of various QD models in section 3.5.

We assume that the Coulomb interaction will be screened predominantly by the electron density in the surrounding bulk. The presence of holes is neglected and this assumption is expected to have the effect of underestimating the magnitude of the screening. However, we do not expect this underestimation to affect the fundamental physics of the system. In the models used in this work, the QD is placed on top of the WL in the manner typical of self-assembled quantum dots, a schematic of this is shown in figure 3.1. We neglect any effect the presence of the WL may have on screening due to its small thickness and assume that the surrounding bulk material is of uniform composition throughout.

We anticipate that the 2D relaxation rate will be proportional to the density of electrons confined in the WL and that screening will increase with the bulk electron density. Therefore, the relative magnitudes of these densities will be important. Electron densities are calculated from the rate equations described by B. Liu *et al.* [28]. Liu *et al.* considered carriers injected into an excited state in the bulk conduction band (CB) at a rate $G(t)$, they then relax to the bulk CB edge in a time τ_{rel}. From there, they can either recombine with a hole in the bulk valence band (VB) in a time τ_{r1} or be captured into the WL in a time τ_{cap}. Carriers recombine in the WL in a time τ_{r2}. Densities in the bulk and the WL are calculated via a 3 level rate equation where n_p, n_{CB} and n_{WL} are defined to be the number of electrons at the pump energy, the bulk conduction band edge and in the wetting layer respectively. From Liu *et al.* [28] we have:

$$\begin{aligned}
\frac{dn_p(t)}{dt} &= G(t) - \frac{n_p(t)}{\tau_{rel}}, \\
\frac{dn_{CB}(t)}{dt} &= \frac{n_p(t)}{\tau_{rel}} - \frac{n_{CB}(t)}{\tau_{r1}} - \frac{n_{CB}(t)}{\tau_{cap}}, \\
\frac{dn_{WL}(t)}{dt} &= \frac{n_{CB}(t)}{\tau_{cap}} - \frac{n_{WL}(t)}{\tau_{r2}}.
\end{aligned} \tag{3.1}$$

where $t_{rel} = 2\text{ps}$, $t_{cap} = 7\text{ps}$, $t_{r1} = 1\text{ns}$, $t_{r2} = 0.25\text{ns}$ and $G(t)$ can be chosen to provide the required number of injected electrons (n_p).

We calculate the transition rates between states of equal energy by the application of Fermi's Golden Rule:

$$\frac{2\pi}{\hbar}\sum_{\mathbf{k}_i\mathbf{k}_f} | < \Psi_f(\mathbf{r},\mathbf{r}_0)|W(\mathbf{r},\mathbf{r}_0)|\Psi_i(\mathbf{r},\mathbf{r}_0) > |^2 f\left(k_i\right)\delta\left(E(\mathbf{k}_f) - E(\mathbf{k}_i) + \Delta E\right), \tag{3.2}$$

where $E(\mathbf{k}_i)$ and $E(\mathbf{k}_f)$ are the initial and final two-dimensional WL electron energies respectively. We must take into consideration the distribution of the energy of the states k_f and k_i. The distribution function will take the form $f(k_i)(1 - f(k_f)) + f(k_f)(1 - f(k_i))$ where $f(k)$ is a Boltzmann distribution. We assume that $f(k_i) \gg f(k_i)$ so that the distribution function reduces to $f(k_i)$. ΔE is the change in energy of the dot electron and $\mathbf{r}$ and $\mathbf{r}_0$ are the QD electron and WL electron coordinates respectively. Since the QD states are highly localised and the WL states are extended by comparison, is assumed that although the exchange term should be included in the formalism, it will be negligible and can safely be ignored. For this reason the wave functions, $\Psi(\mathbf{r}, \mathbf{r}_0)$ are taken to be the product of the QD and WL states.

Strictly, screening should be dealt with quantum mechanically but we will consider the coulomb interaction semi-classically and will therefore consider screening in the same way. To this end we choose the Yukawa potential [57] as the perturbation operator in the Golden rule:

$$W(\mathbf{r} - \mathbf{r}_0) = \frac{e^2}{4\pi\epsilon\epsilon_0} \frac{\exp(-\kappa|\mathbf{r} - \mathbf{r}_0|)}{|\mathbf{r} - \mathbf{r}_0|}, \tag{3.3}$$

where $\kappa = \sqrt{4\pi e^2 n_3/(\epsilon\epsilon_0 k_B T)}$ is the 3D Debye screening wave number resulting from the use of a Boltzmann distribution, n_3 is the bulk electron density and T is the temperature of the bulk electrons.

3.2.1 The Exact Relaxation Rate

In this section, we calculate the exact Auger relaxation rate for scattering of dot electrons by electrons confined in the 2D wetting layer. Because of the need to use a mixture of 2D and 3D vectors, we will take the convention that vectors denoted by upper case letters are three-dimensional whereas vectors denoted by lower case letters are two-dimensional. We define a coordinate system such that the origin is placed in the centre of the dot. We ignore the finite thickness of the wetting layer which is parallel to the $x - y$ plane, a distance z_0 below the origin.

We begin by writing the Yukawa potential (Eq. 3.3) that appears in the matrix element of Fermi's Golden Rule (expression 3.2) as a Fourier transform:

$$W\left(\mathbf{R}-\mathbf{R}_0\right)=\frac{e^2}{8\pi^3\epsilon\epsilon_0}\int\frac{e^{i\mathbf{Q}\cdot(\mathbf{R}-\mathbf{R}_0)}}{\kappa^2+Q^2}d\mathbf{Q}, \tag{3.4}$$

where $\mathbf{R}_0=(\mathbf{r}_0,z_0)$. We assume that the 2D WL wave functions are plane waves that have the form $A^{-\frac{1}{2}}\exp(i\mathbf{k}\cdot\mathbf{r}_0)$, where A is the area of the wetting layer, so that the matrix element appearing in the Golden Rule (Eq. 3.2) is then:

$$\frac{e^2}{8\pi^3\epsilon\epsilon_0 A}\int e^{i\left(\mathbf{k}_f-\mathbf{k}_i\right)\cdot\mathbf{R}_0}\phi_f^*\left(\mathbf{R}\right)\left\{\int\frac{e^{i\mathbf{Q}\cdot(\mathbf{R}-\mathbf{R}_0)}}{\kappa^2+Q^2}d\mathbf{Q}\right\}\phi_i\left(\mathbf{R}\right)d\mathbf{R}_0 d\mathbf{R}. \tag{3.5}$$

The $\mathbf{R}_0$ integral is:

$$\int\exp\left[i\left(\mathbf{k}_f-\mathbf{k}_i\right)\cdot\mathbf{r}_0-i\mathbf{Q}\cdot\mathbf{R}_0\right]d\mathbf{R}_0=$$
$$4\pi^2\exp\left[-iQ_\perp z_0\right]\delta\left[\mathbf{k}_f-\mathbf{k}_i-\mathbf{Q}_\parallel\right]. \tag{3.6}$$

Substituting the result of Eq. 3.6 into expression 3.5, we perform the integral over $\mathbf{Q}_\parallel$ to remove the delta function which gives the matrix element as:

$$\frac{e^2}{2\pi\epsilon\epsilon_0 A}\int\frac{\exp\left(-iQ_\perp z_0\right)}{\left[\kappa^2+\left(\mathbf{k}_f-\mathbf{k}_i\right)^2+Q_\perp^2\right]}\left\langle\phi_f^*\left(\mathbf{R}\right)\left|e^{\left[-i\left(\mathbf{k}_f-\mathbf{k}_i+\mathbf{Q}_\perp\right)\cdot\mathbf{R}\right]}\right|\phi_i\left(\mathbf{R}\right)\right\rangle dQ_\perp. \tag{3.7}$$

We substitute this result into the Golden rule (expression 3.2) where $f(k_i)$ is the 2D Boltzmann distribution. We convert the sum over $\mathbf{k}_i$ and $\mathbf{k}_f$ given in the Golden rule to an integral in the usual way to give the relaxation rate as:

$$\frac{e^4 n_2 m_{QD}^*}{8\pi^4\epsilon^2\epsilon_0^2 k_B T\hbar m_{WL}^*}\int\times$$
$$\left|\int\left\langle\phi_f\left(\mathbf{R}\right)\left|e^{i\left[\left(\mathbf{k}_f-\mathbf{k}_i\right)+\mathbf{Q}_\perp\right]\cdot\mathbf{R}}\right|\phi_i\left(\mathbf{R}\right)\right\rangle\frac{\exp\left[iQ_\perp z_0\right]}{\left[\kappa^2+\left(\mathbf{k}_f-\mathbf{k}_i\right)^2+Q_\perp^2\right]}dQ_\perp\right|^2\times$$
$$\exp\left(-\alpha k_i^2\right)\delta\left(k_f^2-k_i^2-\beta^2\right)d\mathbf{k}_i d\mathbf{k}_f, \tag{3.8}$$

where

$$\alpha=\frac{\hbar^2}{2m_{WL}^* k_B T},$$
$$\beta=\sqrt{\frac{2m_{QD}^*}{\hbar^2}\left(E_i-E_f\right)}, \tag{3.9}$$

m^*_{QD} is the effective mass of the QD electron, m^*_{WL} is the effective mass of the WL electron, E_i is the initial energy of the dot, E_f is the final energy of the dot which for energy relaxation has the relationship $E_i > E_f$.

In expression 3.8 the substitution $\mathbf{k}_f = \mathbf{q} + \mathbf{k}_i$ is now made, which allows the delta function to be rewritten as $\delta(k_f^2 - k_i^2 - \beta^2) = \delta(q^2 - \beta^2 + 2|q||k_i|\cos\theta_i)$ with the rest of the expression independent of θ_i. We now split the θ_i integral into two parts where the limits range from 0 to π and from π to 2π and make the change of variable $\cos\theta = \pm x$ to give the integral over θ as:

$$\frac{1}{|\mathbf{q}||\mathbf{k}_i|}\int_{-1}^{1}\delta\left[\frac{q^2-\beta^2}{2|\mathbf{q}||\mathbf{k}_i|}-x\right]\frac{dx}{\sqrt{1-x^2}} = \frac{2\Theta\left(\frac{q^2-\beta^2}{2|\mathbf{q}||\mathbf{k}_i|}-1\right)}{\left[4q^2k_i^2-(q^2-\beta^2)^2\right]^{\frac{1}{2}}}, \tag{3.10}$$

where Θ is the Heaviside step function which will modify the lower limit on the k_i integral. The result of substituting Eq. 3.10 into expression 3.8 then gives the k_i integral as:

$$\int_{\eta(\mathbf{q})}^{\infty}\frac{k_i\exp\left(-\alpha k_i^2\right)}{\left[4q^2k_i^2-(q^2-\beta^2)^2\right]^{\frac{1}{2}}}dk_i = \sqrt{\frac{\pi}{\alpha}}\frac{1}{4q}\exp\left\{-\alpha\left[\eta\left(\mathbf{q}\right)\right]^2\right\}, \tag{3.11}$$

where we have made use of the change of variable $u^2 = k^2[\eta(\mathbf{q})]^{-2} - 1$ and we have defined:

$$\eta\left(\mathbf{q}\right) = \frac{|q^2-\beta^2|}{2\left|\mathbf{q}\right|}. \tag{3.12}$$

Using the results of Eqs. 3.10 and 3.11 we return to expression 3.8 and find the exact relaxation rate for scattering dot electrons with electrons located in the wetting later is:

$$\frac{e^4 n_2 m^*_{QD}}{16\pi^4\epsilon^2\epsilon_0^2\hbar^2 m^*_{WL}}\sqrt{\frac{2\pi m^*_{WL}}{k_B T}}\int\frac{1}{|\mathbf{q}|}\exp\left\{-\alpha\left[\eta\left(\mathbf{q}\right)\right]^2\right\}\times$$
$$\left|\int\left\langle\phi_f(\mathbf{r})\left|e^{(i\mathbf{q}+\mathbf{Q}_\perp)\cdot\mathbf{r}}\right|\phi_i(\mathbf{r})\right\rangle\frac{\exp\left(-iQ_\perp z_0\right)}{\kappa^2+q^2+Q_\perp^2}dQ_\perp\right|^2 d\mathbf{q}. \tag{3.13}$$

At this point the result is general for any quantum dot state. Later in this chapter, we will discuss the effect of using various different quantum dot models and shall use this expression as the starting point for our discussion.

3.2.2 The Dipole Relaxation Rate

Starting with Eq. 3.4, we make the dipole approximation by making the assumption that $|\mathbf{r}_0| \gg |\mathbf{R}|$ and expand the $\mathbf{R}$ part of the exponential to give:

$$\frac{e^2}{8\pi^3\epsilon\epsilon_0}\int\frac{\exp\left(-i\mathbf{Q}\cdot\mathbf{r}_0\right)}{\kappa^2+Q^2}\left[\sum_{n=0}^{3}\frac{i^n}{n!}\left(\mathbf{Q}\cdot\mathbf{R}\right)^n\right]d\mathbf{Q}. \tag{3.14}$$

Strictly, the dipole approximation requires expansion to only linear ($n = 1$) order but to aid our comparison to the exact result of section 3.2.1, we include terms up to and including cubic order.

Using this form of the Yukawa potential, the matrix element in Eq. 3.2 becomes:

$$\frac{e^2}{8\pi\epsilon\epsilon_0 A}\int\exp\left[i\left(\mathbf{k}_f-\mathbf{k}_i\right)\cdot\mathbf{r}_0\right]\phi_f^*\left(\mathbf{R}\right)\frac{\exp\left(-i\mathbf{Q}\cdot\mathbf{r}_0\right)}{\kappa^2+Q^2}\times$$
$$\left[\sum_{n=0}^{3}\frac{i^n}{n!}\left(\mathbf{Q}\cdot\mathbf{R}\right)^n\right]\phi_i\left(\mathbf{R}\right)d\mathbf{Q}d\mathbf{r}_0d\mathbf{R}. \tag{3.15}$$

We notice that the $\mathbf{r}_0$ integral is identical to that of Eq. 3.6 where the result is given by $4\pi^2\exp[-iQ_\perp z_0]\delta[\mathbf{k}_f-\mathbf{k}_i-\mathbf{Q}_{||}]$. We remove this delta function by integrating over $\mathbf{Q}_{||}$ as described in section 3.2.1 and substitute a 2D Boltzmann distribution for $f(k_i)$ which gives the dipole equivalent of expression 3.8 as:

$$\frac{e^4 n_2 m_{QD}^*}{8\pi^4\epsilon^2\epsilon_0^2 k_B T\hbar m_{WL}^*}\int\exp\left(-\alpha k_i^2\right)\delta\left(k_f^2-k_i^2-\beta^2\right)\times$$
$$\left|\int\left\langle\phi_f\left|\left\{\sum_{n=0}^{3}\frac{i^n}{n!}\left[\left(\mathbf{k}_f-\mathbf{k}_i+Q_\perp\right)\cdot\mathbf{R}\right]^n\right\}\right|\phi_i\right\rangle\frac{\exp\left(-iQ_\perp z_0\right)}{\kappa^2+q^2+Q_\perp^2}dQ_\perp\right|^2 d\mathbf{k}_f d\mathbf{k}_i. \tag{3.16}$$

We now recognise that the first term of the dipole expansion in expression 3.16 is unity which when integrated between orthogonal QD states will simply vanish.

Terms of even order also vanish since the integrand will be an odd function. Hence only terms of odd order contribute to the relaxation rate in this extended dipole approximation. We use Eqs. 3.10, 3.11 and 3.12 to remove the delta function in expression 3.16. The integral over k_i is performed in the same way we described in section 3.2.1 and we find the 2D dipole relaxation rate to be:

$$\frac{e^4 n_2 m^*_{QD}}{16\pi^4\epsilon^2\epsilon_0^2\hbar^2 m^*_{WL}}\sqrt{\frac{2\pi m^*_{WL}}{k_B T}}\int \frac{1}{\left|\mathbf{Q}_{\|}\right|}\exp\left\{-\alpha\left[\eta\left(\mathbf{Q}_{\|}\right)\right]^2\right\}\times$$
$$\left|\int\left\langle\phi_f(\mathbf{R})\left|i\mathbf{Q}\cdot\mathbf{R}-\frac{i}{3!}\left[\mathbf{Q}\cdot\mathbf{R}\right]^3\right|\phi_i(\mathbf{R})\right\rangle\frac{\exp\left(-iQ_\perp z_0\right)}{\kappa^2+Q^2}dQ_\perp\right|^2 d\mathbf{Q}_{\|}. \quad (3.17)$$

This expression, like Eq. 3.13 is completely general for any quantum dot state and we shall return to this point when we compare the two results in section 3.5.1.

3.3 Three Dimensional Auger Rate

In this section we consider an electron in the QD scattering with electrons located in the surrounding bulk. We consider both the exact calculation and the dipole approximation. The presence of the WL is neglected and we assume that screening will be provided by the electron density in the surrounding material as we did in section 3.2. In similar fashion to the 2D case, we assume that the bulk electron will be well described by plane waves of the form $V^{-1}\exp(i\mathbf{k}\cdot\mathbf{r}_0)$. In this section we define a lower case bold font to denote three-dimensional vectors throughout. In order to compare our results to the 2D relaxation rates, we will use the same injected carrier rate $G(t)$ as in section 3.2.

3.3.1 The Exact Relaxation Rate

Using the Yukawa potential of Eq. 3.3 in the matrix element that appears in the Golden Rule (expression 3.2) we have:

$$\frac{e^2}{4\pi\epsilon\epsilon_0 V}\int \exp\left[i\left(\mathbf{k}_f-\mathbf{k}_i\right)\cdot\mathbf{r}_0\right]\phi_f^*\left(\mathbf{r}\right)\phi_i\left(\mathbf{r}\right)\frac{\exp\left(-\kappa\left|\mathbf{r}-\mathbf{r}_0\right|\right)}{\left|\mathbf{r}-\mathbf{r}_0\right|}d\mathbf{r}d\mathbf{r}_0. \tag{3.18}$$

Making the substitution, $\exp[i(\mathbf{k}_f-\mathbf{k}_i)\cdot\mathbf{r}_0] = \exp[i(\mathbf{k}_f-\mathbf{k}_i)\cdot\mathbf{r}]\exp[-i(\mathbf{k}_f-\mathbf{k}_i)\cdot(\mathbf{r}-\mathbf{r}_0)]$ in the above expression, the $\mathbf{r}_0$ integral then becomes the Fourier transform of the Yukawa potential:

$$\int\frac{\exp\left(-\kappa\left|\mathbf{r}-\mathbf{r}_0\right|\right)}{\left|\mathbf{r}-\mathbf{r}_0\right|}\exp\left[-i\left(\mathbf{k}_f-\mathbf{k}_i\right)\cdot\left(\mathbf{r}-\mathbf{r}_0\right)\right]d\mathbf{r}_0 = \frac{4\pi}{\kappa^2+\left(\mathbf{k}_f-\mathbf{k}_i\right)^2}. \tag{3.19}$$

Substituting this result into the matrix element we have:

$$\frac{e^2}{\epsilon\epsilon_0 V}\left[\kappa^2+\left(\mathbf{k}_f-\mathbf{k}_i\right)^2\right]^{-1}\left\langle\phi_f\left(\mathbf{r}\right)\left|\exp\left[i\left(\mathbf{k}_f-\mathbf{k}_i\right)\cdot\mathbf{r}\right]\right|\phi_i\left(\mathbf{r}\right)\right\rangle. \tag{3.20}$$

Substituting this matrix element in the Golden rule, where $f(k_i)$ is a three dimensional Boltzmann distribution, gives:

$$\frac{4e^4 n_3 m^*_{QD}}{\pi^2\epsilon^2\epsilon_0^2}\left[\frac{\pi}{2m^*_B k_B T}\right]^{\frac{3}{2}}\int\frac{\exp\left(-\alpha k_i^2\right)}{\kappa^2+\left(\mathbf{k}_f-\mathbf{k}_i\right)^2}\times$$
$$\left|\left\langle\phi_f\left(\mathbf{r}\right)\left|\exp\left[i\left(\mathbf{k}_f-\mathbf{k}_i\right)\cdot\mathbf{r}\right]\right|\phi_i\left(\mathbf{r}\right)\right\rangle\right|^2\delta\left(k_f^2-k_i^2-\beta^2\right)d\mathbf{k}_f d\mathbf{k}_i. \tag{3.21}$$

Proceeding in similar fashion to that of section 3.2.1 we make the change of variable $\mathbf{k}_f = \mathbf{q}+\mathbf{k}_i$. The delta function then becomes $\delta(k_f^2-k_i^2-\beta^2) = \delta(q^2-\beta^2+2|\mathbf{q}||\mathbf{k}_i|\cos\theta_i)$ where the rest of the integrand is independent of θ_i. Making the change of variable $\cos\theta_i = x$ so that $-\sin\theta_i d\theta_i = dx$, our choice of spherical polar coordinates allows us to simplify the θ_i integral to:

$$\frac{1}{2|\mathbf{q}||\mathbf{k}_i|}\int_{-1}^{1}\delta\left[\frac{q^2-\beta^2}{2|\mathbf{q}||\mathbf{k}_i|}+x\right]dx = \frac{1}{2|\mathbf{q}||\mathbf{k}_i|}\Theta\left(\frac{q^2-\beta^2}{2|\mathbf{q}||\mathbf{k}_i|}-1\right), \tag{3.22}$$

where Θ is the Heaviside step function, which affects the lower limit on the k_i integral in the same way as Eq. 3.11. The k_i integral then has the form:

$$\int_{\eta(\mathbf{q})}^{\infty} k \exp\left[-\alpha k_i^2\right] dk = [2\alpha]^{-1} \exp\left\{-\alpha\left[\eta(\mathbf{q})\right]^2\right\}. \tag{3.23}$$

Substituting the results of Eq. 3.23 into expression 3.21 we have the relaxation rate as:

$$\frac{2e^4 n_3 m_{QD}^*}{\hbar^2 \epsilon^2 \epsilon_0^2}\left[\frac{\pi}{2m_B^* k_B T}\right]^{\frac{1}{2}} \int \frac{\exp\left\{-\alpha\left[\eta(\mathbf{q})\right]^2\right\}}{\left[\kappa^2+q^2\right]^2 |\mathbf{q}|}\left|\left\langle \phi_f(\mathbf{r})\left|e^{i\mathbf{q}\cdot\mathbf{r}}\right|\phi_i(\mathbf{r})\right\rangle\right|^2 d\mathbf{q}. \tag{3.24}$$

Again, this expression is applicable to general QD states and will be used in the discussion of the various QD models considered subsequently.

3.3.2 The Dipole Relaxation Rate

We start with the dipole approximation to the Yukawa potential (expression 3.14) and take the matrix element of initial and final states to give:

$$\begin{aligned}\frac{e^2}{8\pi\epsilon\epsilon_0 V} \quad & \int \exp\left[i\left(\mathbf{k}_f-\mathbf{k}_i\right)\cdot\mathbf{r}_0\right]\phi_f^*(\mathbf{r})\,\frac{\exp\left(-i\mathbf{q}'\cdot\mathbf{r}_0\right)}{\kappa^2+q'^2} \times \\ & \left\{\sum_{n=0}^{3}\frac{i^n}{n!}\left[\mathbf{q}'\cdot\mathbf{r}\right]^n\right\}\phi_i(\mathbf{r})\,d\mathbf{q}'d\mathbf{r}_0 d\mathbf{r}.\end{aligned} \tag{3.25}$$

Since $\mathbf{k}_f$, $\mathbf{k}_i$ and $\mathbf{q}'$ are all three dimensional, the integral over external electron coordinates is $\int \exp[i(\mathbf{k}_f-\mathbf{k}_i-\mathbf{q}')\cdot\mathbf{r}_0]d\mathbf{r}_0 = 8\pi^3\delta(\mathbf{k}_f-\mathbf{k}_i-\mathbf{q}')$. This allows the $\mathbf{q}'$ integral to be performed easily to give:

$$\frac{e^2}{\epsilon\epsilon_0 V\left[\kappa^2+\left(\mathbf{k}_f-\mathbf{k}_i\right)^2\right]}\left\langle \phi_f^*(\mathbf{r})\left|\left\{\sum_{n=0}^{3}\frac{i^n}{n!}\left[\left(\mathbf{k}_f-\mathbf{k}_i\right)\cdot\mathbf{r}\right]^n\right\}\right|\phi_i(\mathbf{r})\right\rangle. \tag{3.26}$$

We substitute expression 3.26 into the Golden Rule, where $f(k_i)$ is a three dimensional Boltzmann distribution. This gives the relaxation rate as:

$$\begin{aligned}&\frac{4e^4 n_3 m_{QD}^*}{\pi\epsilon^2\epsilon_0^2}\left[\frac{\pi}{2m_B^* k_B T}\right]^{\frac{3}{2}} \int \frac{\exp\left(-\alpha k_i^2\right)}{\left[\kappa^2+\left(\mathbf{k}_f-\mathbf{k}_i\right)^2\right]^2}\delta\left(k_f^2-k_i^2-\beta^2\right) \times \\ &\left|\left\langle \phi_f^*(\mathbf{r})\left|\left\{\sum_{n=0}^{3}\frac{i^n}{n!}\left[\left(\mathbf{k}_f-\mathbf{k}_i\right)\cdot\mathbf{r}\right]^n\right\}\right|\phi_i(\mathbf{r})\right\rangle\right|^2 d\mathbf{k}_i d\mathbf{k}_f.\end{aligned} \tag{3.27}$$

We again change variable to $\mathbf{k}_f = \mathbf{q} + \mathbf{k}_i$ and perform the manipulations on the delta function as described in section 3.3.1. The lower limit on the k_i integral is similarly affected as in Eq. 3.11. Our choice of spherical polar coordinates means that the ϕ_{k_i} integral results in a factor of 2π. This leaves the k_i radial part of the integral which has the same form as Eq. 3.23. Even terms in the dipole expansion vanish which leaves the relaxation rate as:

$$\frac{2e^4 n_3 m_{QD}^*}{\hbar^2 \epsilon^2 \epsilon_0^2}\left[\frac{\pi}{2m_B^* k_B T}\right]^{\frac{1}{2}} \int \frac{\exp\left\{-\alpha\left[\eta\left(\mathbf{q}\right)\right]^2\right\}}{\left[\kappa^2+q^2\right]^2 |\mathbf{q}|} \times$$
$$\left|\left\langle \phi_f\left(\mathbf{r}\right)\middle| i\mathbf{q}\cdot\mathbf{r} - \frac{i}{3!}\left(\mathbf{q}\cdot\mathbf{r}\right)^3 \middle| \phi_i\left(\mathbf{r}\right)\right\rangle\right|^2 d\mathbf{q}. \tag{3.28}$$

3.4 Computational Considerations

The calculations described in this chapter require multi-dimensional integrals to be performed numerically and in this section we review some of the computational methods used to perform this task. The primary method of integration used in this work is Simpson's rule. This is used for all numerical integrations except in some circumstances where a discrete Fourier transform is employed. All numerical methods will be briefly reviewed and the accuracy of the integrals computed in this work will be discussed.

Simpson's rule is one of the most widely used techniques for numerical integration and is exact for polynomials of up to second order. The method presented here is given in the form found in *Numerical Recipes in C* [58]:

$$\int_{x_0}^{x_2} f(x)\,dx \approx h\left[\frac{1}{3}f(x_0) + \frac{4}{3}f(x_1) + \frac{1}{3}f(x_2)\right] + O(h^5 f^{(4)}), \tag{3.29}$$

where x_1 is a point equidistant from x_0 and x_2, and $f^{(4)}$ denotes the fourth derivative of the function f, evaluated at an unknown place in the interval h. The unknown nature of the error associated with this method of integration means that the integrals cannot be calculated to arbitrary accuracy. However, systematically increasing the number of sampling points and comparing the results for convergence is a method often used to gain an indication of the accuracy of the numerical integral. This is a method we employ repeatedly during the course this work.

If the integral can be split into equally spaced sections, Simpson's rule can be repeated as many times as is necessary. The integral is then approximated by:

$$\int_a^b f(x)\,dx \approx \frac{h}{3}\left[f(x_0) + 4f(x_1) + 2f(x_2) + 4f(x_3) + \ldots \right.$$
$$\left. \ldots + 2f(x_{n-2}) + 4f(x_{n-1}) + f(x_n)\right] \tag{3.30}$$

where there are $n+1$ points equally spaced by the distance h. This form of Simpson's rule is employed repeatedly in this work.

The second computational method used here is the discrete Fourier transform (DFT) which is used to approximate the Fourier integral:

$$H(k) = \int_a^b \exp(ikx)\, h(x)\, dx \approx \Delta \sum_{j=0}^{M-1} h_j \exp(ikx_j) \tag{3.31}$$

where the sampling interval $\Delta = (b-a)M^{-1}$, M is the number of subintervals, $x_j = a + j\Delta$ and $j = 0, 1, \ldots, M$. However, this approximation to the Fourier integral does not match the definition of the standard numerical discrete Fourier transform routine (as supplied by NAG Ltd. [49]) we wish to use. The problem arises because the DFT introduces a phase factor when the lower limit on the integral is non-zero. We must therefore correct this phase factor to eliminate the problem.

If we define $k_m = 2\pi m(b-a)^{-1}$ where $m = 0, 1 \ldots$, such that $k_m\Delta = 2\pi m M^{-1}$ we can allow for the phase correction by substituting for x_j in the exponential on the right hand side of Eq. 3.31 and the approximation to the Fourier integral then becomes:

$$\begin{aligned} \int_a^b \exp(ikx)\, h(x)\, dx \quad &\approx \Delta \exp(ik_m a) \sum_{j=0}^{M-1} h_j \exp\left(\frac{i2\pi mj}{M}\right) \\ &= \Delta \exp(ik_m a) \left[\mathrm{DFT}(h_0, \ldots h_{M-1})\right]. \end{aligned} \tag{3.32}$$

This approximation to the Fourier integral can suffer from a problem called aliasing. If the function $H(k) \neq 0$ for $k \geq k_c$ where $k_c = (2\Delta)^{-1}$ (known as the Nyquist critical frequency) then all of the data that lies outside of the range $-k_c < k < k_c$ is spuriously translated or aliased onto that range. Technically, we should include corrections to this aliasing since it is possible for the accuracy of the integral to be compromised.

Numerical methods always have an error term associated with the approximation and is usually a function of some small parameter. This small parameter for DFT's is not $\Delta(b-a)^{-1} = M^{-1}$ as it would be if the integrand was not oscillating but is actually $k\Delta$ which leads to a systematic decrease in the accuracy of the integral as the sampling frequency k_m is increased. Clearly there is a need to reduce the aliasing errors, which we can do by increasing the sampling rate, without introducing unacceptable systematic errors.

We must include the phase corrections, but to also include anti-aliasing terms when evaluating a three-dimensional Fourier transform would lead to some lengthy and somewhat intractable calculations. Fortunately, the wave functions used in this work are all slowly varying and decay well before the sampling range is truncated. Therefore the usual aliasing errors associated with DFTs do not cause any difficulty and the low sampling rates needed for convergence (typically 100 points), do not give rise to any significant systematic errors. Anti-aliasing corrections can therefore be neglected without any significant loss of accuracy provided the appropriate sampling range is carefully identified.

The real space range over which the DFT is to be performed is $x_r = b - a$. From the definition of k_m we have the frequency range of $k_r = 2\pi M(b-a)^{-1}$ which leads to the relation $k_r = 2\pi M(x_r)^{-1}$. This relation can be used to locate the optimum range for the transform. Obviously, we wish to avoid truncation which can lead to aliasing errors both before and after the transform and we wish to simultaneously minimise the systematic errors due to the choice of sampling rate.

In general, we wish to transform quantum dot wave functions of the form described by the HO wave functions in expression 2.4 or in the case of the self-assembled models, a sum thereof. In any case the function we wish to transform will always be the product of a polynomial and a Gaussian with a characteristic length parameter λ. By inspecting the quantum numbers needed to generate any given wave function we can deduce the order of the polynomial and use the relation above to optimise the sample range accordingly. We do this by examining the decay of the function and its Fourier transform and find that the *ad hoc* relation $2\pi\lambda\Delta^{-1} \approx 10$ provides a range sufficient that truncation errors are avoided and systematic errors are minimised.

Fourier transforms when used in this work, are always the result of calculating a matrix element between two dot states and invariably precede further integration which is performed by Simpson's rule. For example in expression 3.24, the integral in the Dirac brackets would be performed by DFT before being integrated over $\mathbf{q}$ by Simpson's rule. Therefore the points at which an integrand is known will be defined by our initial choice of sampling points and data range in the DFT. In cases where the integrand is to be evaluated at a position that does not coincide with a data point, a conversion to polar coordinates for example, we employ a three-dimensional linear interpolation scheme.

In some special cases, it is possible to calculate analytical expressions for the relaxation rate. We can then use these results to check the accuracy of the numerical methods in addition to the convergence test already mentioned. The results given in this chapter are found to be accurate to better than 0.1% using no more than 200 points.

3.5 Results and Discussion

Auger relaxation calculations have been performed in both the dipole approximation and exactly. In this section the two methods of calculating the relaxation rates are compared for the HO model as defined by expression 2.4 with $B = 0$. We also present the exact relaxation rates for more realistic QD models and discuss the effects of QD size and shape.

In the case of the HO model considered in the following section and square based truncated pyramid models discussed in section 3.5.4, the first excited state is degenerate. In general, any linear combination $(\sum a_{ij}\phi_j)$ of the degenerate states is a valid eigenfunction of the Hamiltonian. We must take this into account when calculating the relaxation rates and write the matrix element of the operator $\hat{V}$ as:

$$M_i = \left\langle \phi_0 \middle| \hat{V} \middle| \sum_j a_{ij}\phi_j \right\rangle = \sum_j a_{ij} \left\langle \phi_0 \middle| \hat{V} \middle| \phi_j \right\rangle \tag{3.33}$$

If we sum over all possible rates, the square magnitude of the matrix element becomes:

$$\begin{aligned} \sum_i |M_i|^2 &= \sum_{ijk} a_{ij}^* a_{ik} \left\langle \phi_0 \middle| \hat{V} \middle| \phi_j \right\rangle \left\langle \phi_k \middle| \hat{V} \middle| \phi_0 \right\rangle \\ &= \sum_{jk} \delta_{jk} \left\langle \phi_0 \middle| \hat{V} \middle| j \right\rangle \left\langle \phi_k \middle| \hat{V} \middle| \phi_0 \right\rangle = \sum_j \left| \left\langle \phi_0 \middle| \hat{V} \middle| \phi_j \right\rangle \right|^2 , \end{aligned} \tag{3.34}$$

where we have used the fact that $\sum a_{ij}\phi_j$ is an orthogonal set so that $\sum_i a_{ij}^* a_{ik} = \delta_{jk}$. It is easy to then calculate the relaxation rate for each of the degenerate states. In this work we will take the average of these two relaxation rates since a single electron captured into the dot may occupy either of the degenerate excited states with equal probability.

3.5.1 The Breakdown of the Dipole Approximation

We recall that in making the dipole approximation, extra terms were retained in the expansion of the Yukawa potential (Eq. 3.14). We return to the 2D exact and dipole relaxation rates given in expressions 3.13 and 3.17, and the 3D exact and dipole rates given by expressions 3.24 and 3.28 to gain an insight into the validity of this approximation.

We first consider relaxation from the first radial excited state to the ground state of a harmonic oscillator dot (expression 2.4). We find that the matrix elements for both the exact wetting layer and bulk relaxation mechanisms (expressions 3.13 and 3.24) contain a factor like:

$$\left\langle \phi_f\left(\mathbf{r}\right) \left| e^{i\mathbf{q}\cdot\mathbf{r}} \right| \phi_i\left(\mathbf{r}\right) \right\rangle = \frac{i\lambda q_\parallel}{2} \exp\left[-\frac{\lambda^2 q_\parallel^2}{4} - \frac{\lambda_z^2 q_\perp^2}{4} \right], \tag{3.35}$$

whereas our extended dipole approximations (expressions 3.17 and 3.28) contain the factor:

$$\left\langle \phi_f\left(\mathbf{r}\right) \left| i\mathbf{q}\cdot\mathbf{r} - \frac{i}{3!}\left(\mathbf{q}\cdot\mathbf{r}\right)^3 \right| \phi_i\left(\mathbf{r}\right) \right\rangle = \frac{i\lambda q_\parallel}{2} \left[1 - \frac{\lambda^2 q_\parallel^2}{4} - \frac{\lambda_z^2 q_\perp^2}{4} \right]. \tag{3.36}$$

Upon examination of the two expressions above it is obvious that making this approximation simply results in the expansion of the exponential factor appearing in the exact result:

$$\exp\left[-\frac{\lambda^2 q_\parallel^2}{4} - \frac{\lambda_z^2 q_\perp^2}{4} \right] \approx \left[1 - \frac{\lambda q_\parallel^2}{4} - \frac{\lambda_z q_\perp^2}{4} \right]. \tag{3.37}$$

The formal dipole approximation would be to truncate the expansion at unity. Obviously, truncating this expansion at unity is only valid provided that the product $\lambda q \ll 1$. However, we will demonstrate that this condition is unlikely to be satisfied for any realistic confinement energy ($\hbar\omega$).

In order to illustrate this result, we focus on the low temperature limit. We expect that prior to the relaxation process, the external electron will have negligible energy compared to the same electron after the relaxation process has taken place. Similarly, the initial and final wave vectors of the external electron are expected to have the relationship; $|\mathbf{k}_f| \gg |\mathbf{k}_i|$. We can then write the change in wave vector for the external electron as $\mathbf{q} = \mathbf{k}_f - \mathbf{k}_i \approx \mathbf{k}_f$. Since the loss of energy by the QD must be equal to the gain in energy of the external electron we find that:

$$\Delta E = \frac{\hbar^2}{2m^*}\left(k_f^2 - k_i^2\right) \approx \frac{\hbar^2 k_f^2}{2m^*} \approx \frac{\hbar^2 q^2}{2m^*}. \tag{3.38}$$

From this result and the definition of λ in Eq. 2.2, we find that $\lambda q \approx \sqrt{2\Delta E/\hbar\omega}$. However, recalling the definition of the energy levels for the HO model given by Eq. 2.5, we see that $\hbar\omega = \Delta E$. This gives the product $\lambda q \approx \sqrt{2}$ and so the criterion for application of the dipole approximation is not met.

This important result demonstrates that the dipole approximation is not valid for the HO model of any realistic size at least in the low temperature limit, but do other models suffer from the same difficulty? For the cylindrical HO model, the length parameter λ given by Eq. 2.2 is a convenient measure of the confinement of the dot wave function. However, for other QD models this length parameter is not so readily available. In order to make any meaningful comparison, a reasonable substitute must be found. The ground state of the HO model (see expression 2.4) yields the expectation values $< r^2 >= \lambda^2$. We might then anticipate that $\sqrt{< r^2 >}$ for other models will be a reasonable substitute for the length parameter λ in the HO model. Comparison of $q\sqrt{< r^2 >}$ should then give at least an indication of the validity of the dipole approximation for various dot models. This comparison is given in table 3.1.

Dot model	ΔE (eV)	$< r^2 >$ ($\times 10^{-16}$m^2)	λq
Cylindrical HO	$\hbar\omega/e$	λ^2	1.414
Square based pyramid	0.118	0.1235	0.937
Rectangular based truncated	0.061	0.2048	0.868
Square based truncated	0.073	0.2205	0.705

Table 3.1: Quantum dot models, a comparison of λq values.

Clearly, the validity of the dipole approximation is model dependent and the results given in table 3.1 would suggest that the HO model is the least applicable. However, the necessity that $\lambda q \ll 1$ for the dipole approximation to be valid is unlikely to be satisfied for any of the models considered here. It is usual for the dipole approximation to be applied in order to help simplify a calculation to a point where analytical relaxation rates can be found. Since analytic rates can be found for only the most simplified and frequently unrealistic models, it does not seem beneficial to apply the dipole approximation in any subsequent calculations.

The effect of the dipole approximation is evident in figures 3.2 and 3.3 and appears as an overestimation of the relaxation rate by a factor of approximately 3. The discrepancy is roughly constant over the temperature ranges discussed here since the product λq is constant. However, as the temperature is increased, the hypothesis given above will no longer be accurate. In this case the inequality

$|\mathbf{k}_f| \gg |\mathbf{k}_i|$ will no longer be valid and instead we find:

$$\lambda q = \left[2 \left(\frac{3E_i - E_f - 2\sqrt{2E_i - E_i E_f}}{E_i - E_f} \right) \right]^{1/2}, \tag{3.39}$$

where E_i and E_f are the initial and final QD energies respectively. As the energy levels of the dot move closer together ($\hbar\omega \to 0$), the product $\lambda q \to 0$ and the dipole approximation will become applicable. Unfortunately, this does not occur sufficiently rapidly for the dipole approximation to be applicable to self-assembled quantum dots.

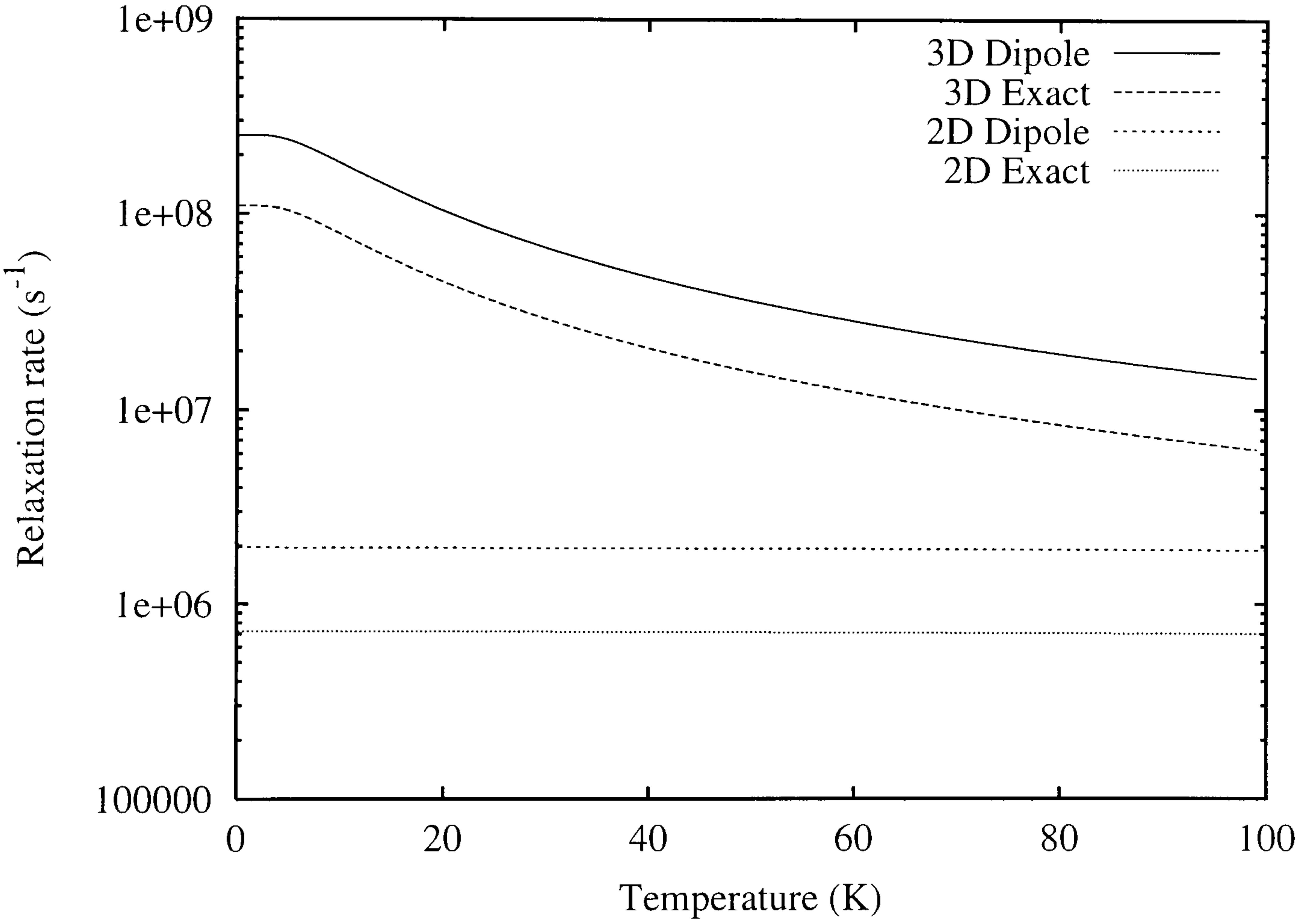

Figure 3.2: Relaxation rate against temperature for 2D and 3D Auger relaxation mechanisms in the dipole approximation and the exact calculation. For an injected carrier density of 10^{11}cm^{-3} and length parameters of $\lambda = 4.5\text{nm}$ and $\lambda_z = 2.2\text{nm}$.

It has been previously stated that the dipole approximation can be used to simplify the calculation to the point where analytical results can be found.

Using the methods explained in this chapter, we find that it is even possible to calculate exact analytic results for bulk scattering in certain special cases. For completeness, we illustrate this by considering the ground and first radially excited HO wave functions from expression 2.4. For one particular special case we can simplify expression 3.11 by assuming $\lambda = \lambda_z$ and $\kappa = z_0 = 0$. The 2D exact relaxation rate is then given by:

$$\frac{e^4 n_2 \lambda^2 m^*_{QD}}{32\pi\epsilon^2\epsilon_0^2\hbar^2 m^*_{WL}}\sqrt{\frac{2\pi m^*_{WL}}{k_B T}}\int_0^\infty \exp\left[-\alpha\left[\eta\left(q\right)\right]^2\right]\left[\text{erfc}\left(\frac{q\lambda}{2}\right)\right]^2 dq \tag{3.40}$$

where $\text{erfc}(x)$ is the complementary error function. In the strict dipole approximation, using the same simplifications, the 2D relaxation rate (Eq. 3.17) becomes:

$$\frac{e^4 n_2 m^*_{QD}\lambda^2}{32\pi\epsilon^2\epsilon_0^2\hbar^2 m^*_{WL}}\sqrt{\frac{2\pi m^*_{WL}}{k_B T}} \tag{3.41}$$

The 3D exact rate Eq. 3.21 is:

$$\frac{4\pi e^4 n_3 m^*_{QD}\lambda^2}{3\hbar^2\epsilon^2\epsilon_0^2}\sqrt{\frac{\pi}{2m^*_B k_B T}}K_0\left[\beta^2\sqrt{\frac{\alpha}{2}\left(\frac{\alpha}{2}+\lambda^2\right)}\right]\exp\left(\frac{\alpha\beta^2}{2}\right) \tag{3.42}$$

and the 3D dipole rate is:

$$\frac{4\pi e^4 n_3 m^*_{QD}\lambda^2}{3\hbar^2\epsilon^2\epsilon_0^2}\sqrt{\frac{\pi}{2m^*_B k_B T}}K_0\left[\frac{\alpha\beta^2}{2}\right]\exp\left(\frac{\alpha\beta^2}{2}\right) \tag{3.43}$$

where $K_0(x)$ is a modified Bessel function.

3.5.2 Temperature Dependence

HO relaxation rates for both wetting layer and bulk scattering mechanisms, both exactly and in the dipole approximations are plotted against temperature in figures 3.2 and 3.3. We have neglected thermal excitations which are expected to be negligible in undoped samples but may be important at higher temperatures if doping is significant. The rates given in figure 3.2 correspond to an injected

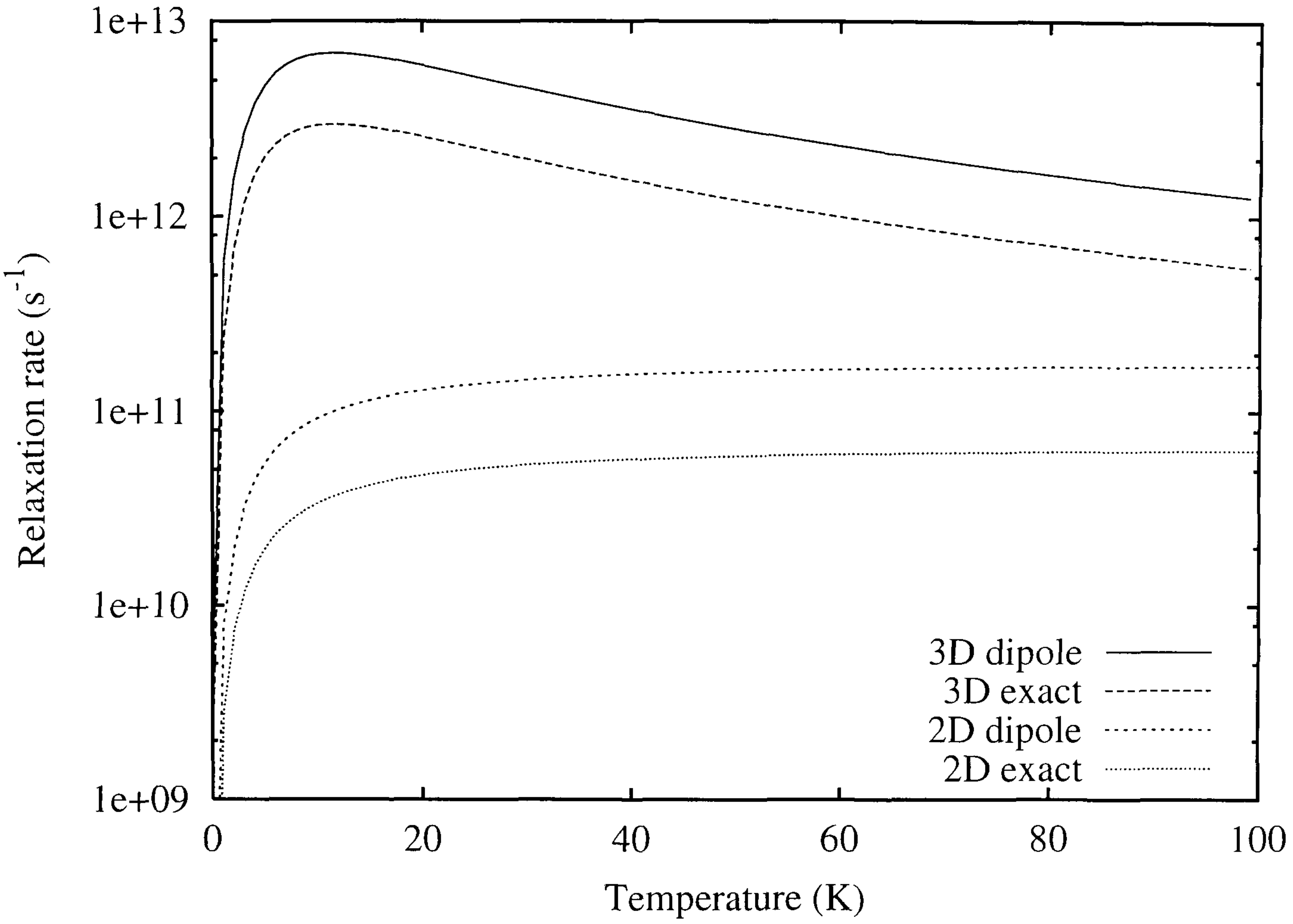

Figure 3.3: Relaxation rate against temperature for 2D and 3D Auger relaxation mechanisms in the dipole approximation and the exact calculation with an injected carrier density of $10^{16}\mathrm{cm}^{-3}$, length parameters of $\lambda = 4.5\mathrm{nm}$ and $\lambda_z = 2.2\mathrm{nm}$.

carrier density of $10^{11}\mathrm{cm}^3$ for which screening is small. The 2D relaxation rate is found to be approximately independent of temperature in agreement with Uskov *et al.* [9]. This temperature independence arises from the Boltzmann distribution used in calculating the 2D rate which is of the form $T^{-1}\exp(-E(k_i)/k_BT)$. Upon integration over q, the exponential gives a factor of T. This effectively cancels the inverse temperature dependence of the pre-factor leaving only the temperature dependence of the exponential. At extremely low temperatures ($<$ 1K not shown), the screening length κ also becomes large and leads to a strong suppression of the relaxation rate.

The Boltzmann distribution used in calculating the 3D rate has the form

$T^{-3/2}\exp(-E(k_i)/k_BT)$. The factor of T resulting from integration leaves the relaxation rate with a remaining $T^{-1/2}$ dependence accounting for the behaviour at $T \geq 5$K shown in figure 3.2. At lower temperatures, the screening length κ diverges as $T^{-\frac{1}{2}}$ and the integrand in Eq. 3.24 suppresses the relaxation rate.

As the carrier density is increased, screening becomes important. Figure 3.3 shows the relaxation rate for 2D and 3D mechanisms in both the dipole approximation and exact calculations for $n_p = 10^{16}\text{cm}^3$. The $T^{-\frac{1}{2}}$ dependence of the screening parameter κ accounts for the sharp reduction in relaxation rate at very low temperatures shown in figure 3.3. The dipole and exact rates converge at extremely low temperatures. With a high electron density, κ is large and at low temperatures is further increased by its $T^{-\frac{1}{2}}$ dependence. When the screening becomes large enough, the $[\kappa^2 + q^2]^{-2}$ factor in the integrand of expression 3.24 can be approximated as κ^{-4} which introduces a T^2 dependence in addition to the $T^{-\frac{1}{2}}$ from the pre-factor. The rate then goes like $T^{\frac{3}{2}}$ and the constant difference between the dipole and the exact rate vanishes as $T \longrightarrow 0$.

3.5.3 The Effect of Size

Figure 3.4 shows the HO relaxation rate against lateral confinement energy for both 2D and 3D scattering mechanisms. This allows us to explore the effect of varying QD size on the relaxation rate since the length parameter λ is dependent on the confinement energy $\hbar\omega_0$. We assume a temperature of 1K and an injected electron density (n_p) ranging between 10^{11} and 10^{16}cm^{-3} which corresponds to small and large screening respectively.

For $n_p = 10^{16}\text{cm}^{-3}$, screening is large and we find the relaxation rate for lateral excitations approaches a constant value for both 2D and 3D scattering when

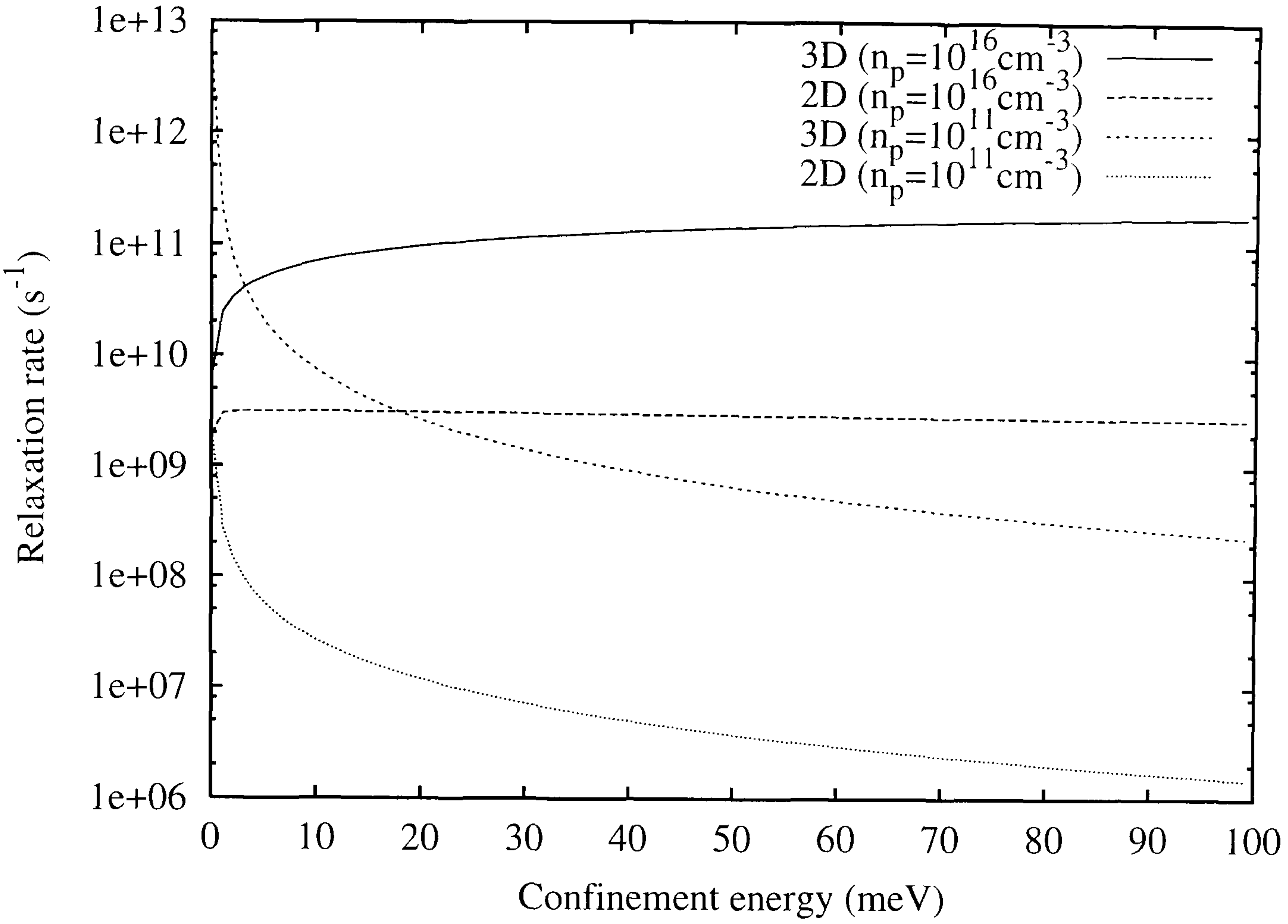

Figure 3.4: Relaxation rate against confinement energy for 2D and 3D Auger relaxation in the exact calculation for the HO model. Injected carrier densities $n_p = 10^{11}\text{cm}^{-3}$ and $n_p = 10^{16}\text{cm}^{-3}$ are used at a temperature of 1K. The small kinks in the plots at low confinement energies are due to a low point density.

vertical confinement is held constant and lateral confinement energy ($\hbar\omega_0$) is increased. The form of the 2D rate can be understood by considering the HO matrix element with $z_0 = 0$ found from expression 3.13 and Eq. 3.35 to be:

$$\frac{\lambda q}{\sqrt{\kappa^2+q^2}} \exp\left[\frac{-\lambda_z^2}{4}\left(\kappa^2+q^2\right) - \frac{\lambda^2 q^2}{4}\right] \text{erfc}\left(\frac{\lambda_z}{2}\sqrt{\kappa^2+q^2}\right) \tag{3.44}$$

In the large screening limit where $\kappa \gg q$ so that $\sqrt{\kappa^2+q^2} \approx \kappa$ the matrix element is approximately $\lambda q \kappa^{-1} \exp(-\lambda_z^2\kappa^2/4 - \lambda^2 q^2/4)\text{erfc}(\lambda_z\kappa/2)$. In section 3.5.1 we found that for lateral excitations, the product $\lambda q \approx \sqrt{2}$. The matrix element therefore becomes constant and the relaxation rate is independent of lateral QD size. At low confinement energies this approximation breaks down and the product $\lambda q \to 0$ as $\Delta E \to 0$ as shown in Eq. 3.39, consequently the relaxation rate decreases. At low screening ($n_p \approx 10^{11}\text{cm}^{-3}$) where κ can be ignored, the matrix element is approximately $\lambda \exp[-(\lambda^2 + \lambda_z^2)q^2/4]\text{erfc}(\lambda_z q/2)$. For high lateral confinement energies, $\text{erfc}(\lambda_z q/2) \to 0$ and the relaxation rate tends to zero whereas at low lateral confinement energies, $\text{erfc}(\lambda_z q/2) \to 1$ and the matrix element goes as λ.

In the 3D case, the matrix element becomes:

$$\frac{\lambda q_{\|}}{\kappa^2 + q^2} \exp\left(-\frac{\lambda^2 q_{\|}^2}{4} - \frac{\lambda_z^2 q_{\perp}^2}{4}\right), \tag{3.45}$$

For low temperatures and high confinement energies the relationship $\lambda q \approx \sqrt{2}$ again holds. In the large screening limit, the matrix element is approximately $\sqrt{2}\kappa^{-2} \cos\xi \exp[-\frac{1}{2}\cos^2\xi - \lambda_z^2(2\lambda^2)^{-1}\sin^2\xi]$ where ξ is the angle between the WL plane and the wave vector $\mathbf{q}$. The $\cos\xi$ factor favours a change of wave vector ($\mathbf{q}$) parallel to the WL plane and the matrix element is nearly independent of confinement energy when ξ is small. Therefore the relaxation rate is almost independent of confinement energy similar to the 2D case. However, there is a slight energy dependence caused by the non-zero perpendicular component of $\mathbf{q}$. In the low screening limit, the matrix element goes like q^{-1} where q is proportional to $\sqrt{\Delta E}$ and we find a rapid increase in relaxation rate as confinement energy tends to zero.

3.5.4 More Realistic Quantum Dot Models

Up to this point, we have considered only the HO model dot with wave functions given by expression 2.4. We now turn our attention to the effect shape and composition has on the relaxation rates by considering the more realistic dot models discussed in chapter 2. We consider the two square based dot models of truncated pyramid shape inspired by observations made by Bruls it et al. [14] and the rectangular based truncated pyramid model inspired by the observations of E. E. Vdovin *et al.* [50]. The asymmetry of the wave function in the rectangular based dot means that the excited states are not degenerate and the averaging procedure described in section 3.5 does not apply. The parameters for these models are given in table 2.1.

In addition to these three self assembled quantum dot models, we include two calculations for the HO model in order to explore the possibility of this simple model being used to accurately predict the relaxation rates in self-assembled quantum dots. The HO length parameters are fitted using two different methods. First, we use the method described in chapter 2 to fit the HO energy gap ($\hbar\omega$) to the truncated pyramid energy gap for the specific transition we wish to examine. This method leads to $\lambda = 6.66$nm and $\lambda_z = 4.68$nm for transitions between the first excited state and the ground state in a square based truncated pyramid quantum dot. The fitting of HO length parameter to the energy levels in this way must be specifically calculated for each transition. It should be noted that parameter fitting to the higher energy transitions can sometimes result in a highly unrealistic dot shape. For example, using this method for transitions between the second excited state and the ground state leads to $\lambda = 4.8$nm and $\lambda_z = 7.5$nm. This is unrealistic for self-assembled dots which invariably have a larger lateral than vertical size.

The second method is to match the HO length parameter to the truncated pyramid RMS displacement to give $\lambda = \sqrt{< r^2 > - < r >^2} = 4.47$nm and $\lambda_z = \sqrt{< z^2 > - < z >^2} = 2.41$nm. In both HO models we maintain the WL coordinate $z_0 = 2.5$nm in line with the truncated pyramid model and our definition of the coordinate origin.

The electron densities used to calculate the data in figures 3.5 through to 3.8 are calculated from the rate equations [28] given in equation 3.1 for an injected carrier density of between 10^{12} and 10^{18}cm^{-3}. The use of the same injected carrier density (n_p) for both 2D and 3D calculations allows us to directly compare these figures. At high carrier densities, the screening length κ will become short enough for the Yukawa potential to become inapplicable, although we do not expect the general physics to be affected.

Inspecting figures 3.5 and 3.6, we see that the HO rates do not match the self-assembled dot rates. The accuracy of the HO model to predict relaxation rates in self-assembled dots depends on a suitable choice of length parameter. The HO model does give a comparable 2D rate to the truncated pyramid when the energy levels are matched. Nevertheless, a comparison of the 2D HO rate with the corresponding truncated pyramid rate shows that the HO rate is smaller at low electron densities and hence low screening by a factor of approximately 1.3. This discrepancy changes slightly to a factor of approximately 2 at higher electron densities. The RMS deviation method of fitting HO parameters does not appear to be quite so accurate. At low electron densities the rate calculated for the HO model is smaller than the rate for the truncated pyramid model by a factor of over 3.5. This inaccuracy changes slightly to approximately 2.4 at higher electron densities but remains roughly constant throughout the range of electron densities considered here.

The 3D relaxation rate for the HO model suffers from similar underestimations. For the energy level fit the rate is underestimated by a factor of more than 2 which persists throughout the entire range of electron densities considered here. The

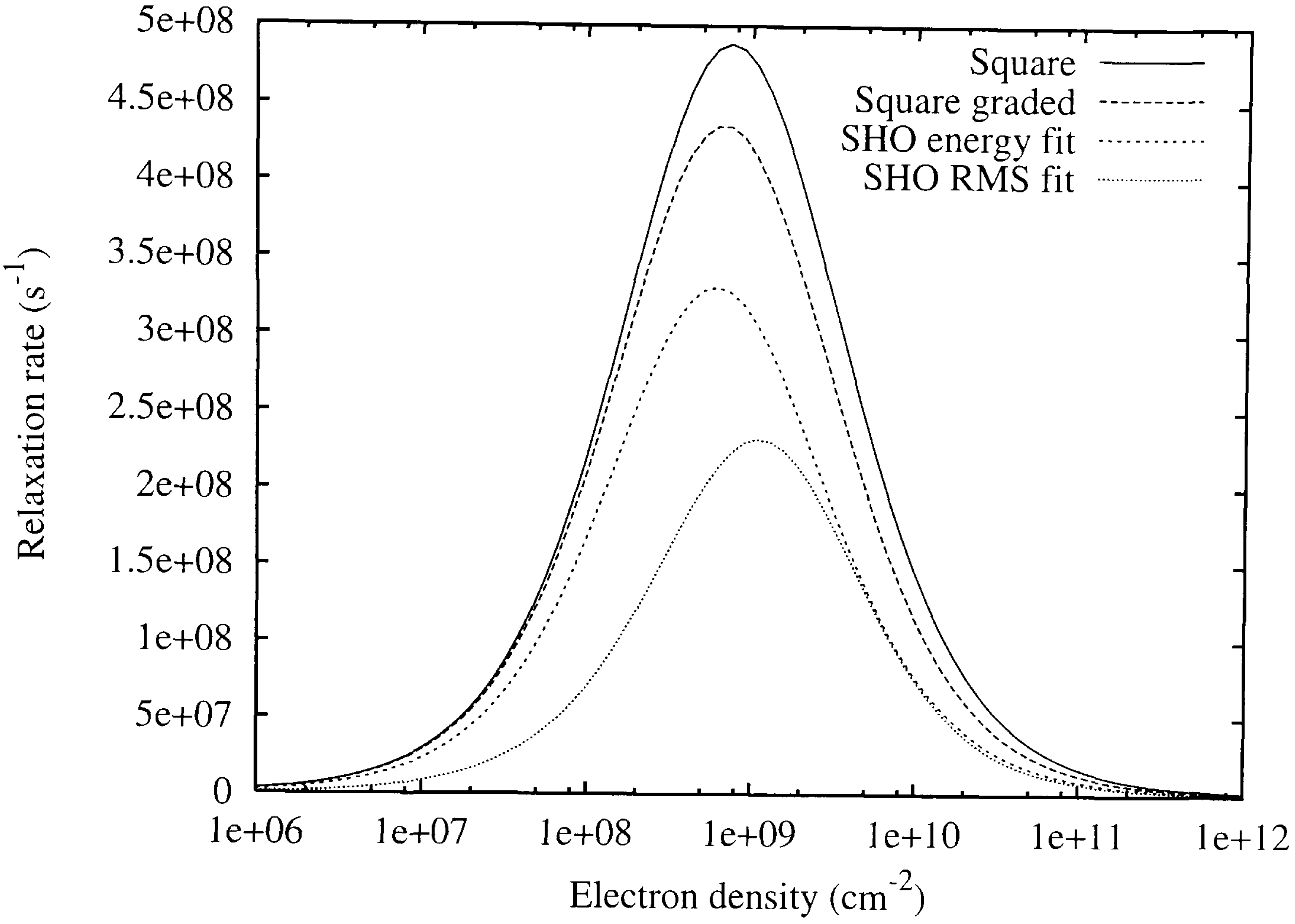

Figure 3.5: 2D Auger relaxation rate against WL electron density for a square based truncated pyramid (solid line), square based graded material truncated pyramid (coarse dotted line), HO model with the energy levels fitted to the square based truncated pyramid model (medium dotted line) and HO model with RMS deviation fitted to the square based truncated pyramid model (fine dotted line). With a temperature of 1K and an injected carrier density $n_p = 10^{12} - 10^{18}\text{cm}^{-3}$.

RMS deviation fit is too low by a factor of 6 at low electron densities which reduces to a factor of 1.2 at high electron densities.

The effect of confinement energy on the HO model is shown in figure 3.4 and in the low electron density, low screening limit, a decrease in confinement energy (increase in size, see Eq. 2.2) seems to strongly increase the rate. When the electron density is high, the increase in size has a mild effect in reducing the rate. This effect is seen in the two HO rates in figures 3.5 and 3.6 where the RMS

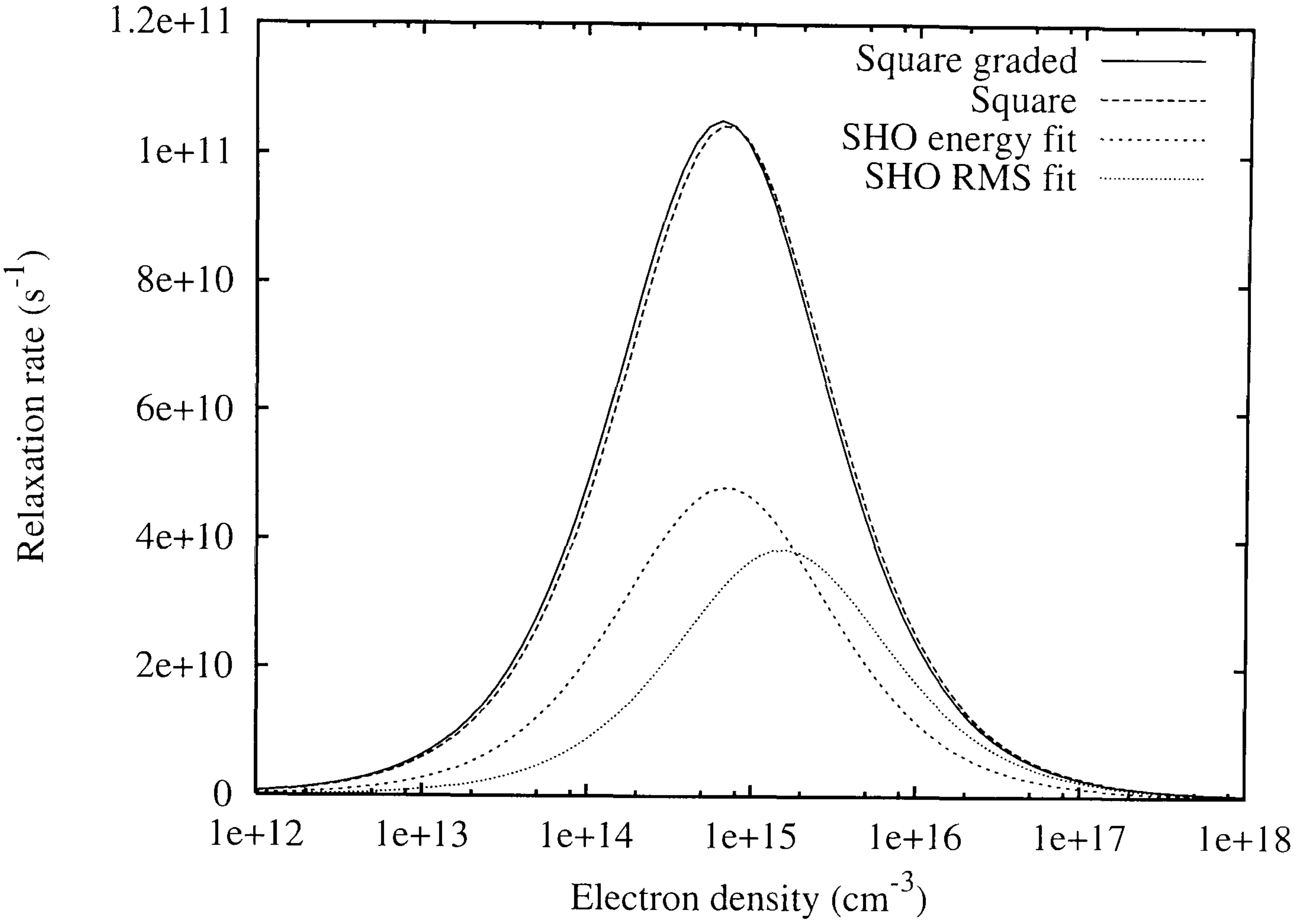

Figure 3.6: 3D Auger relaxation rate against bulk electron density for a square based graded material truncated pyramid (solid line), square based truncated pyramid (coarse dotted line), HO model with the energy levels fitted to the truncated pyramid model (medium dotted line) and HO model with RMS deviation fitted to the truncated pyramid model (fine dotted line). With a temperature of 1K for an injected carrier density $n_p = 10^{12} - 10^{18}\text{cm}^{-3}$

deviation fit has length parameters that are smaller than those calculated for the energy level fit. At low electron densities, the energy level fit has the higher relaxation rate whereas at higher electron densities the rates converge and in the case of bulk relaxation, they even cross over. In essence, for a smaller dot we see the peak value of the relaxation rate shift toward a higher electron density.

The 2D rates given in figure 3.5 are dependent on the parameter z_0 and the vertical length parameter λ_z. The overlap between the quantum dot wave function, which decays with the characteristic length λ_z, and the wetting layer wave function located at the point z_0 below the centre of the dot is clearly relevant. For the HO models considered here $z_0 = 2.5$nm and for parameters fitted to the RMS deviation where $\lambda_z = 2.41$nm we should expect a faster decay of the dot wave function compared to parameters fitted to the energy levels where $\lambda_z = 4.68$nm.

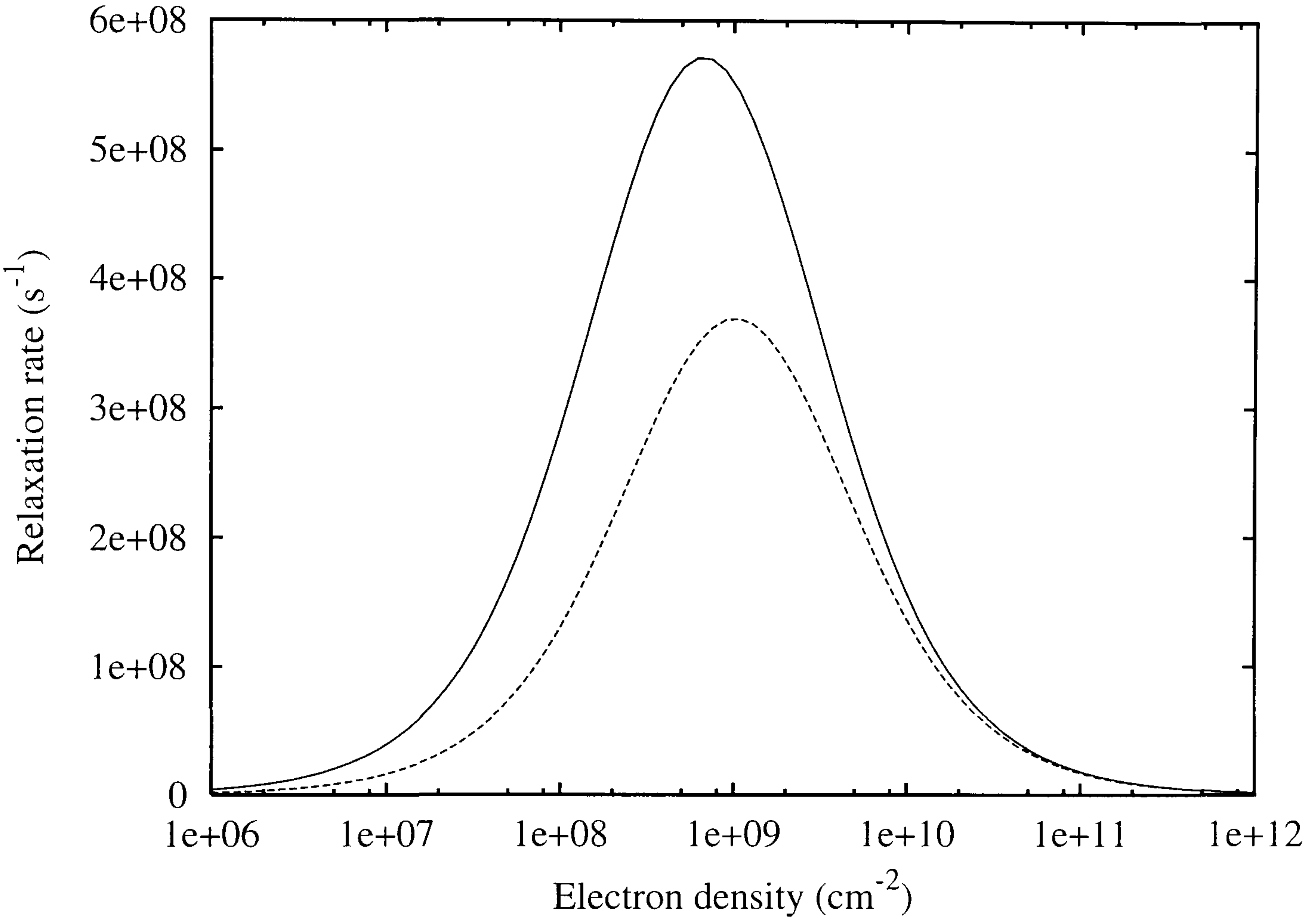

Figure 3.7: 2D Auger relaxation rate against bulk electron density for a rectangular based truncated pyramid dot. The solid line denotes transition between 1st excited and ground state and the dotted line denotes transitions between 2nd excited state and the ground state. Calculated at a temperature of 1K for an injected carrier density $n_p = 10^{12} - 10^{18}\text{cm}^{-3}$.

Comparing the self-assembled quantum dot models, we see that the composition of the dot has a small effect on the relaxation rate. In the case of 2D relaxation, the rate is suppressed slightly (by a factor of ≈ 0.89) in the graded material dot. This suppression can be attributed to the composition gradient confining the electrons higher in the dot thus reducing the overlap between the quantum dot and the wetting layer wave functions. For the square based models, we find the $< z >$ expectation value for the graded material dot is 2.25nm from the wetting layer, whereas for the pure InAs dot the same expectation value is only 2.06nm from the wetting layer. This is in general agreement with observations of Bruls *et al.* [14] and Fry *et al.* [59].

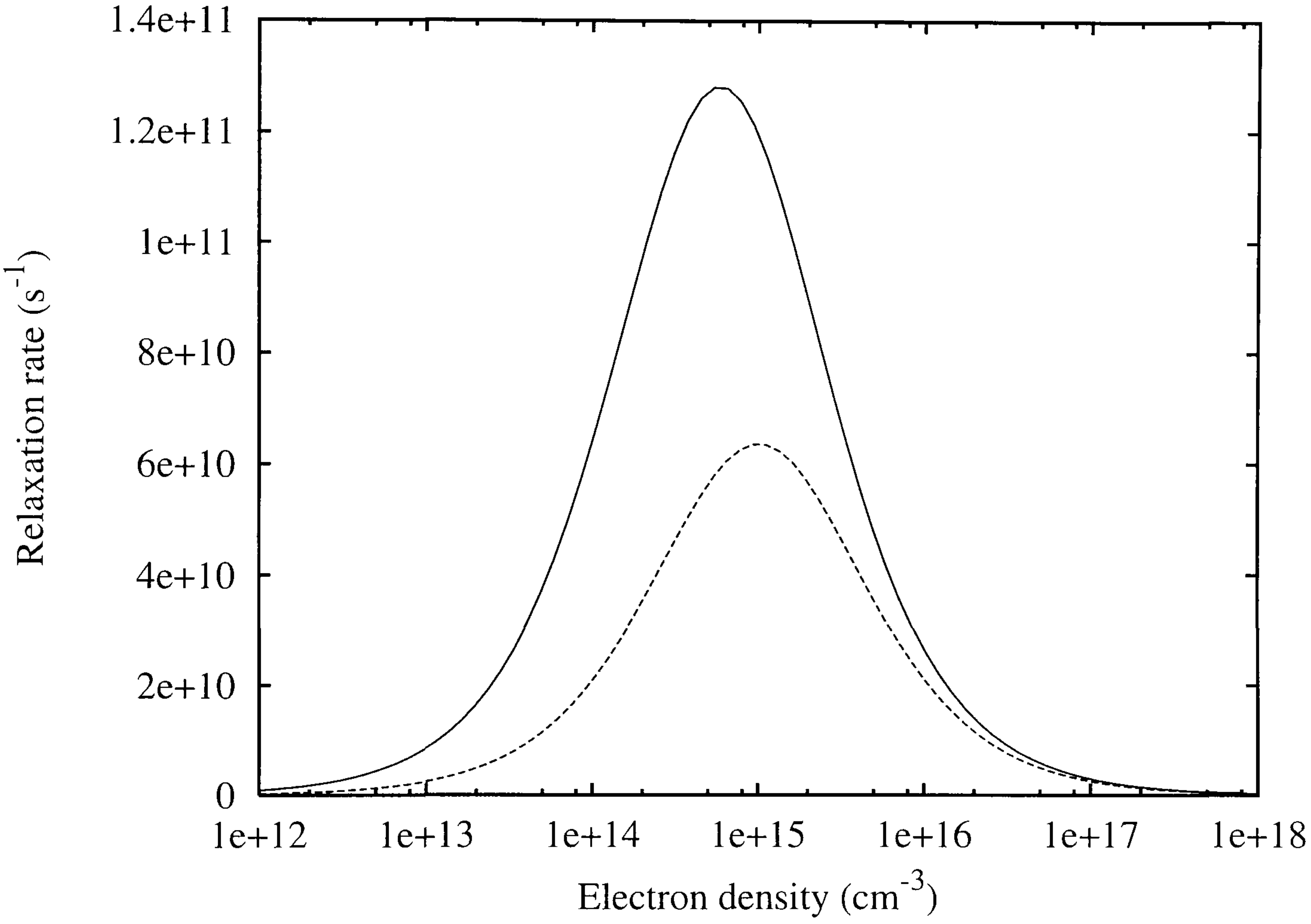

Figure 3.8: 3D Auger relaxation rate against bulk electron density for a rectangular based truncated pyramid dot. The solid line denotes transition between 1st excited and ground state and the dotted line denotes transitions between 2nd excited state and the ground state. Calculated at a temperature of 1K for an injected carrier density $n_p = 10^{12} - 10^{18}\mathrm{cm}^{-3}$.

The overlap between dot and wetting layer wave functions does not affect the 3D mechanism and so the effect of the composition gradient is much smaller. The composition gradient can only influence the relaxation rate by the effect it has on the dot wave function. The effective mass in $\mathrm{In_{0.8}Ga_{0.2}As}$ is approximately 1.4

times greater that the effective mass in pure InAs. This change in the effective mass causes the graded material dot to have a slightly smaller confinement energy and thus a slightly larger rate, especially at lower electron densities where screening is less important.

In figures 3.7 and 3.8, we compare the 2D and 3D relaxation mechanisms against electron density for two different transitions in a rectangular based truncated pyramid dot. The first transition considered is from an excitation in the long axis of the dot to the ground state with an energy difference of $\approx$ 60meV. The second is for transitions from an excitation in the short axis to the ground state with an energy difference of $\approx$ 110meV. The departure from the four fold rotational symmetry of the square based quantum dot to the two fold rotational symmetry of the rectangular based dot breaks the degeneracy of the first excited state and consequently splits the relaxation rate for the two transitions. The difference in the two rates can be considered analogous to the size dependence shown in figure 3.4 where the two relaxation rates correspond to excitations in either the long or short axis of the dot.

3.5.5 Conclusions

We have demonstrated that the dipole approximation is unlikely to be applicable to Auger relaxation rates in QD systems. For 2D and 3D HO relaxation rates, the dipole approximation overestimates the relaxation rates by a factor of approximately 3. This is attributed to the spreading of the energy levels as confinement energy is increased. We have shown that the size and shape of self-assembled quantum dots have a large effect on Auger relaxation rates. The HO wave functions can give qualitative indications of the physical behaviour of QD systems but are only able to give an estimate of the relaxation rate in real QDs if the parameters are chosen carefully. The relaxation times found in this work (less than 10ps) are comparable with experimental results of between 20 and 300ps observed by Morris *et al.* [8] but it is unknown if the electron densities used in this work are consistent with their experiment.

In comparing the 2D and 3D rates we notice that for all injected electron densities n_p, the 3D rate dominates by over 2 orders of magnitude. The relative magnitudes of the WL and bulk electron densities determined by the parameters used to calculate these densities [28] play a crucial role in selecting which mechanism dominates. That is not to say that there are no circumstances where WL scattering can become dominant, it is possible to conceive of a system where this may become the prevailing mechanism. However, it is unlikely that minor changes in the parameter values used to calculate the relative carrier densities would have any great effect on this result. The inclusion of a composition gradient in the QD model is expected to confine the charge density higher in the QD [14, 59] which does appear to have the effect of further reducing the 2D relaxation rate as shown in figure 3.5.

Chapter 4

Auger Relaxation in Two Particle Self-Assembled Quantum Dots

In this chapter we consider Auger relaxation in a two-particle quantum dot and explore the physics that arises from the Coulomb interaction between the confined electrons. The inclusion of a "spectator" electron might be expected to modify the Auger mechanism and we investigate what impact this may have on the relaxation rates. This chapter follows on from the discussion of Auger relaxation in single particle quantum dots given in chapter 3 and we consider the same dot models in order for a direct comparison to be made. We again consider the two scattering mechanisms where the dot electron scatters with electrons located in the wetting layer and the surrounding bulk material.

The screening mechanism we must also examine, is considered in two parts. The first is the screening of the Auger mechanism between the dot electron and the external scattering electron due to the electron density in the surrounding bulk material. This is identical to the screening mechanism considered in chapter 3. The second is screening of the Coulomb interaction between the two dot electrons again due to the electrons located in the surrounding bulk material.

Unfortunately, including this mechanism in the calculation turns out to be extremely computationally expensive. To calculate the relaxation rate as a function of electron density requires the dot wave functions to be determined explicitly for each point on the curve. Since the majority of the computing time is required to calculate the dot wave functions, the screening of the two dot electrons from each other is neglected in the majority of results. Full details of this screening mechanism are given in section 4.2.2. The effect of including this mechanism is given in section 4.4.2.

The chapter is organized as follows. First we provide a brief discussion of the previous work in this field (section 4.1) before providing a description of the method used to calculate the two particle quantum states (section 4.2). Section 4.2 also includes a discussion of non-interacting two particle Slater determinants and how they are used as a basis set for the system Hamiltonian, which is described in section 4.2.1. The Coulomb matrix elements needed to calculate the interaction between the two dot electrons are discussed in section 4.2.2.

With the quantum states calculated, we turn our attention to the Auger relaxation rate in section 4.3. We first calculate the bulk relaxation rate in section 4.3.1 and then the wetting layer relaxation rate in section 4.3.2. In section 4.4 we present the results for the two scattering mechanisms and compare them to the single particle rates calculated in chapter 3 before giving the conclusions in section 4.5.

4.1 Previous Work

The single particle Auger relaxation mechanisms that have attracted attention recently (see section 3.1) have been primarily concerned with dot electrons scattering with electrons located in the wetting layer. Scattering of dot electrons with electrons located in the surrounding bulk however, does not appear to have attracted the same consideration. Similarly, the extension of the single particle calculations to include a second particle confined in the dot has also been overlooked. To date, the author is unaware of any calculations concerning two particle Auger relaxation rates in self-assembled quantum dots.

Auger relaxation in two particle self-assembled quantum dots may not have attracted significant attention, but there has been some interest in two particle relaxation processes in other types of quantum dot system, specifically the chemically produced colloidal nanoparticle. Auger relaxation rates in single and many particle spherical nanoparticles have been calculated using the Golden rule by J. L. Pan [60]. The energy spectrum of two particle colloidal nanoparticles was calculated by A. Franceschetti *et al.* [61] using a pseudopotential method. The same group then went on to make pseudopotential calculations of Auger relaxation rates in CdSe colloids where dot electrons scattered with holes also confined in the dot. Their results are presented in the paper by L. W. Wang *et al.* [62].

4.2 The Two Particle Dot States

In this section, we discuss the method of calculating the eigenstates for the interacting two-particle system. This is done by the exact diagonalisation of the two particle Hamiltonian matrix, constructed with a suitable basis set. For non-interacting two particle systems, the quantum states can be expressed as a Slater determinant of the form:

$$\begin{aligned}\Psi\left(\mathbf{r}_1,\mathbf{r}_2\right) &= \frac{1}{\sqrt{2}}\left[\Phi_1\left(\mathbf{r}_1\right)\Phi_2\left(\mathbf{r}_2\right)\chi^{(1)}_{m_{s1}}\chi^{(2)}_{m_{s2}} - \Phi_1\left(\mathbf{r}_2\right)\Phi_2\left(\mathbf{r}_1\right)\chi^{(2)}_{m_{s1}}\chi^{(1)}_{m_{s2}}\right]\\ &= \frac{1}{\sqrt{2}}\sum_p\left(-1\right)^p P\Phi_1\left(\mathbf{r}_1\right)\chi^{(1)}_{m_{s1}}\Phi_1\left(\mathbf{r}_2\right)\chi^{(2)}_{m_{s2}},\end{aligned} \tag{4.1}$$

where $\phi_i(\mathbf{r})$ are the spatial states, χ_{m_s} are the spin states for spin quantum number m_s and P is the permutation operator. We can write this Slater determinant in terms of symmetric and antisymmetric functions:

$$\begin{aligned}\Psi\left(\mathbf{r}_1,\mathbf{r}_2\right) &= \frac{1}{2\sqrt{2}}\left[\Phi_1\left(\mathbf{r}_1\right)\Phi_2\left(\mathbf{r}_2\right)+\Phi_1\left(\mathbf{r}_2\right)\Phi_2\left(\mathbf{r}_1\right)\right]\left[\chi^{(1)}_{m_{s1}}\chi^{(2)}_{m_{s2}} - \chi^{(2)}_{m_{s1}}\chi^{(1)}_{m_{s2}}\right]\\ &+\frac{1}{2\sqrt{2}}\left[\Phi_1\left(\mathbf{r}_1\right)\Phi_2\left(\mathbf{r}_2\right)-\Phi_1\left(\mathbf{r}_2\right)\Phi_2\left(\mathbf{r}_1\right)\right]\left[\chi^{(1)}_{m_{s1}}\chi^{(2)}_{m_{s2}} + \chi^{(2)}_{m_{s1}}\chi^{(1)}_{m_{s2}}\right]\\ &= \frac{1}{\sqrt{2}}\left[\psi^s\chi^a+\psi^a\chi^s\right].\end{aligned} \tag{4.2}$$

The antisymmetric spin function corresponds to total spin 0 and the symmetric spin function corresponds to total spin 1. Using this notation, we can choose our basis set to be the eigenstates of total spin 0 or 1 depending on our needs. In this work, we choose the basis set such that the eigenstates can be written in the form:

$$\Psi\left(\mathbf{r}_1,\mathbf{r}_2\right) = \sum_n\frac{a_n}{\sqrt{2}}\left[\Phi_{n_1}\left(\mathbf{r}_1\right)\Phi_{n_2}\left(\mathbf{r}_2\right)\pm\Phi_{n_1}\left(\mathbf{r}_2\right)\Phi_{n_2}\left(\mathbf{r}_1\right)\right], \tag{4.3}$$

where the + sign corresponds to states of total spin 0, the − sign determines states of total spin 1, a_n is the complex amplitude of each term in the eigenvector found by the diagonalisation of the two particle Hamiltonian matrix.

The use of an infinite basis set would theoretically lead to the exact energy eigenvalues and eigenstates. However, in practice this process would be unworkable and we take the usual method of truncating the basis set at a suitable point. This point is chosen by increasing the number of basis states and testing the convergence of the calculated energy eigenvalues. The basis set is truncated when the energy eigenvalues converge to within 0.1%.

In order to minimise the number of basis states we must include to achieve converged results, we choose to expand the two particle states in terms of the single particle states of the system under investigation. In this work we will use both the HO states given by expression 2.4 and the single particle states of M. Roy [17, 48] introduced in chapter 2. These states have all been used to calculate the single particle relaxation rates in chapter 3. This will enable us to make a direct comparison with the two particle rates calculated in this chapter.

4.2.1 The Hamiltonian

The Hamiltonian used to describe the N particle quantum dot system is given by:

$$\hat{H} = \sum_{i=1}^{N} \hat{h}_i + \frac{1}{2} \sum_{i=1}^{N} \sum_{\substack{j=1 \\ j \neq i}}^{N} \frac{e^2}{4\pi\epsilon\epsilon_0} \frac{\exp\left(-\kappa \left|\mathbf{r}_i - \mathbf{r}_j\right|\right)}{\left|\mathbf{r}_i - \mathbf{r}_j\right|}. \tag{4.4}$$

For the self-assembled dots modelled by M. Roy *et al.* [17, 48], $\hat{h}_i$ is given by Eq. 2.7 which allows for the possibility of a position dependent effective mass. The confinement potential $V(\mathbf{r})$ in Eq. 2.7 is a sum of terms describing the potential due to the band offset and the modification to this potential by the material strain. For the HO model (Eq. 2.4), a position dependent effective mass is not required and we have $\hat{h}_i = -(\hbar^2/2m^*)\nabla_i^2 + V(\mathbf{r}_i)$. In this case, the confinement $V(\mathbf{r}_i)$ is a harmonic oscillator potential characterised by the frequencies relating to the length parameters given by Eq. 2.2. The second term in Eq. 4.4 describes the Coulomb interaction between the N non-interacting particles.

The Schrödinger equation of the system is then simply $\hat{H}\Psi = E\Psi$ where Ψ is a function of the spatial and spin coordinates of all the electrons in the system. In our two-particle case this is either a sum of Slater determinants (spin 1) or the difference of two Slater determinants (spin 0) as defined by Eq. 4.3. Once the matrix elements have been calculated, diagonalisation of the Hamiltonian is performed by a "black box" routine supplied by the Numerical Algorithms Group [49]. Typically, fast convergence of the two particle states means that the largest matrices used in this work are of the order 200 × 200.

4.2.2 The Coulomb Matrix Elements

In order to construct the matrix needed to find the two particle eigenstates we must calculate the Coulomb matrix elements. To do this, we take the matrix element of the Coulomb operator given by the second term in Eq. 4.4 between two particle basis states. The Coulomb matrix element between the nth and mth basis state will have the form:

$$\int \frac{1}{\sqrt{2}} \left[\Phi_{n_1}(\mathbf{r}_1)\Phi_{n_2}(\mathbf{r}_2) \pm \Phi_{n_1}(\mathbf{r}_2)\Phi_{n_2}(\mathbf{r}_1)\right] \left[\frac{e^2}{4\pi\epsilon\epsilon_0}\frac{\exp\left(-\kappa\left|\mathbf{r}_1-\mathbf{r}_2\right|\right)}{\left|\mathbf{r}_1-\mathbf{r}_2\right|}\right]$$
$$\frac{1}{\sqrt{2}}\left[\Phi_{m_1}(\mathbf{r}_1)\Phi_{m_2}(\mathbf{r}_2) \pm \Phi_{m_1}(\mathbf{r}_2)\Phi_{m_2}(\mathbf{r}_1)\right] d\mathbf{r}_1 d\mathbf{r}_2, \tag{4.5}$$

where the + sign corresponds to states of total spin 0 and the − sign, states of total spin 1 as previously stated. In order to evaluate the Coulomb matrix element given by Eq. 4.5 we write the Yukawa potential (Eq. 3.3) as a Fourier transform:

$$\frac{e^2}{4\pi\epsilon\epsilon_0}\frac{\exp\left(-\kappa\left|\mathbf{r}_1-\mathbf{r}_2\right|\right)}{\left|\mathbf{r}_1-\mathbf{r}_2\right|} = \frac{e^2}{8\pi^3\epsilon\epsilon_0}\int \frac{1}{\kappa^2+q^2}\exp\left[i\mathbf{q}\cdot(\mathbf{r}_1-\mathbf{r}_2)\right]d\mathbf{q}. \tag{4.6}$$

Substituting this result into expression 4.5, the Coulomb matrix elements are found to be a sum of integrals, each of which has the form:

$$\begin{aligned} & \frac{e^2}{16\pi^3\epsilon\epsilon_0}\int\frac{1}{\kappa^2+q^2}\int \Phi_i^*(\mathbf{r}_1)\Phi_j^*(\mathbf{r}_2)e^{i\mathbf{q}\cdot(\mathbf{r}_1-\mathbf{r}_2)}\Phi_k^*(\mathbf{r}_1)\Phi_l^*(\mathbf{r}_2)\,d\mathbf{r}_1 d\mathbf{r}_2 d\mathbf{q} \\ = & \frac{e^2}{16\pi^3\epsilon\epsilon_0}\int\frac{1}{\kappa^2+q^2}\int \Phi_i^*(\mathbf{r}_1)\exp\left(i\mathbf{q}\cdot\mathbf{r}_1\right)\Phi_k^*(\mathbf{r}_1)\,d\mathbf{r}_1 \times \\ & \int \Phi_j^*(\mathbf{r}_2)\exp\left(-i\mathbf{q}\cdot\mathbf{r}_2\right)\Phi_l^*(\mathbf{r}_2)\,d\mathbf{r}_2 d\mathbf{q}. \end{aligned} \tag{4.7}$$

The single particle wave functions considered here are either HO wave functions or, in the case of the more realistic SAQD models, comprised of a sum of HO wave functions ($\Phi = \sum b_n \phi_n$) so the $\mathbf{r}$ integrals in Eq. 4.7 have the general form:

$$\int \left[\sum b_n^* \phi_n^* (\mathbf{r})\right] \exp\left(\pm i \mathbf{q} \cdot \mathbf{r}\right) \left[\sum b_m' \phi_m (\mathbf{r})\right] d\mathbf{r}. \tag{4.8}$$

The SAQD wave functions can contain of a large number of HO basis states. For this reason we proceed by calculating the Coulomb matrix elements numerically. First, we compute $\sum b_n^* \phi_n^*(\mathbf{r})$ and $\sum b_m' \phi_m(\mathbf{r})$ and then perform the integral in expression 4.8 via a standard discrete Fourier transform routine supplied by the Numerical Algorithms Group [49], applied using the methods discussed in section 3.4. To reduce the number of DFT operations required for the numerical evaluation of Eq. 4.7 we employ the relation:

$$\langle \phi_b (\mathbf{r}) \left| \exp\left(i \mathbf{q} \cdot \mathbf{r}\right) \right| \phi_a (\mathbf{r}) \rangle = \left[\langle \phi_a (\mathbf{r}) \left| \exp\left(-i \mathbf{q} \cdot \mathbf{r}\right) \right| \phi_b (\mathbf{r}) \rangle \right]^* . \tag{4.9}$$

The Fourier transforms in Eq. 4.7 are calculated in Cartesian coordinates but the $\mathbf{q}$ integral is done in spherical polar coordinates to avoid divergence problems that arise when screening is neglected ($\kappa = 0$). A three-dimensional linear interpolation scheme is employed to evaluate the integrand at the unknown points as mentioned in section 3.4.

4.3 The Relaxation Rate

In this section, we will outline the methods used to calculate the Auger relaxation rates for two electron quantum dots. We assume that the dot is prepared in an excited state. One of the electrons is then able to relax by scattering with electrons located in either the surrounding bulk material or the wetting layer via the mechanisms described in chapter 3. The calculations presented here can be thought of as an expansion of the work discussed in chapter 3 to include the effects of the Coulomb interaction due to an extra "spectator" electron confined inside the quantum dot.

4.3.1 Three Dimensional Auger rate

The two particle wave functions have been calculated using the method described in section 4.2 and are expressed in the form given in Eq. 4.3. The expansion coefficients (a_n) are found by the exact diagonalisation of the Hamiltonian matrix as described in section 4.2.1. The symmetric and antisymmetric wave functions correspond to spin 0 and spin 1 states respectively. In this section, all vectors are three-dimensional and are denoted in a lowercase bold font.

The potential used for calculating the Auger rate is a two-particle extension of the Yukawa potential given in Eq. 3.3:

$$u\left(\mathbf{r}_0, \mathbf{r}_1, \mathbf{r}_2\right) = \frac{e^2}{4\pi\epsilon\epsilon_0}\left[\frac{e^{-\kappa|\mathbf{r}_1-\mathbf{r}_0|}}{|\mathbf{r}_1-\mathbf{r}_0|}+\frac{e^{-\kappa|\mathbf{r}_2-\mathbf{r}_0|}}{|\mathbf{r}_2-\mathbf{r}_0|}\right]. \tag{4.10}$$

The quantum dot wave functions are highly localised but by comparison the bulk wave functions are highly extended. Although technically the exchange term between these functions should be included, we expect it to be negligible and by ignoring it we should not compromise accuracy significantly. For this reason we take the wave functions to be the product of the dot and bulk states. We assume that the bulk carriers are described by plane waves of the form $V^{-\frac{1}{2}}\exp(\imath\mathbf{k}\cdot\mathbf{r})$. We use dot wave functions of the form given by Eq. 4.3 and a potential of the form given by Eq. 4.10. The matrix element that appears in the Golden Rule (expression 3.2) is then given by:

$$\frac{e^2}{8\pi\epsilon\epsilon_0 V}\int \exp\left[i\left(\mathbf{k}_f-\mathbf{k}_i\right)\cdot\mathbf{r}_0\right]\sum_n a_n^*\left[\phi_{n_1}^*\left(\mathbf{r}_1\right)\phi_{n_2}^*\left(\mathbf{r}_2\right)\pm\phi_{n_1}^*\left(\mathbf{r}_2\right)\phi_{n_2}^*\left(\mathbf{r}_1\right)\right]\times$$
$$\left[\frac{e^{-\kappa|\mathbf{r}_1-\mathbf{r}_0|}}{|\mathbf{r}_1-\mathbf{r}_0|}+\frac{e^{-\kappa|\mathbf{r}_2-\mathbf{r}_0|}}{|\mathbf{r}_2-\mathbf{r}_0|}\right]\times$$
$$\sum_m a_m'\left[\phi_{m_1}\left(\mathbf{r}_1\right)\phi_{m_2}\left(\mathbf{r}_2\right)\pm\phi_{m_1}\left(\mathbf{r}_2\right)\phi_{m_2}\left(\mathbf{r}_1\right)\right]d\mathbf{r}_0 d\mathbf{r}_1 d\mathbf{r}_2. \tag{4.11}$$

We rewrite expression 4.11, to give:

$$\frac{e^2}{8\pi\epsilon\epsilon_0 V}\int \exp\left(i\left(\mathbf{k}_f-\mathbf{k}_i\right)\cdot\mathbf{r}_0\right)\left[\frac{e^{-\kappa|\mathbf{r}_1-\mathbf{r}_0|}}{|\mathbf{r}_1-\mathbf{r}_0|}+\frac{e^{-\kappa|\mathbf{r}_2-\mathbf{r}_0|}}{|\mathbf{r}_2-\mathbf{r}_0|}\right]\times$$
$$\sum_{nm} a_n^* a_m'\left[\phi_{n_1}^*\left(\mathbf{r}_1\right)\phi_{n_2}^*\left(\mathbf{r}_2\right)\phi_{m_1}\left(\mathbf{r}_1\right)\phi_{m_2}\left(\mathbf{r}_2\right)\pm\right.$$
$$\phi_{n_1}^*\left(\mathbf{r}_1\right)\phi_{n_2}^*\left(\mathbf{r}_2\right)\phi_{m_1}\left(\mathbf{r}_2\right)\phi_{m_2}\left(\mathbf{r}_1\right)\pm\phi_{n_1}^*\left(\mathbf{r}_2\right)\phi_{n_2}^*\left(\mathbf{r}_1\right)\phi_{m_1}\left(\mathbf{r}_1\right)\phi_{m_2}\left(\mathbf{r}_2\right)+$$
$$\left.\phi_{n_1}^*\left(\mathbf{r}_2\right)\phi_{n_2}^*\left(\mathbf{r}_1\right)\phi_{m_1}\left(\mathbf{r}_2\right)\phi_{m_2}\left(\mathbf{r}_1\right)\right]d\mathbf{r}_0 d\mathbf{r}_1 d\mathbf{r}_2. \tag{4.12}$$

From expression 4.12 we see that the $\mathbf{r}_0$ integral is similar to that of Eq. 3.19 and written explicitly is:

$$\int\left[\frac{e^{-\kappa|\mathbf{r}_1-\mathbf{r}_0|}}{|\mathbf{r}_1-\mathbf{r}_0|}+\frac{e^{-\kappa|\mathbf{r}_2-\mathbf{r}_0|}}{|\mathbf{r}_2-\mathbf{r}_0|}\right]\exp\left(i\left(\mathbf{k}_f-\mathbf{k}_i\right)\cdot\mathbf{r}_0\right)d\mathbf{r}_0$$
$$=\frac{4\pi}{\kappa^2+\left|\mathbf{k}_f-\mathbf{k}_i\right|^2}\left[\exp\left(i\left(\mathbf{k}_f-\mathbf{k}_i\right)\cdot\mathbf{r}_1\right)+\exp\left(i\left(\mathbf{k}_f-\mathbf{k}_i\right)\cdot\mathbf{r}_2\right)\right]. \tag{4.13}$$

We substitute this result into expression 4.12. It is clear that for each of the four terms in the sum over n and m, the first term in the $\exp[i(\mathbf{k}_f-\mathbf{k}_i)\cdot\mathbf{r}_1)]+\exp[i(\mathbf{k}_f-\mathbf{k}_i)\cdot\mathbf{r}_2)]$ factor from Eq. 4.13 will give a Fourier transform over the $\mathbf{r}_1$ coordinate and an orthogonality integral over the $\mathbf{r}_2$ coordinate. The second term will give the reverse. The orthogonality integral for normalised wave functions is just a delta function. This gives the matrix element as:

$$\frac{-e^2}{\epsilon\epsilon_0 V\left[\kappa^2+\left|\mathbf{k}_f-\mathbf{k}_i\right|^2\right]}F_{\pm}\left(\mathbf{k}_f-\mathbf{k}_i\right), \tag{4.14}$$

where

$$F_{\pm}\left(\mathbf{k}_f-\mathbf{k}_i\right)=\sum_{nm} a_n^* a_m' \left\{\delta_{n2,m2}\left\langle\phi_{n_1}\left(\mathbf{r}\right)\left|e^{i(\mathbf{k}_f-\mathbf{k}_i)\cdot\mathbf{r}}\right|\phi_{m_1}\left(\mathbf{r}\right)\right\rangle+\right.$$
$$\delta_{n1,m1}\left\langle\phi_{n_2}\left(\mathbf{r}\right)\left|e^{i(\mathbf{k}_f-\mathbf{k}_i)\cdot\mathbf{r}}\right|\phi_{m_2}\left(\mathbf{r}\right)\right\rangle \pm \delta_{n1,m2}\left\langle\phi_{n_2}\left(\mathbf{r}\right)\left|e^{i(\mathbf{k}_f-\mathbf{k}_i)\cdot\mathbf{r}}\right|\phi_{m_1}\left(\mathbf{r}\right)\right\rangle \pm$$
$$\left.\delta_{n2,m1}\left\langle\phi_{n_2}\left(\mathbf{r}\right)\left|e^{i(\mathbf{k}_f-\mathbf{k}_i)\cdot\mathbf{r}}\right|\phi_{m_1}\left(\mathbf{r}\right)\right\rangle\right\}. \tag{4.15}$$

The ± signs denote states of total spin 0 and 1 respectively.

Substituting expression 4.14 into the Golden Rule (expression 3.2) gives the relaxation rate as:

$$A\int\frac{\exp\left(-\alpha k_i^2\right)}{\left[\kappa^2+\left|\mathbf{k}_f-\mathbf{k}_i\right|^2\right]^2}\left|F_{\pm}\left(\mathbf{k}_f-\mathbf{k}_i\right)\right|^2\delta\left(k_f^2-k_i^2-\beta^2\right)d\mathbf{k}_f d\mathbf{k}_i, \tag{4.16}$$

where $F_{\pm}(\mathbf{k}_f-\mathbf{k}_i)$ is given by Eq. 4.15 and

$$A=\frac{4e^4 m^* n_3}{\pi^2\epsilon^2\epsilon_0^2}\left(\frac{\pi}{2m^* k_B T}\right)^{\frac{3}{2}}$$
$$\alpha=\frac{\hbar^2}{2m^* k_B T}$$
$$\beta=\sqrt{\frac{2m^*\left(E_i-E_f\right)}{\hbar^2}}. \tag{4.17}$$

We make the substitution $\mathbf{k}_f=\mathbf{q}+\mathbf{k}_i$ and write the delta function in expression 4.16 as $\delta\left(q^2-\beta^2+2|\mathbf{q}||\mathbf{k_i}|\cos\theta\right)$ following the same method given in sections 3.2 and 3.3. We make the change of variable $\cos\theta=x$ as in section 3.2.1. This allows us to rearrange the delta function so that the x integral is given by Eq. 3.22. This change of variable affects the lower limit on the $\mathbf{k}_i$ integral in the same way as it did in Eq. 3.10. The $\mathbf{k}_i$ integral is then given by Eq. 3.23 and the two particle Auger relaxation rate for scattering by electrons located in the bulk material is:

$$\frac{2e^4 m^* n_3}{\hbar^2\epsilon^2\epsilon_0^2}\sqrt{\frac{\pi}{2m^* k_B T}}\int\frac{1}{|\mathbf{q}|}\left[\kappa^2+q^2\right]^{-2}\left|F_{\pm}\left(\mathbf{q}\right)\right|^2\exp\left[-\alpha\left(\frac{q^2-\beta^2}{2\left|\mathbf{q}\right|}\right)^2\right]d\mathbf{q}. \tag{4.18}$$

We can compare this to the equivalent single particle rate given by expression 3.24. The only difference between the two is the factor $F(\mathbf{q})$ which is given by

$< \phi_f(\mathbf{r})|\exp(i\mathbf{q}\cdot\mathbf{r})|\phi_i(\mathbf{r}) >$ in expression 3.24 and given by Eq. 4.15 in the present case.

4.3.2 Two Dimensional Auger Relaxation

In this section, we consider scattering of an electron in a two-particle quantum dot with electrons located in the wetting layer. We define vectors denoted by upper case letters to be three-dimensional whereas vectors denoted by lower case letters are two-dimensional, consistent with the convention used in section 3.2.

We begin with the Yukawa potential given in Eq 4.10 and take its Fourier transform to give:

$$\frac{e^2}{8\pi^3\epsilon\epsilon_0}\int\frac{\exp\left(-i\mathbf{Q}'\cdot(\mathbf{R}_1-\mathbf{R}_0)\right)}{\kappa^2+Q'^2}+\frac{\exp\left(-i\mathbf{Q}'\cdot(\mathbf{R}_2-\mathbf{R}_0)\right)}{\kappa^2+Q'^2}d\mathbf{Q}'. \tag{4.19}$$

We assume that the WL wave functions are plane waves of the form $A^{-\frac{1}{2}}\exp(-i\mathbf{k}\cdot\mathbf{r})$, where A is the area of the wetting layer, and that the dot wave functions are of the form given by Eq. 4.3. Neglecting the exchange term, the matrix element appearing in the Golden rule (expression 3.2) is given by:

$$\begin{aligned}&\frac{e^2}{16\pi^3\epsilon\epsilon_0 A}\int\exp\left[i\left(\mathbf{k}_f-\mathbf{k}_i\right)\cdot\mathbf{R}_0\right]\sum_n a_n^*\left[\phi^*_{n_1}\left(\mathbf{R}_1\right)\phi^*_{n_2}\left(\mathbf{R}_2\right)\pm\phi^*_{n_1}\left(\mathbf{R}_2\right)\phi^*_{n_2}\left(\mathbf{R}_1\right)\right]\times\\&\left[\int\frac{e^{-\mathbf{Q}'\cdot(\mathbf{R}_1-\mathbf{R}_0)}}{\kappa^2+Q'^2}+\frac{e^{-\mathbf{Q}'\cdot(\mathbf{R}_2-\mathbf{R}_0)}}{\kappa^2+Q'^2}d\mathbf{Q}'\right]\times\\&\sum_m a_m\left[\phi_{m_1}\left(\mathbf{R}_1\right)\phi_{m_2}\left(\mathbf{R}_2\right)\pm\phi_{m_1}\left(\mathbf{R}_2\right)\phi_{m_2}\left(\mathbf{R}_1\right)\right]d\mathbf{R}_0 d\mathbf{R}_1 d\mathbf{R}_2,\end{aligned} \tag{4.20}$$

where the + sign refers to total spin 0 and the − sign refers to spin 1. The two dimensional variables $\mathbf{k}_i$ and $\mathbf{k}_f$ are the initial and final wave vectors of the WL electron whereas $\mathbf{Q}'$ is merely a three dimensional dummy variable used in the Fourier transform of the Yukawa potential. This distinction is important since the wetting layer is located a distance z_0 below the origin and we must take this into account when performing the $\mathbf{R}_0$ integral which has the general form:

$$\exp\left(i\mathbf{Q}'\cdot\mathbf{R}_n\right)\int\exp\left(i\left(\mathbf{k}_f-\mathbf{k}_i\right)\cdot\mathbf{r}_0-i\mathbf{Q}'\cdot\mathbf{R}_0\right)d\mathbf{R}_0$$
$$=4\pi^2\exp\left(i\mathbf{Q}'\cdot\mathbf{R}_n\right)\exp\left(-iQ'_\perp z_0\right)\delta\left[\left(\mathbf{k}_f-\mathbf{k}_i\right)-\mathbf{Q}'_\parallel\right]. \tag{4.21}$$

The subscript n takes the value 1 or 2 corresponding to one of the two integrals over $\mathbf{R}_1$ or $\mathbf{R}_2$ in Eq. 4.20. Substituting the result of Eq. 4.21 into expression 4.20 we immediately perform the integral over $\mathbf{Q}'_\parallel$ to remove the delta function. This gives the matrix element as:

$$\frac{e^2}{4\pi\epsilon\epsilon_0 A}\int\frac{\exp\left(-iQ'_\perp z_0\right)}{\kappa^2+\left(\mathbf{k}_f-\mathbf{k}_i\right)^2+Q_\perp^2}\left\{\exp\left[i\left(\mathbf{k}_f-\mathbf{k}_i+\mathbf{Q}'_\perp\right)\cdot\mathbf{R}_1\right]+\right.$$
$$\left.\exp\left[i\left(\mathbf{k}_f-\mathbf{k}_i+\mathbf{Q}'_\perp\right)\cdot\mathbf{R}_2\right]\right\}\sum_{nm}a_n^*b_m\left[\phi_{n_1}^*\left(\mathbf{R}_1\right)\phi_{n_2}^*\left(\mathbf{R}_2\right)\phi_{m_1}\left(\mathbf{R}_1\right)\phi_{m_2}\left(\mathbf{R}_2\right)\pm\right.$$
$$\phi_{n_1}^*\left(\mathbf{R}_1\right)\phi_{n_2}^*\left(\mathbf{R}_2\right)\phi_{m_1}\left(\mathbf{R}_2\right)\phi_{m_2}\left(\mathbf{R}_1\right)\pm\phi_{n_1}^*\left(\mathbf{R}_2\right)\phi_{n_2}^*\left(\mathbf{R}_1\right)\phi_{m_1}\left(\mathbf{R}_1\right)\phi_{m_2}\left(\mathbf{R}_2\right)+$$
$$\left.\phi_{n_1}^*\left(\mathbf{R}_2\right)\phi_{n_2}^*\left(\mathbf{R}_1\right)\phi_{m_1}\left(\mathbf{R}_2\right)\phi_{m_2}\left(\mathbf{R}_1\right)\right]dQ_\perp d\mathbf{R}_1 d\mathbf{R}_2. \tag{4.22}$$

The integrals over $\mathbf{R}_1$ and $\mathbf{R}_2$ result in the expression $F_\pm(\mathbf{k}_f-\mathbf{k}_i+\mathbf{Q}'_\perp)$ as defined by Eq. 4.15. Substituting expression 4.22 into the Golden Rule (Eq. 3.2) we have the relaxation rate as:

$$\frac{e^4 n_2}{8\pi^4\epsilon^2\epsilon_0^2 k_B T\hbar}\int\left|\int\frac{\exp\left(-iQ'_\perp z_0\right)}{\left[\kappa^2+\left(\mathbf{k}_f-\mathbf{k}_i\right)^2+Q'^2_\perp\right]}F_\pm\left(\mathbf{k}_f-\mathbf{k}_i+\mathbf{Q}'_\perp\right)dQ'_\perp\right|^2\times$$
$$\exp\left(-\alpha k_i^2\right)\delta\left(k_f^2-k_i^2-\beta^2\right)d\mathbf{k}_i d\mathbf{k}_f \tag{4.23}$$

where α and β are defined in Eq. 4.17

We now make the coordinate transform $\mathbf{k}_f=\mathbf{q}+\mathbf{k}_i$. This allows the integral over θ_{k_i} to be performed in the same way as Eq. 3.10 which will affect the lower limit on the $\mathbf{k}_i$ integral in the same way as Eq. 3.22. The k_i integral is then given by Eq. 3.11 which gives the two particle, Auger relaxation rate for electrons in the quantum dot scattering with electrons located in the wetting layer as:

$$\frac{e^4 n_2 m_{QD}^*}{16\pi^4\epsilon^2\epsilon_0^2\hbar^2 m_{WL}^*}\sqrt{\frac{2\pi m_{WL}^*}{k_B T}}\int|\mathbf{q}|^{-1}\exp\left[-\alpha\left(\frac{q^2-\beta^2}{2|\mathbf{q}|}\right)^2\right]\times$$

$$\left| \int \left[\kappa^2 + q^2 + Q_\perp'^2\right]^{-1} \exp\left(-iQ'_\perp z_0\right) F_\pm\left(\mathbf{q} + \mathbf{Q}'_\perp\right) dQ'_\perp \right|^2 d\mathbf{q}, \tag{4.24}$$

where α and β are given by Eq. 4.17, m^*_{QD} and m^*_{WL} are the effective masses of the dot electron and the wetting layer electron respectively and $F_\pm(\mathbf{q} + \mathbf{Q}'_\perp)$ is given by Eq. 4.15. The equivalent single particle rate is given by expression 3.13 which is identical to expression 4.24 except that the factor $F(\mathbf{q} + \mathbf{Q}'_\perp)$ is given by $< \phi_f(\mathbf{r})| \exp[i(\mathbf{q} + \mathbf{Q}'_\perp] \cdot \mathbf{r})|\phi_i(\mathbf{r}) >$.

4.4 Results and Discussion

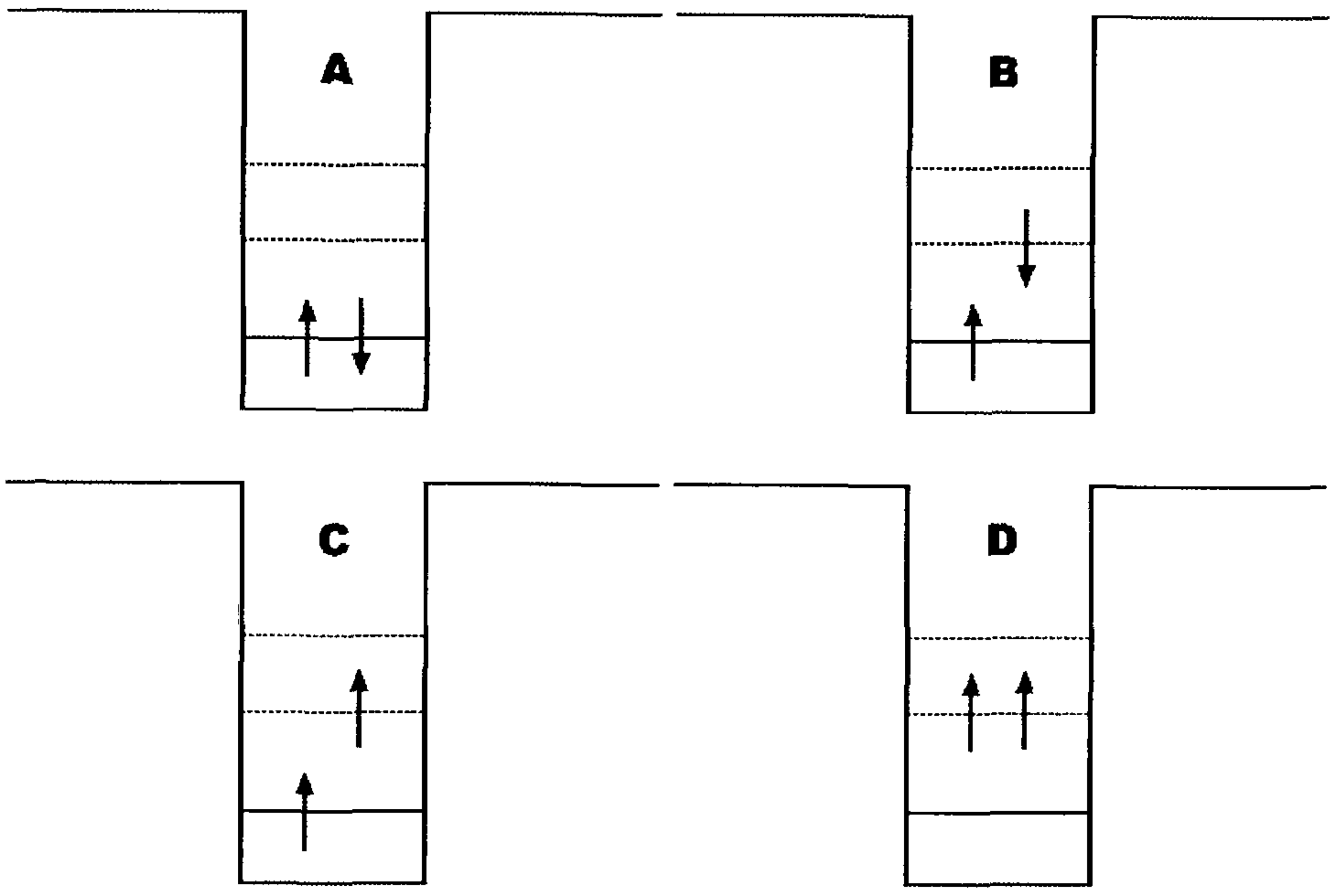

Figure 4.1: Schematic showing the configuration of spin 0 and spin 1 two particle states. Dotted lines denote degenerate levels. A) Spin 0 ground state, B) spin 0 first excited state, C) spin 1 ground state, D) spin 1 first excited state. State D is allowed since the two electrons occupy two distinct spatial quantum states.

For all of the models used in this chapter, the first excited energy level for single particles is two-fold degenerate. For the HO model this degeneracy arises due to the angular momentum ($l = \pm 1$) symmetry of the first excited energy level. In the case of the truncated pyramid models the degeneracy comes from the four-fold rotational symmetry of the dot. In both cases, we can construct the ground state of the two-electron system by placing both electrons in the lowest energy level. This picture is not strictly valid since the Coulomb interaction mixes the non-interacting states, but if the interaction is weak the schematic given in figure 4.1 will be acceptable. In this system, both electrons must have opposite spin, giving the total spin as zero. This state is shown in figure 4.1A.

The first excited state for the two electron system of total spin zero will occur when one of the electrons is placed in either of the two degenerate first excited energy levels and the other electron is placed in the lowest energy level. Relaxation between this excited state and the ground state described above is allowed since both states have a total spin of zero as shown in figures 4.1A-B. If we consider the situation where the two-electron system has total spin 1, then without the possibility of a spin flip (which we discuss in chapter 5) relaxation from this state to the spin 0 ground state will be blocked. This configuration must then be the ground state of total spin 1 and is shown in figure 4.1C.

If both electrons have the same spin and are each placed in one of the two degenerate energy levels described above, then we have the spin 1 excited state shown in figure 4.1D. Relaxation from this state can occur by an electron in either of the degenerate levels making the transition to the lowest energy level. In this way, the electronic states of the two-particle quantum dot can be thought of as somewhat analogous to para and ortho-helium.

We choose these particular states because in a non-interacting dot, the energy difference between the initial and final states is identical and for each value of total spin, the relaxing electron makes the same transition. The only difference is the location of the "spectator" electron, which will begin to influence the relaxation process and the energy levels once the Coulomb interaction is turned on.

	InAs (I)	InAs (N)	InGaAs (I)	InGaAs (N)
$S = 0$ GS	-497.55	-515.84	-428.97	-447.22
$S = 0$ ES	-421.28	-441.26	-357.66	-377.34
$S = 0$ ΔE	76.27	74.58	71.31	69.88
$S = 1$ GS	-429.62	-441.26	-365.71	-377.35
$S = 1$ ES	-354.48	-366.68	-295.37	-307.46
$S = 1$ ΔE	75.14	74.58	70.34	69.88

Table 4.1: Energy levels in meV for the InAs truncated pyramid dot and the InGaAs graded truncated pyramid dot for interacting (I) and non-interacting (N) spin 0 and spin 1 two particle states. Energies are relative to the GaAs conduction band edge where applicable.

When the Coulomb interaction between the two dot electrons is included, the energy difference of the levels becomes spin dependent. In Table 4.1 we present the energy of the ground state (GS), excited state (ES) and the energy difference (ΔE) for the states given schematically in figure 4.1. The interacting and non-interacting energy levels are compared for the pure InAs truncated pyramid and the graded $\mathrm{In}_x\mathrm{Ga}_{1-x}\mathrm{As}$ truncated pyramid models introduced in chapter 2.

From table 4.1, we find that the inclusion of the Coulomb interaction makes only a small difference to the energy gap (ΔE). For the pure InAs pyramid dot, the spin 1 energy gap increases by only 0.75% due to the inclusion of the unscreened Coulomb interaction whereas the spin 0 energy gap increases by

2.22%. For the InGaAs graded dot, the spin 1 energy gap increases by 0.65% and the spin 0 energy gap increases by 2.01%. The Coulomb interaction raises the energy of the ground and excited states by similar amounts so that the energy gap is only marginally affected.

4.4.1 The Effect of Screening on the Dot Wave Functions.

In calculating the two particle states described in section 4.2.2, the use of a Yukawa potential (Eq. 4.6) allows for the possibility of screening of the Coulomb interaction between the two electrons confined in the dot. The screening parameter κ that appears in the Coulomb matrix elements of Eq. 4.7 is dependent on the electron density of the surrounding material. Therefore, in order to calculate the relaxation rate as a function of injected electron density (see Eq. 3.1), the two particle states must be calculated individually for each point on the curve. However, each time we calculate the relaxation rate, approximately 98% of the computer time is taken to calculate the two particle states. This fact alone makes the calculation prohibitively time consuming.

Since calculating the two particle states is so computationally expensive, it would be ideal if we were able to calculate the states once and then use those states to calculate the relaxation rate over the entire range of carrier densities. To do this we would have to either neglect screening between the two dot electrons or fix it at some arbitrary value. If the surrounding electron density is high and screening is strong, the two-particle dot will be approximately non-interacting. For non-interacting systems, the spectator electron can be expected to play no part in the relaxation mechanism other than to block transitions to the occupied state. In this case, the process will be similar to the single particle case discussed in chapter 3. At the other end of the scale where electron density is low, screening can be safely neglected. We might expect that the relaxation rate will vary smoothly between the highly screened and unscreened limits and we may simplify the calculations by considering only the unscreened limit in the majority of results. To explore this possibility, we present a comparison between the relaxation rates calculated using screened and unscreened InAs truncated pyramid quantum dot wave functions.

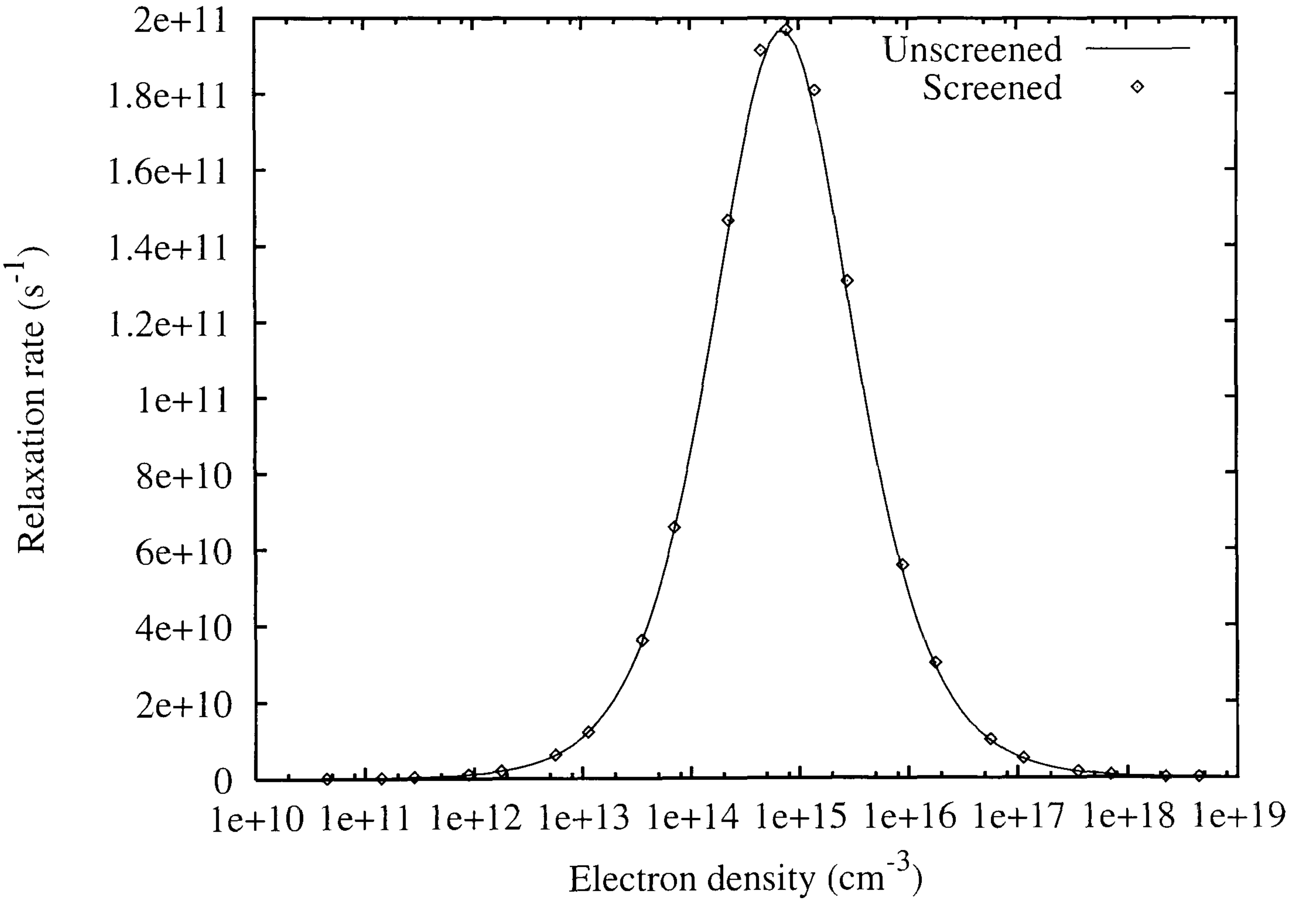

Figure 4.2: Relaxation rate against bulk electron density. The points denote calculations where the interaction between the two dot electrons is screened by the surrounding bulk electron density. The line denotes unscreened wave functions. See section 4.2.2.

Figure 4.2 shows the relaxation rate against bulk carrier density calculated with unscreened (line) and screened (dots) wave functions. At low electron densities the relaxation rate calculated with screened wave functions is smaller than the relaxation rate with unscreened wave functions by approximately 0.6%, a value which saturates below electron densities of $\approx 10^{13}$cm^{-3}. At electron densities greater than $\approx 10^{16}$cm^{-3}, the difference saturates again with the relaxation rate calculated using unscreened wave functions being smaller by approximately 3.3%. Figure 4.3 shows the percentage difference between relaxation rates using screened and unscreened wave functions (denoted by dots) and the screening length (κ^{-1} (line), see Eq. 3.3) as a function of bulk electron density.

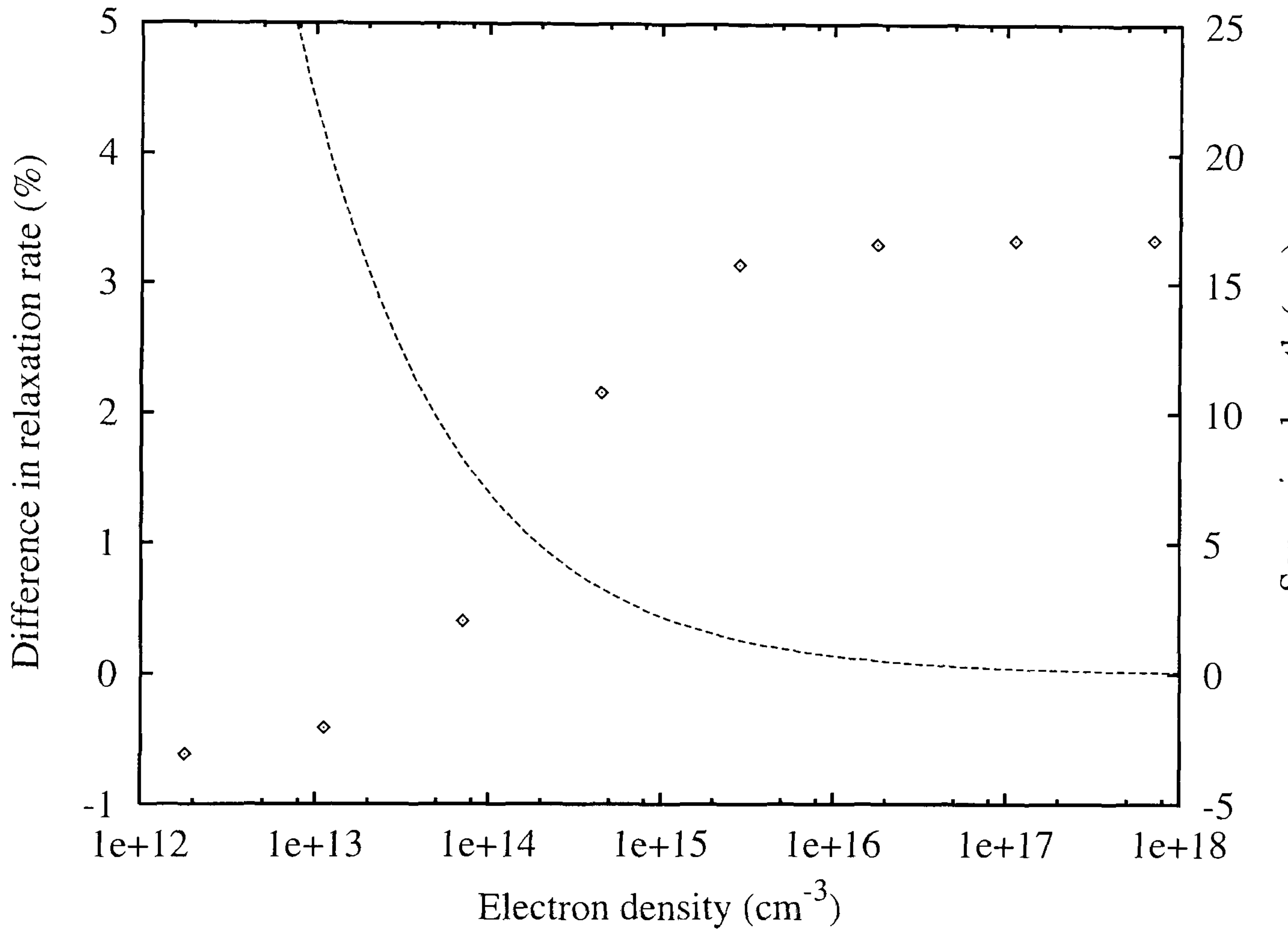

Figure 4.3: Points denote the percentage difference between the relaxation rate calculated using screened and unscreened wave function as a function of bulk electron density for dot electrons scattering with electrons in the bulk. The line denotes screening length as a function of bulk electron density. Calculated for the InAs truncated pyramid dot at $T = 1$K.

When the screening length is much larger than the size of the quantum dot (18nm in this case), the interaction between the dot electrons can be neglected.

As the screening length becomes comparable to the size of the quantum dot, the interaction becomes more important. However, for this system the difference between the relaxation rates calculated with screened and unscreened wave functions still saturates at only 3.3%. The relatively small effect screening has on the relaxation rate suggests that the dot electrons can be considered to be only weakly interacting and that the effect of screening the two dot electrons from each other can be neglected with only a small loss of accuracy.

4.4.2 Two Dimensional Auger Relaxation

We first consider relaxation between the total spin 0 states as shown schematically in figures 4.1A-B. The excited electron (figure 4.1B) relaxes by scattering with carriers confined in the wetting layer. The method used to calculate this relaxation rate is given in section 4.3.2 and is similar to that of section 3.2 for Auger relaxation in single particle dots.

Figure 4.4 shows the relaxation rate against wetting layer electron density for several different dot models. We consider the two self-assembled quantum dot models of truncated pyramid shape introduced in chapter 2. The first is pure InAs and the second is $In_xGa_{1-x}As$ where x varies linearly from 0.6 at the bottom and 1 at the top. In addition to the truncated pyramid models, we include two HO models (expression 2.4) where parameters have been fitted to the InAs truncated pyramid models by the energy gap and the root mean square (RMS) deviation ($\sqrt{< r^2 > - < r >^2}$) methods described in section 3.5.4.

The graded material model gives rise to a slightly lower relaxation rate than the pure InAs model. This is due to the material gradient confining the electrons slightly higher in the dot and further away from the wetting layer as discussed in

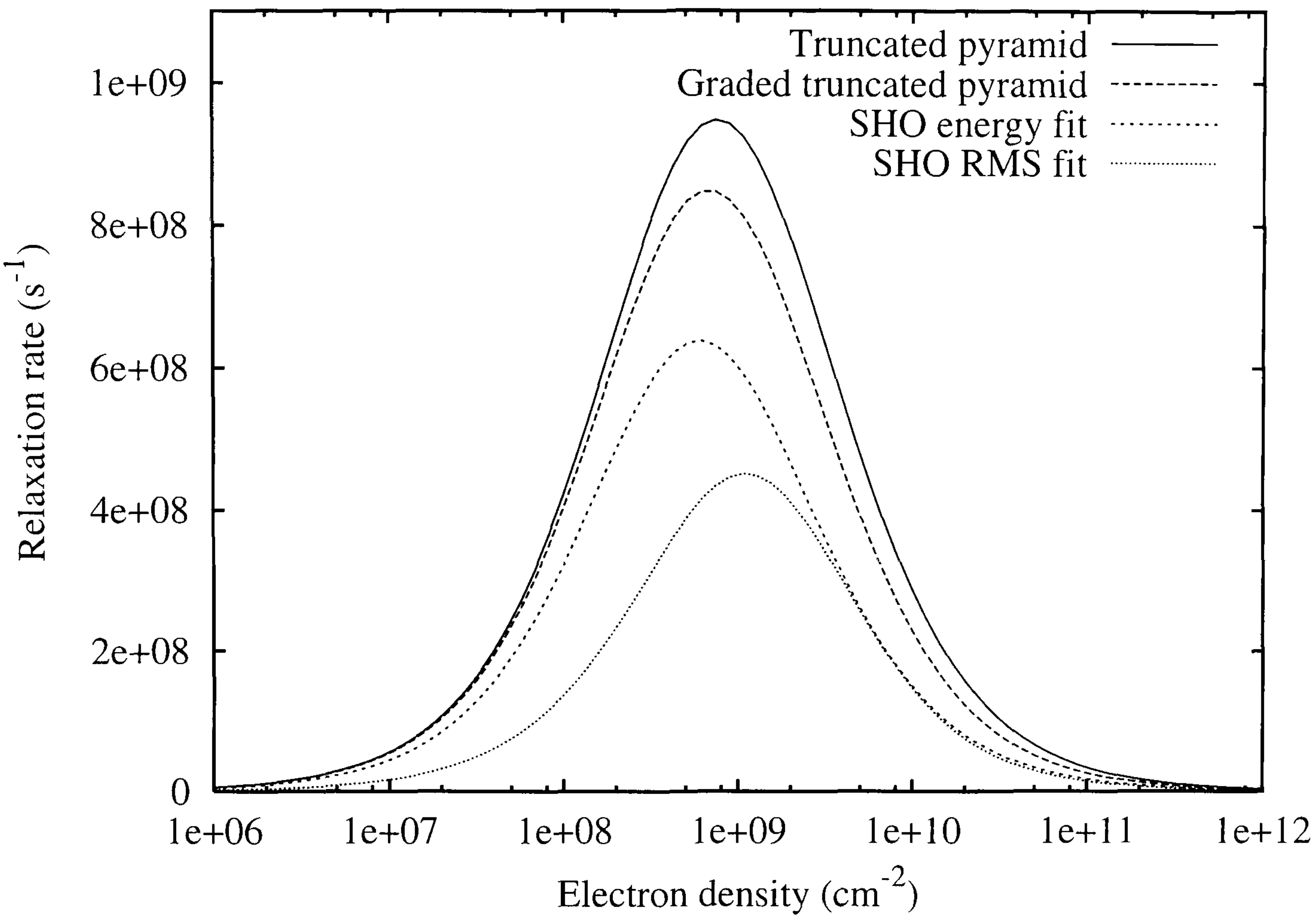

Figure 4.4: Total spin 0 relaxation, QD electrons scatter with WL electrons at a temperature of 1K. Solid line denotes the InAs truncated pyramid model, the coarse dotted line is the $In_xGa_{1-x}As$ graded truncated pyramid, the fine dotted line is the HO model with parameters fitted to the energy gap and ground state energy, and the chained line is the HO model with parameters fitted to the RMS deviation.

section 3.5.4.

Figure 4.5 shows total spin 1 relaxation between the two states shown schematically in figures 4.1C-D. The suppression of the relaxation rate in the case of the graded truncated pyramid model is again present. Once more this can be attributed to the composition gradient confining the electrons slightly further away from the wetting layer than in the pure InAs dot.

Comparing the results presented in figures 4.4 and 4.5, we find that the spin 0 and spin 1 relaxation rates for the GaAs truncated pyramid dot differ by a factor

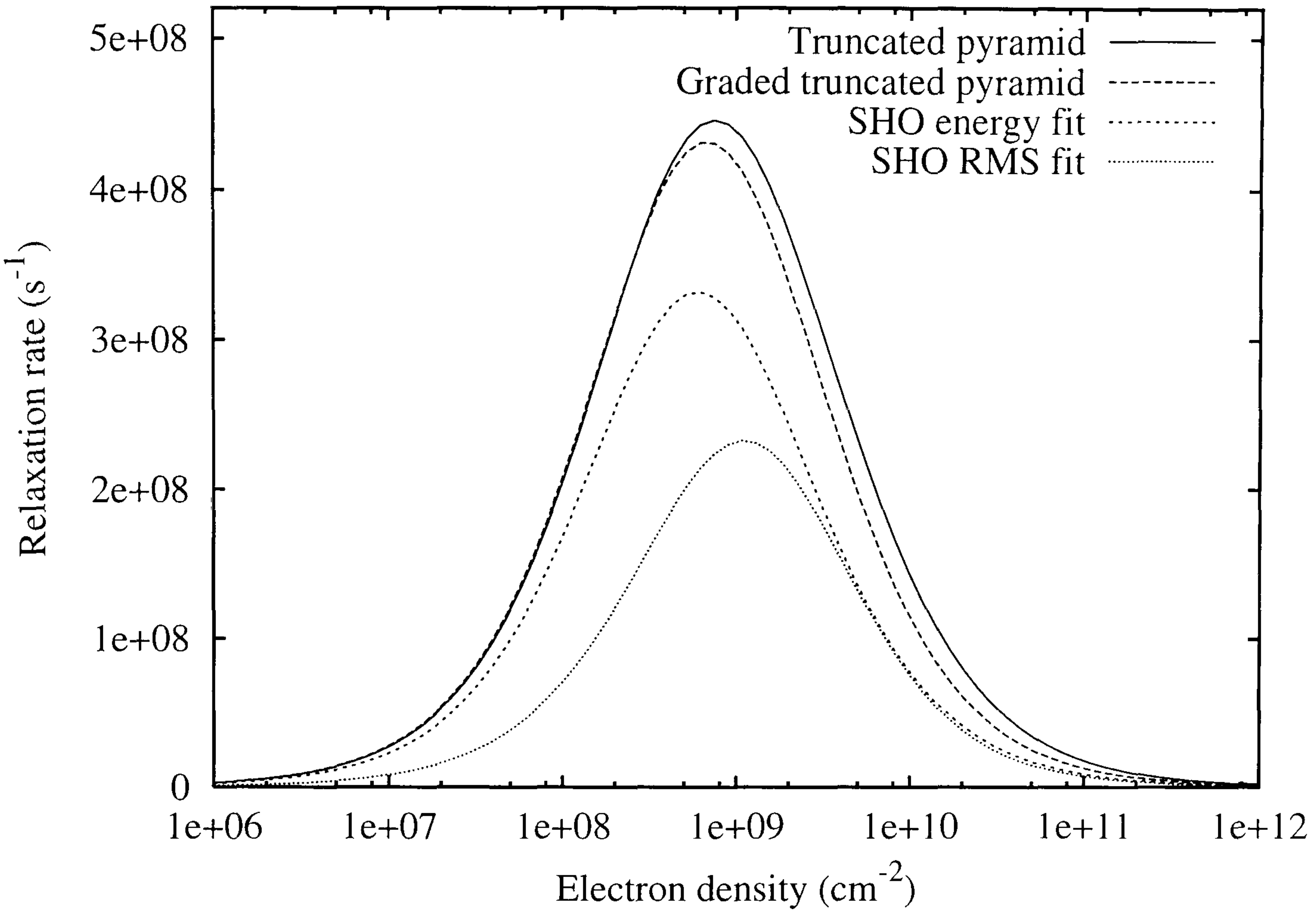

Figure 4.5: Total spin 1 relaxation, QD electrons scatter with WL electrons at a temperature of 1K for an injected carrier density of $n_p = 10^{12} - 10^{18}\mathrm{cm}^{-3}$. Solid line denotes the InAs truncated pyramid model, the coarse dotted line is the $\mathrm{In}_x\mathrm{Ga}_{1-x}\mathrm{As}$ graded truncated pyramid, the fine dotted line is the HO model with parameters fitted to the energy gap and ground state energy, and the chained line is the HO model with parameters fitted to the RMS deviation.

of 2.07. The spin 0 and spin 1 rates for the InGaAs graded truncated pyramid model differs by a factor of 1.97. A similar comparison for the RMS and energy fit HO models shows a difference of 1.94 and 1.92 respectively. This factor of approximately 2 can be explained by considering the matrix element for a non-interacting two particle quantum dot. The factor $F_{\pm}(\mathbf{q})$ given by Eq. 4.15 for non-interacting particles reduces to:

$$\begin{aligned}&\delta_{2n,2m}\left\langle\phi_{1n}(\mathbf{r})\left|e^{i\mathbf{q}\cdot\mathbf{r}}\right|\phi_{1m}(\mathbf{r})\right\rangle+\delta_{1n,1m}\left\langle\phi_{2n}(\mathbf{r})\left|e^{i\mathbf{q}\cdot\mathbf{r}}\right|\phi_{2m}(\mathbf{r})\right\rangle\pm\\&\delta_{1n,2m}\left\langle\phi_{2n}(\mathbf{r})\left|e^{i\mathbf{q}\cdot\mathbf{r}}\right|\phi_{1m}(\mathbf{r})\right\rangle\pm\delta_{2n,1m}\left\langle\phi_{2n}(\mathbf{r})\left|e^{i\mathbf{q}\cdot\mathbf{r}}\right|\phi_{1m}(\mathbf{r})\right\rangle,\end{aligned}\qquad(4.25)$$

where the + sign corresponds to the spin 0 and the − sign corresponds to the spin 1 matrix elements. For the spin 0 case, the + sign applies and we consider relaxation between the ground and first excited states shown schematically in figures 4.1A-B. Relaxation between states of total spin 0 in a non-interacting dot gives $\phi_{n_1} = \phi_{n_2} = \phi_{m_2} = \phi_0$ and $\phi_{m_1} = \phi_1$. The double occupancy of the $\phi_{n_2} = \phi_{m_2} = \phi_0$ state requires an additional normalisation factor of $1/\sqrt{2}$. When these states are substituted into 4.25, we find the expression simplifies to $\frac{1}{\sqrt{2}}[< \phi_0|e^{i\mathbf{q}\cdot\mathbf{r}}|\phi_1 > + < \phi_0|e^{i\mathbf{q}\cdot\mathbf{r}}|\phi_1 >] = \sqrt{2} < \phi_0|e^{i\mathbf{q}\cdot\mathbf{r}}|\phi_1 >$.

If we consider the spin 1 case we have $\phi_{n_2} = \phi_{m_2} = \phi_2$, $\phi_{n_1} = \phi_0$ and $\phi_{m_1} = \phi_1$, and expression 4.25 simplifies to the single term: $< \phi_0|e^{i\mathbf{q}\cdot\mathbf{r}}|\phi_1 >$. Comparing these two results, we find that the double occupancy of the spin 0 ground state gives two terms in the matrix element that do not vanish due to the Kronecker delta selection rules instead of one. The extra normalisation constant that also arises because of the double occupancy results in the factor of $\sqrt{2}$ in the matrix element. This can be thought of as a consequence of the two possible spin orientations and the Pauli exclusion principle. The Coulomb interaction introduces a small mixing of other states that subsequently appear in the matrix element. The slight deviation from the factor of 2 in the non-interacting case is a result of this mixing.

We now wish to compare the single particle rates calculated in chapter 3 with the two particle interacting rate. We consider the spin 1 system so that double occupancy of spatial states does not obscure the comparison. Figure 4.6 shows relaxation rates for the HO model with parameters fitted to the energy gap of the truncated pyramid model for both the two-particle rate (solid line) and the single particle rate (points). At the peak, the single particle rate is found to be

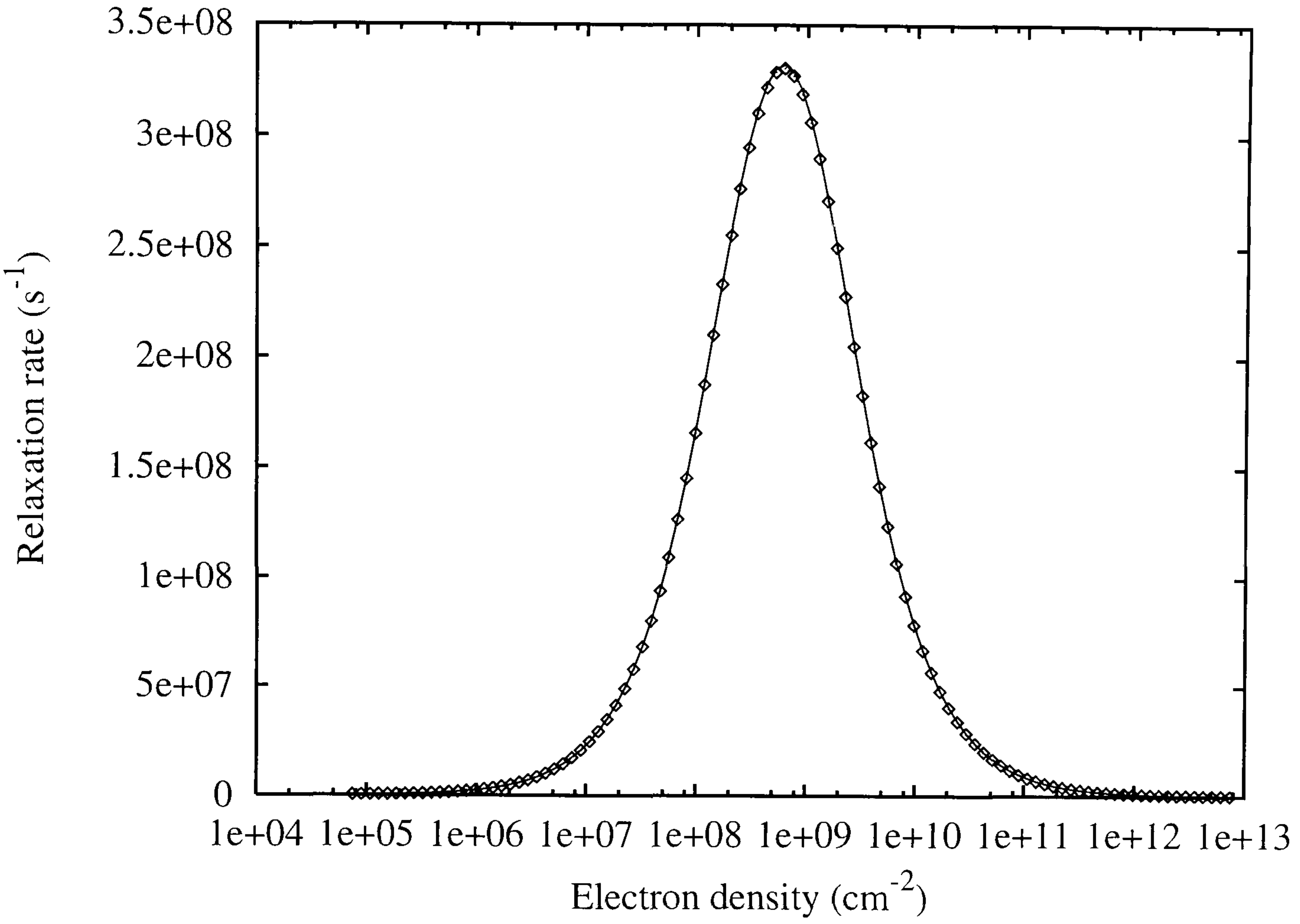

Figure 4.6: Relaxation rate against wetting layer electron density for the HO model with parameters fitted to the energy levels of the truncated pyramid dot. The solid line is the two-electron rate and the points correspond to the single electron rate from figure 3.5. The difference at the peak between these two plots is $\approx 0.5\%$.

$\approx 0.5\%$ lower than the two particle rate. Comparing the single and two particle rates for parameters fitted to the RMS deviation, we find that the peak single particle rates is $\approx 0.39\%$ lower than the two particle rate.

The difference between the single and two particle relaxation rates might be explained by considering the contribution to the total energy by the Coulomb matrix elements. For the HO model, the energy of the two independent particles (E_0) goes like λ^{-2} (see Eqs. 2.2 and 2.5) whereas the Coulomb energy (E_c) can be shown to go like λ^{-1}. So a larger dot might be expected to show a more pronounced effect from the Coulomb interaction. A comparison of the Coulomb

	RMS fit	Energy fit
λ (nm)	4.47	6.67
E_0 (meV)	509.56	231.55
E_c (meV)	12.04	7.81
E_c/E_0 (%)	2.36	3.38
$\Delta E_{\kappa=\infty}$ (meV)	165.84	74.58
$\Delta E_{\kappa=0}$ (meV)	165.96	74.67

Table 4.2: Ground state energies (E_0), Coulomb energies (E_c) and their ratio for various HO quantum dot models. The ΔE's are the differences between first excited state and ground state for the non-interacting and interacting states.

energies for ground state interactions for the two HO models considered here is given in table 4.2. A small decrease in the size of the quantum dot length parameter (λ) is seen to produce a large increase in the non-interacting ground state energy E_0 but by comparison only a relatively small increase in the Coulomb energy E_c.

The small size of the self-assembled dot means that the two-electron system is relatively weakly interacting. Because of this, the energy difference between ground and first excited state does not change significantly with the inclusion of the Coulomb interaction. In the energy fit HO model for example, the non-interacting energy difference is 74.58meV increasing by only 0.12% to 74.67meV in the interacting dot. In the SAQD models the Coulomb interaction has only a slightly more noticeable effect. Table 4.1 shows the energy levels for the two

SAQD models considered here. For the pure InAs model the energy gap increases by 0.74% from 74.58meV to 75.14meV. For the graded model, the increase is by 0.65% from 69.88meV to 70.34meV. Since the relaxation rate only has an energy difference dependence in β (Eq. 4.17) and the mixing of the basis states is relatively small, the inclusion of the Coulomb interaction has only a marginal effect on the relaxation rate.

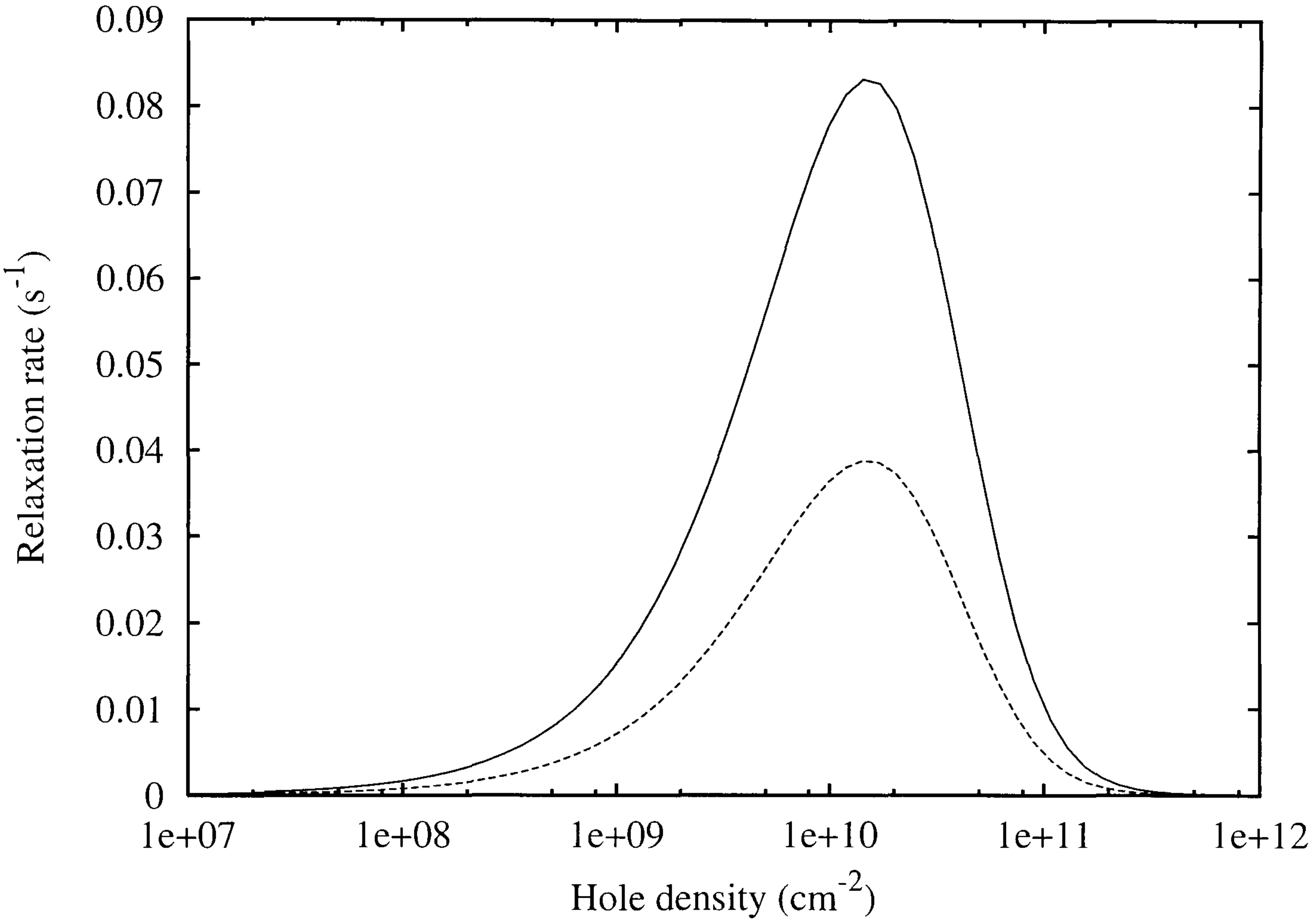

Figure 4.7: 2D Relaxation rate for heavy holes in the HO model with parameters fitted to the energy levels of the graded truncated pyramid model. The top (solid) line denotes spin 0, and the bottom (dotted) line denotes spin 1. Calculations are performed at a temperature of 1K.

For completeness sake we include relaxation rates calculated for heavy holes in the dot scattering with holes in the wetting layer. Figure 4.7 shows the spin 0 (solid line) and spin 1 (dotted line) relaxation rates for the HO model, calculated using parameters fitted to the heavy hole energy gap in the graded truncated pyramid model. The heavy hole well depth in the graded truncated pyramid model varies approximately linearly from $\approx$ 100 to 400meV relative to the valence band edge. In order to calculate the length parameters we have taken an average depth of 250meV with a ground state energy of 174meV and a first excited state energy of 134meV again relative to the valence band edge. This gives length parameters for heavy holes as $\lambda = 2.16$nm and $\lambda_z = 0.83$nm.

The λ_z length parameter corresponds to an extremely tight confinement in the z direction. The vertical component of the dot wave function is a Gaussian that decays rapidly with such a small length parameter. As a result of this fast decay, the overlap between dot and wetting layer wave functions at z_0 is negligible and the relaxation rate for heavy holes scattering with holes in the wetting layer is strongly suppressed. The two relaxation rates differ by a factor of approximately 2.14.

However, it must be stressed that the results for hole scattering presented here depend strongly on the parameters of the dot system. In order to fit the λ_z length parameter used in the HO model, we have matched the energy difference between the bottom of the potential well and the ground state; to the vertical confinement energy ($\hbar\omega_z$) for the truncated pyramid model calculated by Roy *et al.* [48]. Since the WL scattering rate depends critically on the overlap between the vertical part of the dot wave function and the two dimensional WL states at the point z_0, the correct choice of length parameter λ_z is crucial and will depend on the type of dot under investigation. This work is not intended to form a complete discussion of the hole relaxation processes in quantum dots and we include these limited results for comparison only.

4.4.3 Three Dimensional Auger Relaxation

In this section we consider dot electrons scattering with electrons in the surrounding bulk material and neglect the presence of the wetting layer as we did in section 3.3. First, we consider scattering between states of total spin 0 shown schematically in figure 4.1A-B. We then consider scattering between states of total spin 1 shown in figure 4.1C-D. In order to make the calculations tractable, we must again neglect the screening of dot wave functions by the surrounding electron density.

Figure 4.8 shows the relaxation rate for the two-electron system with total spin 0 calculated using the method given in section 4.3.1. We have considered the same dot models used in section 4.4.2. These are the two self-assembled quantum dot models of truncated pyramid shape, one of which is pure InAs and the other is $\mathrm{In}_x\mathrm{Ga}_{1-x}\mathrm{As}$ where x varies between 0.6 and 1 from bottom to top; and the two HO models with parameters fitted to the energy gap and the RMS deviation of the truncated pyramid dot.

The material gradient of the truncated pyramid dot in figure 4.8 affects the bulk relaxation rate only slightly. This effect may be caused by the small change in the effective mass due to the inclusion of Gallium into the dot composition. This effect is discussed in section 3.5.4.

Figure 4.9 shows relaxation between states of total spin 1 shown schematically in figure 4.1C-D. We consider the same self-assembled and HO models as used in section 4.4.2. Comparing the relaxation rates given in figures 4.8 and 4.9 we find that the spin 0 and spin 1 relaxation rates for the GaAs truncated pyramid dot differ by a factor of 1.92. We also find that the spin 0 and spin 1 relaxation rates for the InGaAs graded truncated pyramid model differs by a factor of 1.93,

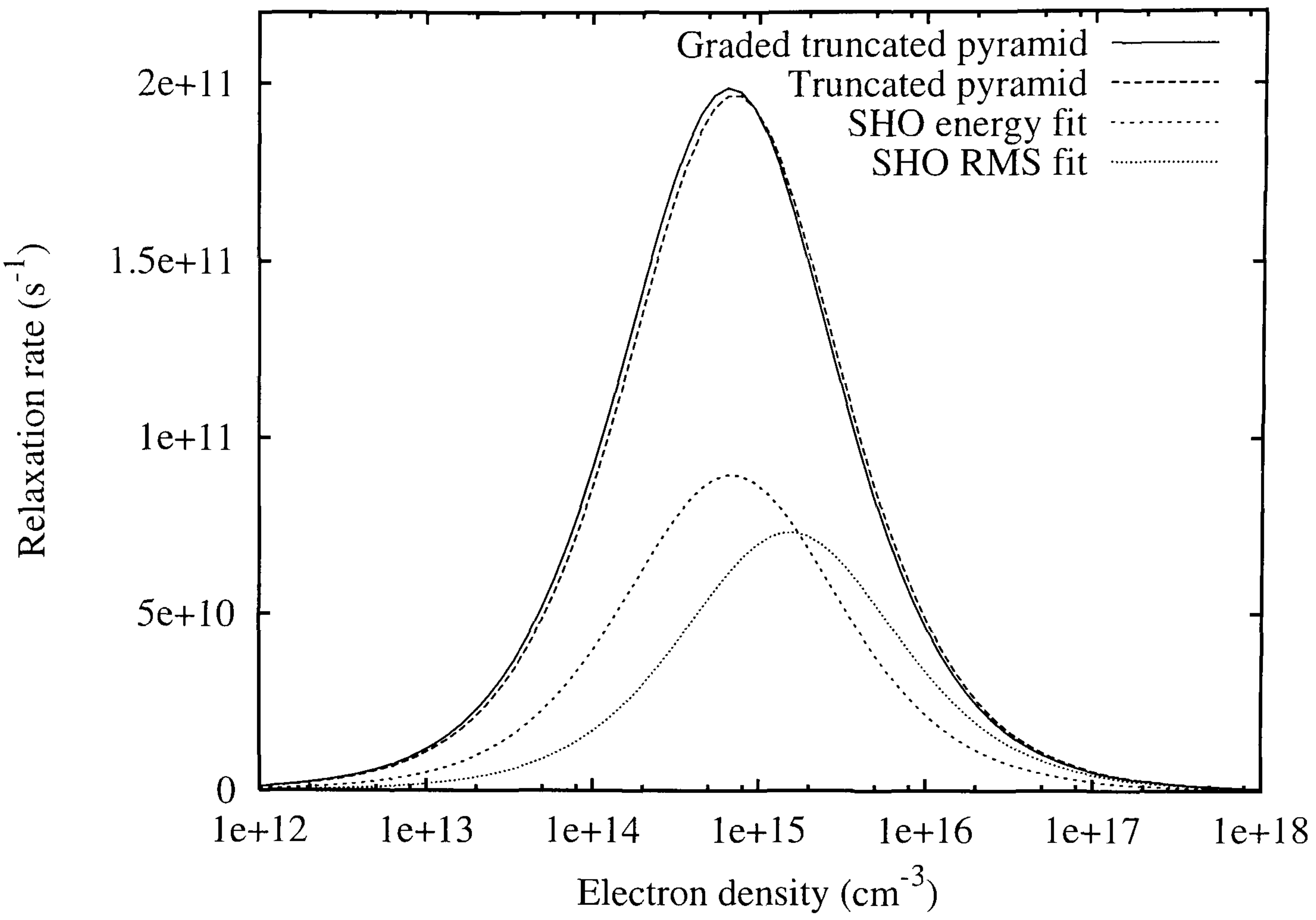

Figure 4.8: Total spin 0 relaxation, QD electrons scatter with electrons located in the surrounding bulk material. Calculated at a temperature of 1K with an injected carrier density of $n_p = 10^{12} - 10^{18}\text{cm}^{-3}$. The solid line denotes the truncated pyramid model, the coarse dotted line is the graded truncated pyramid, the fine dotted gives line HO model with parameters fitted to the ground and first excited state energy, and chained line is the HO model with parameters fitted to the RMS deviation.

and the RMS and energy fit HO models differ by 1.91 and 1.88 respectively. This factor of approximately 2 is discussed in section 4.4.2.

Figure 4.10 shows the two electron rate (solid line) compared to the single electron rate (points) originally presented in figure 3.6. The inclusion of the Coulomb interaction reduces the two-particle relaxation rate from the single particle rate by only 1.3% at the peak. This again can be contributed to the Coulomb interaction having only a marginal effect on the energy difference

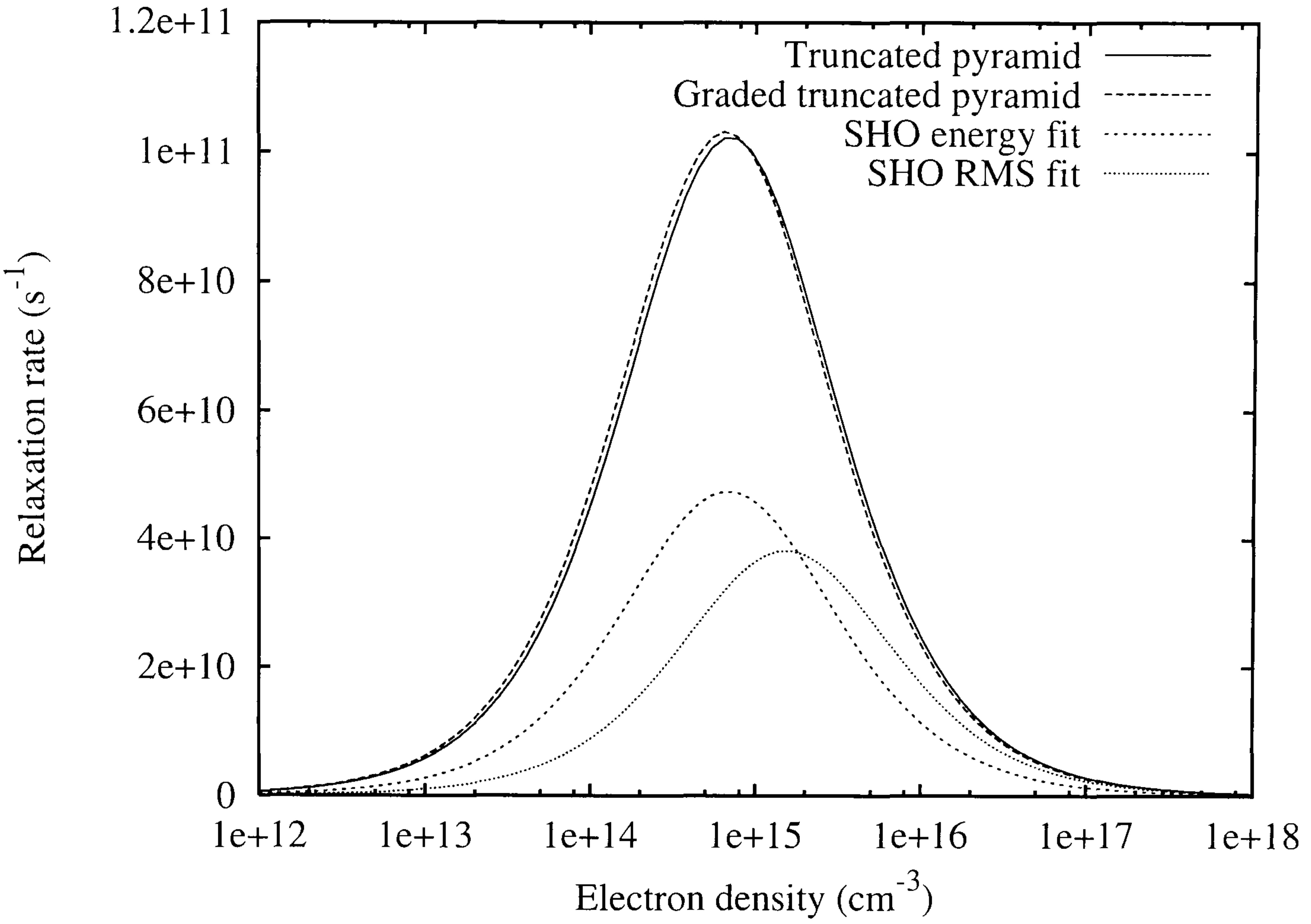

Figure 4.9: Total spin 1 relaxation, QD electrons scatter with electrons located in the surrounding bulk material. Calculated at a temperature of 1K with an injected carrier density of $n_p = 10^{12} - 10^{18}\text{cm}^{-3}$. The solid line denotes the truncated pyramid model, the coarse dotted line is the graded truncated pyramid, the fine dotted gives line HO model with parameters fitted to the ground and first excited state energy, and chained line is the HO model with parameters fitted to the RMS deviation.

between initial and final quantum states.

Figure 4.11 shows relaxation for heavy holes confined in the dot scattering with holes located in the surrounding bulk. The solid line denotes relaxation between states of total spin 0 (figure 4.1A-B) and the dotted line denotes relaxation between states of total spin 1. The two rates differ by a factor of 1.95 at the peak. The large effective mass of the heavy holes leads to a high confinement energy. This high confinement has the effect of reducing the rate at low electron

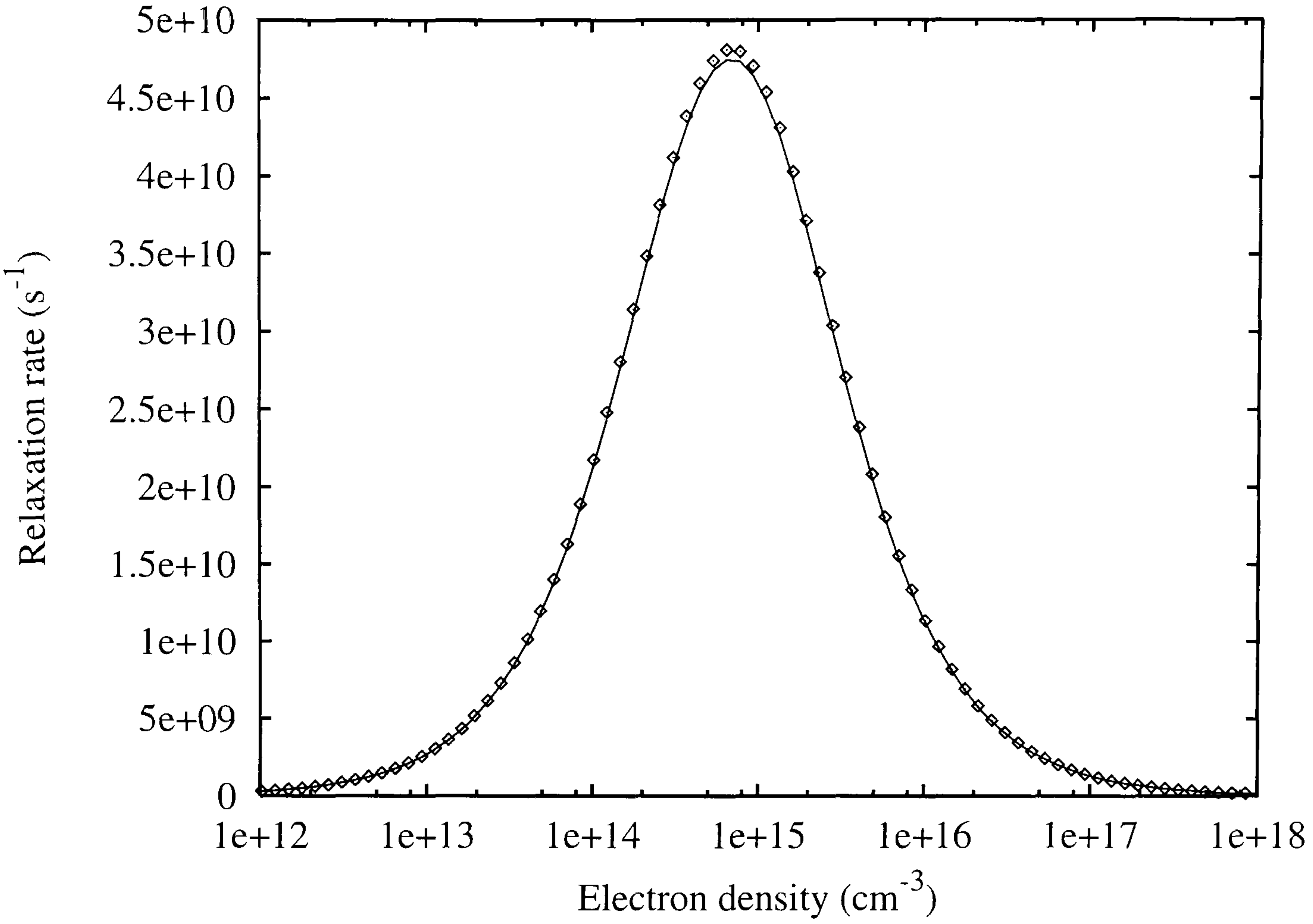

Figure 4.10: Bulk relaxation mechanism for HO energy fit model against electron density. The solid line denotes the two-electron rate and the points denote the single electron rate from figure 3.6. The difference between these two plots at the peak is $\approx 1.3\%$

densities, shifting the peak towards the higher electron density. The effect of confinement energy has been discussed in section 3.5.4.

4.5 Conclusions

In this chapter we have considered Auger relaxation processes in quantum dots containing two electrons. The two particle interacting states have been calculated by the exact diagonalisation of the Hamiltonian matrix with a basis set truncated by means of a convergence test. In the HO model, the Coulomb interaction energy is generally proportional to λ^{-1} which is a measure of the size of the quantum dot whereas the individual particle energy is proportional to λ^{-2}. Hence, the

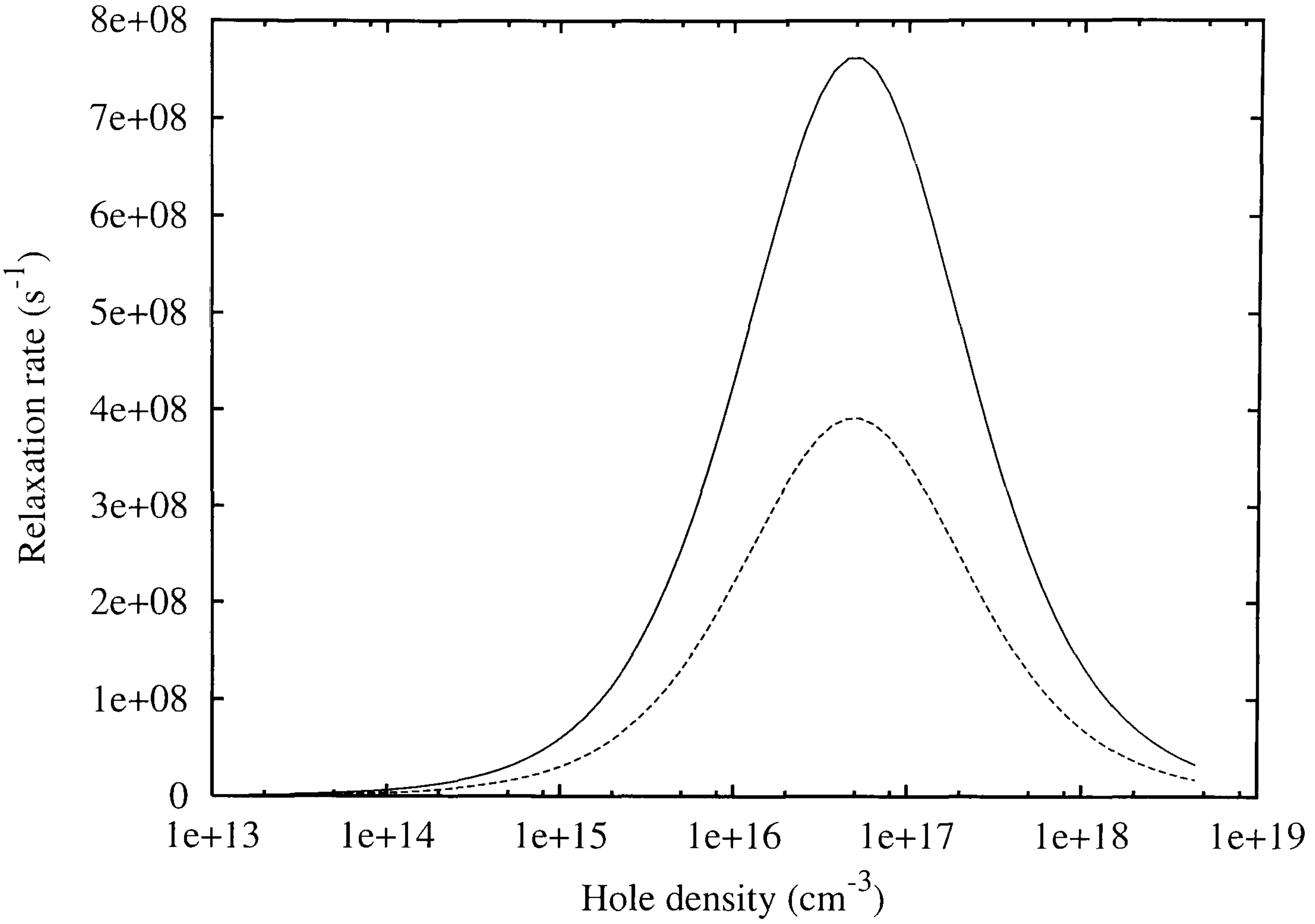

Figure 4.11: 3D Relaxation rate for heavy holes in the HO model with parameters fitted to the energy levels of the graded truncated pyramid model. Calculated at a temperature of 1K with an injected hole density of $n_p = 10^{10} - 10^{18}\text{cm}^{-3}$. Top (solid) line denotes spin 0 relaxation whereas the bottom (dotted) line denotes spin 1.

relative effect of the Coulomb interaction between dot electrons is size dependent and to a reasonable approximation, sufficiently small self-assembled dots can be considered only weakly interacting. The length parameters used in the HO states have no real counterpart in the other SAQD models so the argument presented above is not completely general. However, we expect that the main conclusions will remain valid.

The electron relaxation rate is only slightly influenced by the Coulomb interaction due to the effect it has on the matrix element and the change in the energy difference between initial and final states. The absolute energy of the states themselves does not affect the relaxation rate. Since the ground and excited state energy levels are affected similarly by the coulomb interaction for sufficiently small dots, the energy difference remains almost constant and the relaxation rate is virtually unaffected. The small mixing of the basis states introduced by the inclusion of the Coulomb interaction is the cause of this minor change in the energy of the levels. The state mixing also affects the relaxation rate directly through the dot wave functions used in the matrix element. The relaxation rate for the interacting system is dependent on both the effect the modified dot wave functions have on the matrix element and the change in the energy gap although both effects would seem to be weak in the systems considered in this work.

The Pauli exclusion principle has a strong effect on the relaxation rate in two particle dots. Double occupancy of the total spin zero spatial states causes a factor of 2 to be included in the non-interacting relaxation rate. This factor is modified slightly by the Coulomb interaction that causes a mixing of the quantum states.

This chapter has been mainly concerned with transitions between low-lying energy levels in specific self-assembled quantum dot systems. In these systems the energy gaps are generally much larger than the typical Coulomb energy between the dot electrons. As such, many of the conclusions drawn cannot be considered generally applicable since the relative magnitude of the Coulomb energy is dependent on factors such as dot size, effective mass and the energy gap between electronic states. In the case of relaxation of heavy holes given in figures 4.7 and 4.11, the spacing between energy levels is smaller than for electrons and the Coulomb interaction might be expected to be stronger. This will have an effect on the two-particle interaction, although the limited work presented here does not provide enough information to make any general conclusions. However, relaxation of heavy holes in the dot by scattering with holes in the wetting layer is found to be strongly suppressed in the model we have considered. The 2D relaxation rate is governed by the wave function overlap between WL and SAQD and is parameter dependent. The large effective mass of heavy holes gives rise to strong spatial confinement of the wave function, reducing the overlap, causing a strong reduction the rate. Fast relaxation is found for scattering with holes located in the surrounding bulk although the peak value of the relaxation rate is shifted towards the higher hole density. Clearly, there is a need for further work to be performed in this area to fully understand this subtle effect.

Chapter 5

Spin Relaxation in Electrostatic Quantum Dots

In this chapter we consider phonon-assisted relaxation processes in two electron electrostatic quantum dots. This work is inspired by the potential applications of quantum dots in quantum computing technology [22, 23, 24] and particularly by the recent experimental work of T. Fujisawa *et al.* [19, 20, 21]. Fujisawa *et al.* measured energy relaxation processes with and without a spin flip in electrostatic quantum dots. For this type of dot (see also the review by L. P. Kouwenhoven *et al.* [18]) we will calculate the wave functions and the energy spectrum, exploring the effects of the Coulomb interaction between dot electrons and the effect of the spin-orbit interaction. In addition, we will calculate relaxation rates for two different electron-phonon coupling mechanisms. The first is due to the deformation potential arising from the band bending produced by the emitted phonon. The second is due to the piezoelectric potential caused by the polarisation effect due to the strain produced by an emitted phonon.

The chapter is organised as follows. In section 5.1 we provide a brief review of some of the previous work in this area before going on to describe the Hamiltonian of the system in section 5.2. We describe the formulation of the Dresselhaus spin-orbit interaction matrix elements in section 5.2.1. In section 5.2.2, we present the energy spectrum, including spin-orbit coupling effects, as a function of magnetic field. The effect the Dresselhaus spin-orbit mixing has on the energy spectrum is discussed in detail by considering a single particle system in section 5.2.3. The method used to calculate the spin relaxation rates is given in section 5.3 for both the deformation potential interaction (section 5.3.1) and the piezoelectric potential interaction (section 5.3.2). We consider the effect screening has on the piezoelectric relaxation rate in section 5.3.3. In section 5.4 we present our results for the deformation potential relaxation rates. We first consider the non-interacting two-particle system in section 5.4.1 in order to explain the emergence of oscillations in the relaxation rate due to the vertical finite well confinement. We then include the Dresselhaus spin-orbit term and consider transitions that involve a spin flip in section 5.4.2. In section 5.5 we consider the piezoelectric mechanism and compare the results to those given in the previous section and to experimental work. The total relaxation rate is given in section 5.6 and in section 5.7 we reconsider the previous work in this field in light of our findings. Finally in section 5.8 we give our conclusions.

5.1 Previous Work

To date several authors have considered spin flip processes in quantum dots. A. V. Khaetskii and Y. V. Nazarov [25, 26], have examined several different mechanisms that could be responsible for spin flip transitions. By comparing the relaxation rates for each of these mechanisms in turn, they concluded that the dominant spin-mixing mechanism is related to the inversion asymmetry of the crystal lattice. This results in an admixture of different spin states that removes spin as a good quantum number. We will discuss Khaetskii and Nazarov's calculations further in section 5.2.1.

Several spin-orbit coupling effects in quantum dots have been considered by M. Valin-Rodriguez *et al.* [63, 64, 65, 66]. These authors did not consider relaxation but did compare the two possible admixture mechanisms (known as the Dresselhaus and Rashba mechanisms) previously considered by Khaetskii *et al.* It was noted by Valin-Rodriguez *et al.* that the Rashba term can be unitarily transformed to have the same form as the Dresselhaus term and therefore only amounts to a redefinition of the coupling constant. They also report that the Rashba term provided negligible spin-orbit coupling for the systems they considered.

During the course of this work, S. Dickman and P. Hawrylak [67] and M. Florescu *et al.* [68] (two papers from the same group) published relaxation rate studies concerning both Rashba and Dresselhaus admixture mechanisms, finding that the Dresselhaus term is usually dominant. These authors used a highly restricted basis set that does not appear to give converged energy eigenvalues when calculating the two-particle states. This also restricts the mixing of the electronic states, which may affect the relaxation rate if the basis set is truncated prematurely. We will discuss this work further in section 5.2.3.

Spin flip relaxation processes in electrostatic quantum dots have been studied experimentally by T. Fujisawa *et al.* [19, 20, 21]. These authors measured a single electron relaxation time without a spin flip of $\approx$ 10ns and two electron relaxation with a spin flip of $\approx$ 200μs for a parabolic quantum dot with asymmetric confinement potentials of $\hbar\omega_x = 2.5$meV and $\hbar\omega_y = 5.5$meV. Due to experimental limitations, they were unable to resolve individual Zeeman energy levels [20]. The relaxation rates observed by Fujisawa *et al.* are found to be consistent with the rates calculated in this work. We will return to consider the work of Fujisawa *et al.* in section 5.5.

5.2 The Hamiltonian

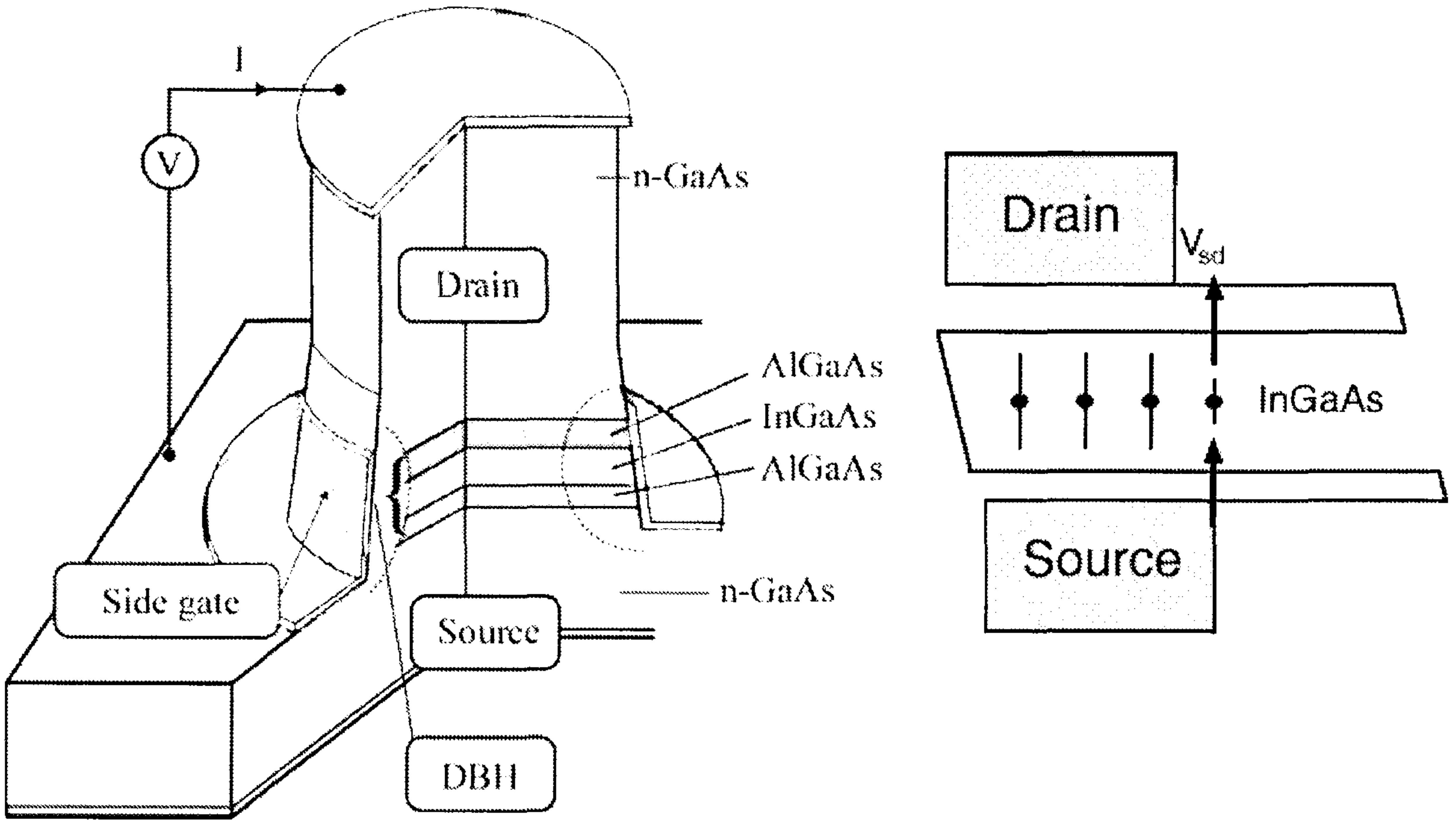

Figure 5.1: Left: an electrostatic pillar type quantum dot located between two AlGaAs barriers. A negative bias applied to the side gate provides the lateral confinement. Reproduced from [18]. Right: The corresponding energy diagram. Electrons tunnel from occupied states in the source, to an empty state in the drain via the quantum dot. The source-drain voltage V_{sd} determines the difference in the Fermi energies of the two electrodes.

We will consider electrostatic quantum dots similar to those used in the experimental work of Fujisawa *et al.* [19, 20, 21] and reviewed by L. P. Kouwenhoven *et al.* [18]. This type of dot is shown in figure 5.1. The quantum dot is located in the centre of the pillar between the two AlGaAs barrier layers. The potential barriers that separate the dot from source and drain contacts are such that tunnelling is weak and the number of electrons confined by the dot is well defined. The side gate has two functions. Firstly, it provides the lateral confinement and can be used to strengthen the potential effectively reducing the diameter of the dot. Secondly, by varying the side gate voltage an individual energy level can be aligned with the source and drain potential so that single electrons can tunnel into and out of the system. The electron number N can be varied widely over a range of side gate voltages. For example, when the confinement energy $\hbar\omega \approx 5$meV, $N = 1$, but if the gate voltage is increased by 0.43V corresponding to a confinement energy of $\hbar\omega \approx 4.25$meV, the electron number increases to $N = 6$ [18, 70].

For the purposes of mathematically representing the dot, we assume the system to be constructed from bottom to top as 3nm of n^+ doped GaAs, 0.5nm of GaAs, a 7nm AlGaAs tunnel barrier layer and the 12nm thick $In_{0.05}Ga_{0.95}As$ layer that forms the quantum dot itself. This is then covered with a 9nm AlGaAs tunnel barrier layer and finally 3nm of n^+ doped GaAs.

The lateral confinement potential of an electrostatic dot is known to be well approximated by a parabolic well [69]. In this work the parabolic confinement potential is taken to be $\hbar\omega = 5$meV which has been found [70] to be applicable to dots of the type used by Fujisawa *et al.* The wave functions for this type of parabolic dot are given by the Fock-Darwin states introduced in section 2.1 (see Eq. 2.1). The vertical confinement is a finite rectangular well. The dielectric constant has a position dependence due to the different materials in the heterostructure and the interactions between the dot electrons are screened by the dot contacts. The effect of this is two fold. First, the interaction does not have the usual r^{-1} dependence and second, the energy of each electron is shifted by the interaction with its own electrostatic image [70].

These effects are all taken into account when calculating the Coulomb integrals, which are found numerically by a subroutine provided by P. A. Maksym [70]. The routine calculates the electrostatic Green's functions given the approximation that the dot is much narrower than the pillar. This is expected to be valid since the lateral length parameter of the dot is typically very much less than the pillar diameter. The effect of the electrostatic image charge is comparatively small and is included via perturbation theory.

The Hamiltonian for the system is given by:

$$\hat{H} = \hat{H}_0 + \hat{H}_C + \hat{H}_Z + \hat{H}_D, \tag{5.1}$$

where $\hat{H}_0$ describes the energies of the non-interacting particles (see the first term in Eq. 4.4), $\hat{H}_C$ is the energy of the Coulomb interactions described above and $\hat{H}_Z$ is the Zeeman term given by:

$$\hat{H}_Z = \frac{1}{2} g^* \mu_B \sum_i \boldsymbol{\sigma}_i \cdot \mathbf{B}, \tag{5.2}$$

where μ_b is the Bohr magneton, g^* is the effective gyro-magnetic g-factor, σ are the Pauli matrices and B is the applied external magnetic field assumed to be applied perpendicular to the plane of the dot.

The Dresselhaus term ($\hat{H}_D$) has the effect of removing spin as a good quantum number by mixing the spin states. For example, the ground state at $B = 0$ can no longer be considered as a pure spin 0 state and will actually contain a small admixture of spin 1 states. This lifts the selection rule prohibiting transitions between states of differing total spin. The Dresselhaus term also has the effect of lifting the degeneracy of the triplet states at zero magnetic field although this effect is typically very small in comparison to the other terms in the Hamiltonian. We examine the Dresselhaus term and our reasons for choosing it in more detail in section 5.2.1.

In order to calculate the two particle states of the quantum dot system we will construct the Hamiltonian matrix with a Slater determinant basis set of the form given in Eq. 4.1. Instead of considering the symmetric and anti-symmetric spatial functions for spin 0 and spin 1 states separately as we did in chapter 4 we must now consider all possible spin states and construct the matrix accordingly. Once the Hamiltonian matrix is constructed, we diagonalise it using the method described in section 4.2.1.

5.2.1 The Dresselhaus Spin-Mixing Matrix Elements

Due to the selection rules imposed by spin conservation, transitions between states of differing spin will be blocked unless spin can be removed as a good quantum number. In order to include the possibility of spin flip relaxation in our calculations we need to consider the mechanisms capable of removing the spin selection rules.

A. V. Khaetskii and A. Y. Nazarov [25, 26, 27] considered several physical processes that may be responsible for spin flip transitions in GaAs quantum dots. They did this by comparing the relaxation rates calculated with each of the spin-orbit mixing mechanisms in turn. The first mechanism they considered was the spin flip being caused by the admixture of different spin states. The second was the spin-orbit splitting of the electron spectrum due to the strain field produced by the emitted phonons and the third was the relativistic interaction with the electric field caused by the confinement potential. They concluded that it was the spin-orbit admixture term which was dominant.

The admixture terms arise from two of the properties of certain semiconductor crystals, bulk inversion asymmetry (BIA) and structural inversion asymmetry

(SIA). Bulk inversion asymmetry appears in crystals that do not have a centre of inversion symmetry and leads to a **k** dependent splitting of the conduction band. That is, electrons with the same **k** vector but different spins will have different energies. This spin splitting of the conduction band states can be thought of as equivalent to the splitting induced by an internal **k** dependent magnetic field. The spin then precesses around this internal magnetic field, which allows the spin states to mix. This mixing process is frequently referred to as the Dresselhaus mechanism. Structural inversion asymmetry is very similar to BIA except that it arises in the presence of either an external electric field or an internal electric field such as that formed in an asymmetric potential well. The spin mixing that results is frequently referred to as the Rashba mechanism.

Several people have compared the Dresselhaus and Rashba mechanisms in quantum dot systems. M. Valin-Rodriguez *et al.* [63, 64, 65, 66] noted that the Rashba term can be unitarily transformed to have the same form as the Dresselhaus term and therefore only amounts to a redefinition of the coupling constant. Valin-Rodriguez *et al.* also reported that the Rashba term provided negligible spin-orbit coupling for the systems they considered. During the course of this work, S. Dickman and P. Hawrylak [67] and M. Florescu *et al.* [68] also published studies of the Rashba and Dresselhaus mechanisms and reported that the Dresselhaus term is dominant. In addition to this, the Rashba term vanishes in systems with a symmetric confinement potential. For these reasons we will ignore the Rashba mechanism and consider only the Dresselhaus mechanism.

From *Optical Orientation* [71] we have:

$$\hat{H}_D = \gamma_D \boldsymbol{\sigma} \cdot \boldsymbol{\kappa} = \frac{2\hbar^3 \eta}{3m_{cv}} \sqrt{\frac{2m^* E_g}{1 - \frac{\eta}{3}}} \boldsymbol{\sigma} \cdot \boldsymbol{\kappa}, \tag{5.3}$$

where

$$\eta = \frac{\Delta_{SO}}{E_g + \Delta_{SO}} \tag{5.4}$$

and

$$\kappa_x = p_x \left(p_y^2 - p_z^2\right), \tag{5.5}$$

and cyclic permutations thereof where p_x, p_y and p_z are momentum operators. In the presence of a perpendicular magnetic field, the momentum operator $\mathbf{p} \rightarrow \mathbf{p} + e\mathbf{A}$, where it is convenient to take the vector potential in the circular gauge so that $\mathbf{A} = (-y, x, 0)B/2$ and B is the applied magnetic field. The spin orbit splitting of the valence band is Δ_{SO}, the band gap is E_g, m_{cv} is a parameter of the Kane model [76] (which is found from the literature to range between 0.22 and 0.27 for GaAs [65, 72]) and $\boldsymbol{\sigma}$ are the Pauli spin matrices. On expanding the $\boldsymbol{\sigma} \cdot \boldsymbol{\kappa}$ factor in Eq. 5.3 we have:

$$\boldsymbol{\sigma} \cdot \boldsymbol{\kappa} = p_z^2 \left(\sigma_y p_y - \sigma_x p_x\right) + \sigma_x p_x p_y \left(p_y - p_x\right) + \sigma_z p_z \left(p_x^2 - p_y^2\right). \tag{5.6}$$

The first term is proportional to p_z^2 and linear in the in-plane momentum. The second term is independent of p_z but cubic in the in-plane momentum. For the electrostatic quantum dot considered here, the z confinement is very much greater than the in-plane confinement. As a result the $< p_z^2 >$ term will be expected to dominate over the relatively low magnetic fields considered here and the cubic terms may be neglected. The third term vanishes since $< Z_0|p_z|Z_0 >= 0$, where Z_0 is the z dependent ground state wave function.

We begin by considering a single particle system and take the matrix elements of Eq. 5.3 into which we substitute the first term on the right hand side of Eq. 5.6. This gives:

$$\gamma_D \left\langle \phi_b \chi_b \left| p_z^2 \left(\sigma_y p_y - \sigma_x p_x\right) \right| \phi_a \chi_a \right\rangle \tag{5.7}$$

where γ_D is defined in Eq. 5.3. The single particle states used in this work can be separated into radial, angular and perpendicular parts, $\phi(\mathbf{r}) = R(r)\Phi(\phi)Z(z)$. With this notation for the wave functions, the matrix element of expression 5.7 has the form:

$$\begin{aligned}\left\langle Z_b \left| p_z^2 \right| Z_a \right\rangle \times \quad & \{ i\left(\delta_{b\downarrow}\delta_{a\uparrow} - \delta_{a\downarrow}\delta_{b\uparrow}\right) \left\langle R_b(r)\Phi_b(\phi) \left| p_y + eA_y \right| R_a(r)\Phi_a(\phi) \right\rangle - \\ & \left(\delta_{b\uparrow}\delta_{a\downarrow} + \delta_{a\uparrow}\delta_{b\downarrow}\right) \left\langle R_b(r)\Phi_b(\phi) \left| p_x + eA_x \right| R_a(r)\Phi_a(\phi) \right\rangle \} . \quad (5.8)\end{aligned}$$

In order to evaluate the matrix element, the derivatives of the Fock-Darwin states $(R(r)\Phi(\phi))$ must be calculated. The Fock-Darwin states are functions of r and θ, but we require x and y derivatives. It would therefore simplify the calculation if we were able to remove the need to evaluate these derivatives. We can achieve this by using the relationship:

$$\begin{aligned}\left\langle \alpha \left| p_x + eA_x \right| \beta \right\rangle &= \frac{m^*}{i\hbar} \left\langle \alpha \left| x\hat{H}_0 - \hat{H}_0 x \right| \beta \right\rangle \\ &= \frac{m^*}{i\hbar} \left(E_\beta - E_\alpha\right) \left\langle \alpha \left| x \right| \beta \right\rangle . \quad (5.9)\end{aligned}$$

This is a generalisation of the standard result found in many quantum mechanics text books (see for example Bransden and Jochain [73]) which allows for the application of a magnetic field in the z direction. As mentioned previously this manipulation enables the matrix elements in expression 5.8 to be simplified but also has the significant benefit of allowing a magnetic field to be included in the calculation with no additional effort.

Expression 5.8 then becomes:

$$\begin{aligned}&\left\langle Z_b(z) \left| p_z^2 \right| Z_a(z) \right\rangle \frac{m^*}{i\hbar} \left(E_b - E_a\right) \times \\ &\{ i\left(\delta_{b\downarrow}\delta_{a\uparrow} - \delta_{a\downarrow}\delta_{b\uparrow}\right) \left\langle R_b(r)\Phi_b(\phi) \left| y \right| R_a(r)\Phi_a(\phi) \right\rangle - \\ &\left(\delta_{b\uparrow}\delta_{a\downarrow} + \delta_{a\uparrow}\delta_{b\downarrow}\right) \left\langle R_b(r)\Phi_b(\phi) \left| x \right| R_a(r)\Phi_a(\phi) \right\rangle \} . \quad (5.10)\end{aligned}$$

The matrix elements of x and y are given by the integrals:

$$
\begin{aligned}
\langle R_b(r)\Phi_b(\phi)\,|x|\,R_a(r)\Phi_a(\phi)\rangle &= \frac{1}{2\pi}\int r^2 R_b^*(r)R_a(r)\exp(i(l_a-l_b)\phi)\cos\phi dr d\phi \\
&= \frac{1}{2}\delta_{|l_a-l_b|,1}\int_0^\infty r^2 R_b j(r)R_a^*(r)dr,
\end{aligned}
$$

$$
\begin{aligned}
\langle R_b(r)\Phi_b(\phi)\,|y|\,R_a(r)\Phi_a(\phi)\rangle &= \frac{1}{2\pi}\int r^2 R_b^*(r)R_a(r)\exp(i(l_a-l_b)\phi)\sin\phi dr d\phi \\
&= \frac{i}{2}\left(l_a-l_b\right)\delta_{|l_a-l_b|,1}\int_0^\infty r^2 R_b^*(r)R_a(r)dr. \qquad (5.11)
\end{aligned}
$$

From Eq. 5.11 we have the relationship $<\phi_b|y|\phi_a>= i(l_b-l_a) <\phi_b|x|\phi_a>$ which allows us to simplify expression 5.10 to give:

$$
\begin{aligned}
&\frac{m^*}{2i\hbar}\left(E_b-E_a\right)\delta_{|l_a-l_b|,1}\left\{\left(l_a-l_b\right)\left(\delta_{a\downarrow}\delta_{b\uparrow}-\delta_{b\downarrow}\delta_{a\uparrow}\right)-\left(\delta_{b\uparrow}\delta_{a\downarrow}+\delta_{a\uparrow}\delta_{b\downarrow}\right)\right\}\times \\
&\left\langle Z_b\left|p_z^2\right|Z_a\right\rangle\int_0^\infty r^2 R_b^*(r)R_a(r)dr. \qquad (5.12)
\end{aligned}
$$

From the first Kronecker delta, it is apparent that there are two cases where expression 5.12 can be non-zero, namely $|l_a| = |l_b|+1$ and $|l_a| = |l_b|-1$. Using these selection rules and the radial part of the Fock-Darwin states (Eq. 2.1), we can evaluate the integral in expression 5.12 to give:

$$
\begin{aligned}
\int_0^\infty r^2 R_b^*(r)R_a(r)dr = &\frac{(n_a+|l_a|)!}{n_a!}\delta_{|l_a|,|l_b|+1}\left[\delta_{n_a n_b}-\delta_{n_a,n_b-1}\right]+ \\
&\frac{(n_b+|l_b|)!}{n_b!}\delta_{|l_a|,|l_b|-1}\left[\delta_{n_a n_b}-\delta_{n_b,n_a-1}\right]. \qquad (5.13)
\end{aligned}
$$

The single particle Dresselhaus matrix element of expression 5.7 is then given by expression 5.12 and Eq. 5.13.

We can use this theory to find the Dresselhaus matrix elements for the two-particle system. We do this by using the Slater determinant wave functions given in Eq. 4.1 and the two-particle analogue of Eq. 5.3:

$$
\hat{H}_D = \gamma_D\left(\boldsymbol{\sigma}_{(1)}\cdot\boldsymbol{\kappa}_{(1)}+\boldsymbol{\sigma}_{(2)}\cdot\boldsymbol{\kappa}_{(2)}\right) \qquad (5.14)
$$

where the subscripts refer to the first (1) or second (2) particle in the Slater determinant. The two-particle matrix element of Eq. 5.3 is then given by:

$$\gamma_D \left[\delta_{b_2 a_2} \langle \phi_{b_1} \chi_{b_1} | \boldsymbol{\sigma} \cdot \boldsymbol{\kappa} | \phi_{a_1} \chi_{a_1} \rangle + \delta_{b_2 a_2} \langle \phi_{b_1} \chi_{b_1} | \boldsymbol{\sigma} \cdot \boldsymbol{\kappa} | \phi_{a_1} \chi_{a_1} \rangle - \right.$$
$$\left. \delta_{b_2 a_2} \langle \phi_{b_1} \chi_{b_1} | \boldsymbol{\sigma} \cdot \boldsymbol{\kappa} | \phi_{a_1} \chi_{a_1} \rangle - \delta_{b_2 a_2} \langle \phi_{b_1} \chi_{b_1} | \boldsymbol{\sigma} \cdot \boldsymbol{\kappa} | \phi_{a_1} \chi_{a_1} \rangle \right]. \qquad (5.15)$$

The Kronecker deltas preceding each of the individual integrals in expression 5.15 arise from the orthogonality condition of the single particle HO wave functions used in the Slater determinant.

5.2.2 The Two Particle States

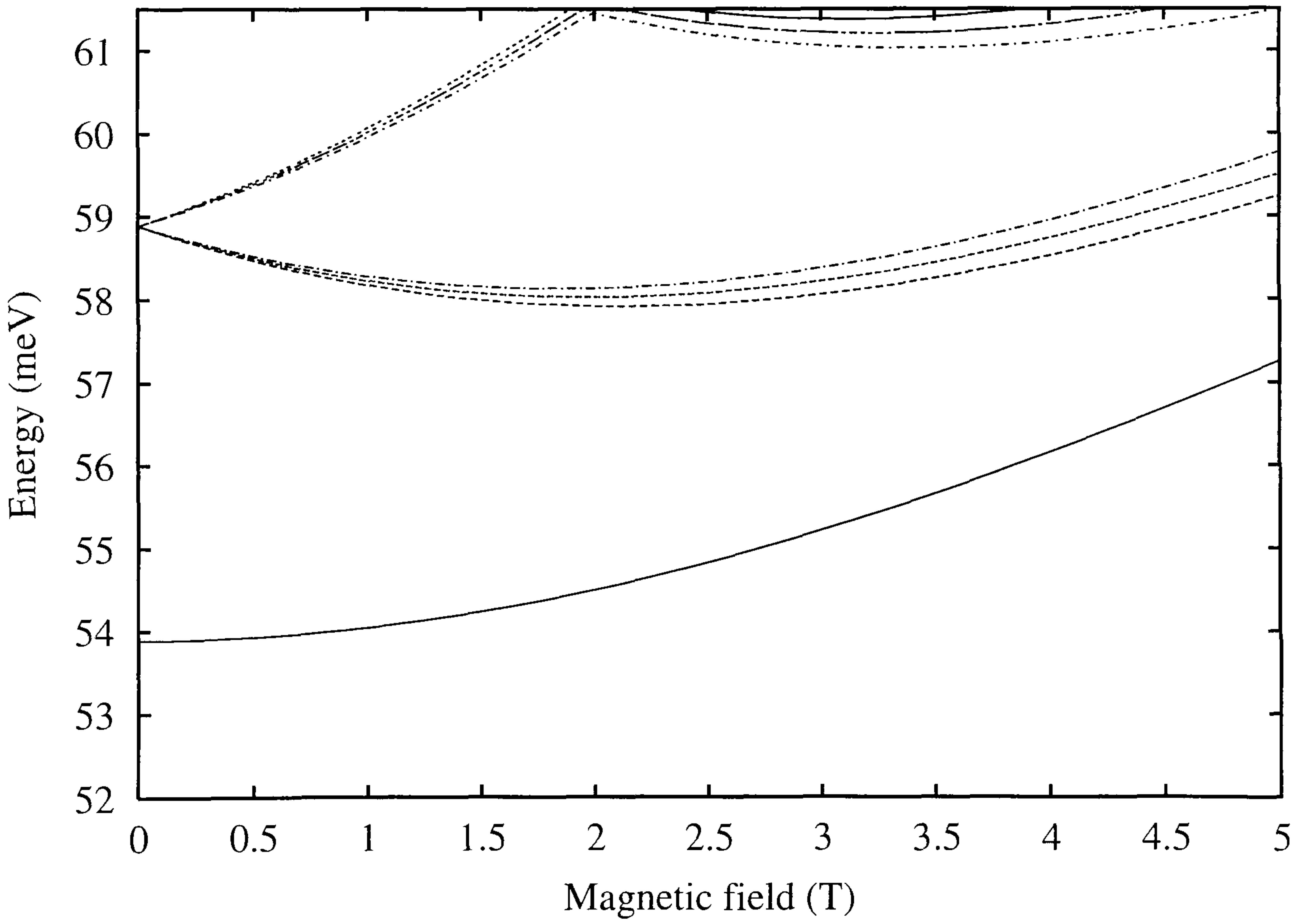

Figure 5.2: The energy levels of a two particle non-interacting electrostatic quantum dot without spin-orbit coupling as a function of external magnetic field. Lateral confinement energy is 5meV.

The energy spectrum for two non-interacting particles is shown in figure 5.2 as a function of magnetic field. The gyro-magnetic factor used in this and subsequent calculations is $g = -0.46$ found from experimental data [70]. This was the best available estimate at the time the work was completed but has since been revised to $g = -0.3$ [74]. The electronic effective mass is $m^* = 0.065$. We use lower case letters to denote the quantum numbers of the single particle wave functions. Quantum numbers for the two particle wave functions are denoted by upper case letters. The two triplet states separating at $\approx$ 59meV correspond to angular momentum of $L = -1$ for the upper branch and $L = 1$ for the lower branch. Each branch has 4 distinct levels, with spins of $S_z = -1, 0, 1$ from top to bottom. The centre ($S_z = 0$) line of each triplet state is two-fold degenerate corresponding to total spin states of $S = 0$ and $S = 1$.

The inclusion of the Coulomb interaction has a pronounced effect on the energy levels. Figure 5.3 shows the energy spectrum as a function of externally applied magnetic field for the states given in table 5.1. The quantum numbers used to label the states in table 5.1 correspond to a magnetic field of $B = 0.5$T. This field strength is used only to allow quantum numbers to be unambiguously associated with distinct energy levels since at $B = 0$T, the $L = \pm 1$ states are degenerate. States will subsequently be referred to by the state number given in this table. All parameters are the same as used in figure 5.2.

In the energy spectrum for the non-interacting states as shown in figure 5.2, the $L = \pm 1$, $S_z = 0$ states (states 2 and 7) are degenerate. This degeneracy is lifted in the presence of a magnetic field by the inclusion of the Coulomb interaction. The Pauli exclusion principle requires that for spin-polarised electrons, the exact wave function must vanish when the two electrons are in the same spatial state, thus

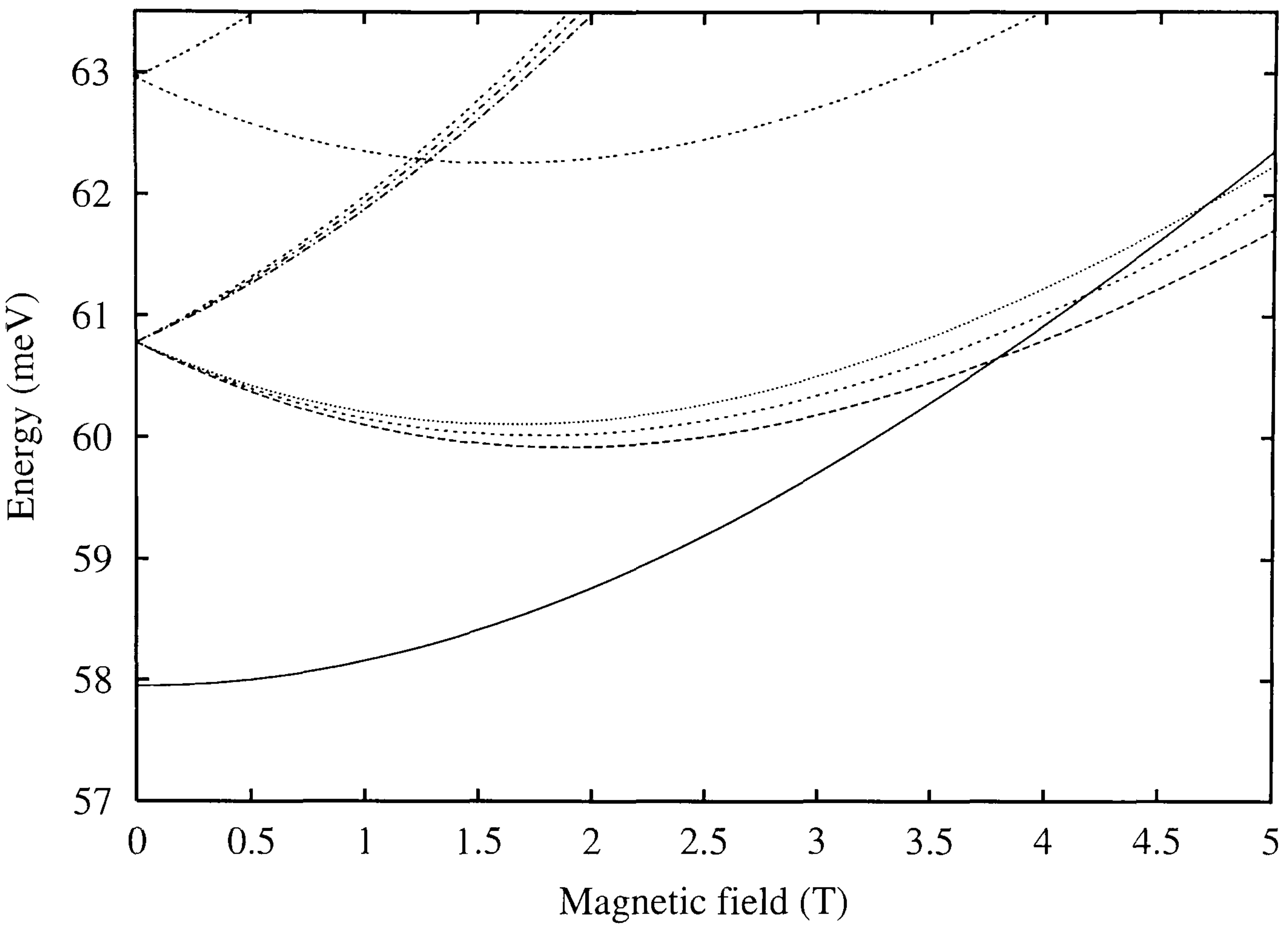

Figure 5.3: The energy levels against external magnetic field for a two particle electrostatic quantum dot interacting via the Coulomb potential. Lateral confinement energy is 5meV.

reducing the Coulomb energy. The triplet states branching out from ≈ 60.8meV (states 1-6) correspond to total spin $S = 1$ with $S_z = 0, \pm 1$ whereas the singlet states splitting at ≈ 63.0meV (states 7 and 8) correspond to total spin $S = 0$ with $S_z = 0$.

We now include the spin-mixing term (Eq. 5.3). This lifts the zero magnetic field degeneracy of the singlet and triplet states. The mixing of different spin and angular momentum states means that individual states will no longer have a definite spin orientation or angular momentum quantum number. However, we can find the quasi-spin of the state by calculating the $< S_z >$ expectation value. Since spin mixing is a very small effect, the resulting expectation values are all close to the values gained for the non-spin mixed states. Even though the

State	Energy at $B = 0.5$T (meV)	L	S	S_z
0	57.99	0	0	0
1	60.35	1	1	1
2	60.39	1	1	0
3	60.44	1	1	-1
4	61.24	-1	1	1
5	61.28	-1	1	0
6	61.32	-1	1	-1
7	62.58	1	0	0
8	63.47	-1	0	0

Table 5.1: Quantum numbers for the states in figure 5.3 at $B = 0.5$T. This magnetic field is used only to allow quantum numbers to be unambiguously associated with energy levels.

quasi-spin and quasi-angular momentum have no value with regard to selection rules, they can still be a useful way of labeling the quantum states. The $< S_z >$ expectation value is given by:

$$\langle S_z \rangle = \sum_n a_n^* a_n \left[\chi_{1n}^T \sigma_z \chi_{1n} + \chi_{2n}^T \sigma_z \chi_{2n} \right]. \tag{5.16}$$

The angular momentum expectation values can be calculated in a similar way. The quasi-quantum numbers typically differ from the integer quantum numbers in table 5.1 by less than 0.1%. The exception to this is at $B \approx 4.7$T where the quasi-quantum numbers for states 0 and 3 change places with each other due to the emergence of an anti-crossing in the energy spectrum. This anti-crossing will be discussed further in section 5.2.3.

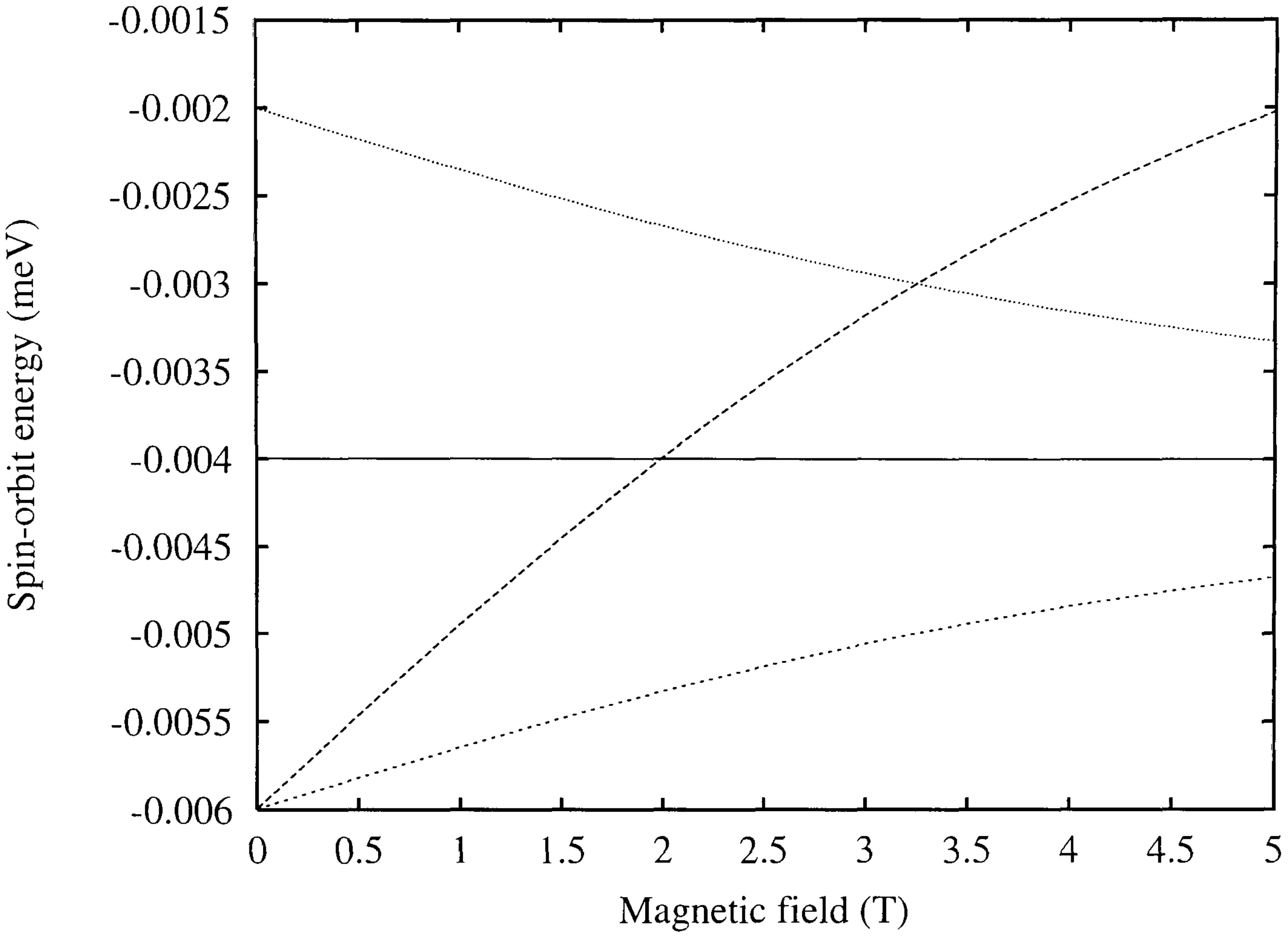

Figure 5.4: The Dresselhaus spin-orbit contribution to energy of singlet and triplet states in table 5.1. The solid line denotes state 0, the coarse dotted line denotes state 1, the medium dotted line state 2 and the fine dotted line state 3.

Figure 5.4 shows the Dresselhaus contribution to the total energy. The spin-orbit coupling parameters used in this calculation (see Eq. 5.3) are $m_{cv} = 0.27$ [72], $\Delta_{SO} = 0.34$eV and $E_g = 1.52$eV. The spin-orbit energies in figure 5.4 are found to be in agreement with energies calculated by M. Valin-Rodriguez *et al.* [65, 64].

After the bulk of this work had been completed, S. Dickman, P. Hawrylak [67] and M. Florescu *et al.* [68] (members of the same group), published studies concerning both Rashba and Dresselhaus admixture mechanisms in an approximate treatment of the spin flip relaxation in a two electron interacting

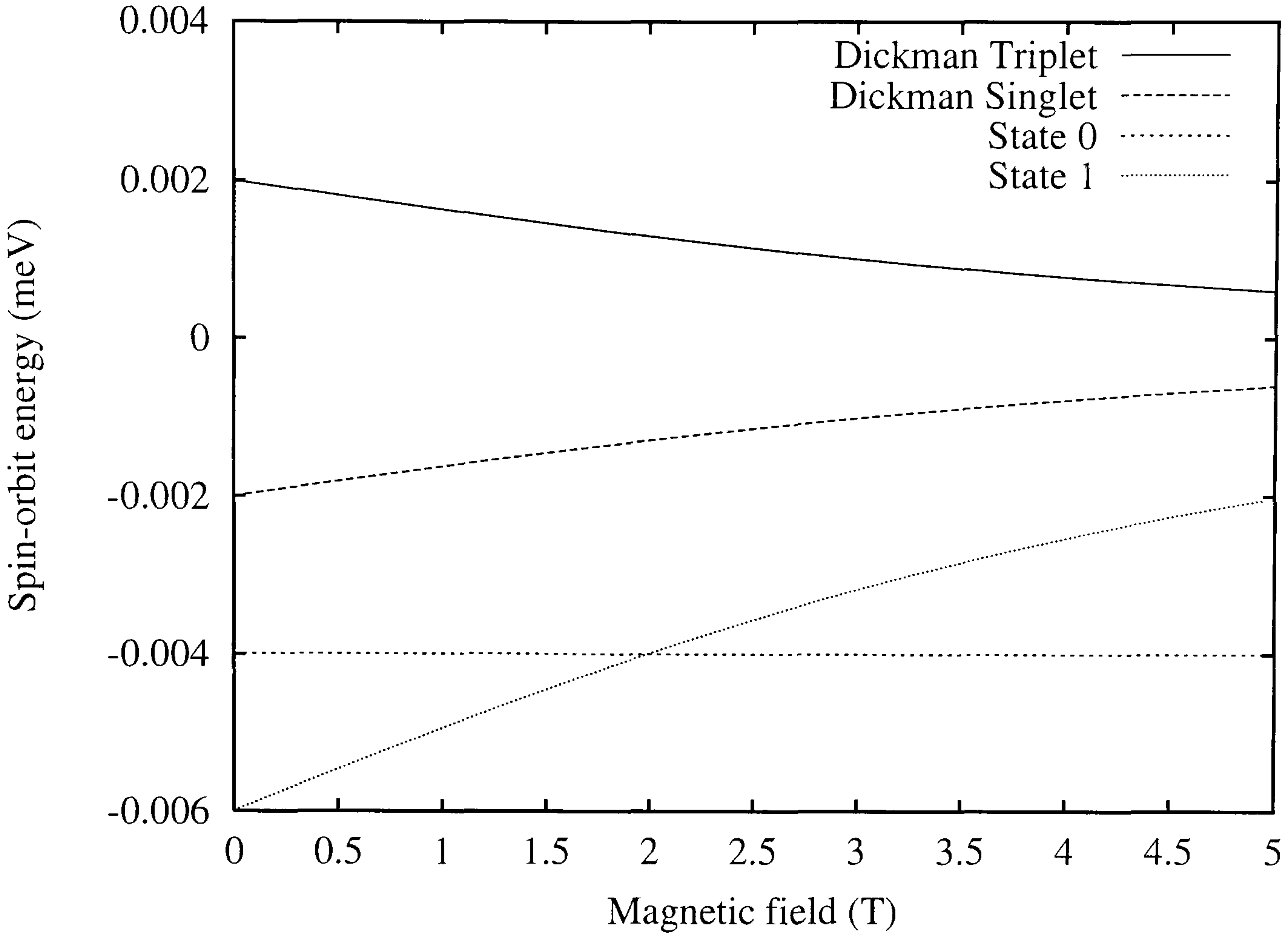

Figure 5.5: The spin-orbit energy against magnetic field for the singlet and triplet states of S. Dickman *et al* [67] compared with the corrections calculated for the equivalent states (states 0 and 1) from figure 5.4.

system. In both papers, Dickman *et al.* [67] and Florescu *et al.* [68] used a basis set of 4 states. This basis set does not appear to give converged energy eigenvalues. To illustrate this, figure 5.5 shows a comparison between the spin-orbit corrections for the singlet and triplet states of Dickman *et al.* and the equivalent energies for state 0 (singlet) and state 1 (triplet) calculated in this work. We find that we need to include basis states with quantum numbers of at least $n = 0, 1$, $l = 0, \pm 1$, $s = 0, \pm 1$ before even the sign of the triplet state spin-orbit energy correction is correct. We also find that we need to increase n and $|l|$ to 3 before convergence to better than 0.1% is achieved.

Since the Dresselhaus spin-orbit contribution to the total energy is so small, the energy spectrum including spin-orbit contribution does not look significantly different from that of Figure 5.3. However there are differences, the most significant being the emergence of the anti-crossing in the energy spectrum, which is shown in detail in figure 5.6. The anti-crossing appears for the ground state and state 3 at $B = 4.7$T, when the linear Dresselhaus spin-orbit mechanism is included. The other crossings involving the ground state remain as crossings. At the energy anti-crossing, the quasi-quantum numbers behave as though the states crossed. Since we choose to label the states by tracking continuous energy levels, the quasi-quantum numbers of states 3 and 0 effectively swap quite abruptly. Explicitly, at $B > 4.72$T, state 0 has quasi-quantum numbers of $L \approx S \approx 1$ and $S_z \approx 0$ whereas state 3 has quasi-quantum numbers of $L \approx S \approx S_z \approx 0$ instead of the values given in table 5.1. All other crossings in the $L \approx 1$ triplet state remain as crossings.

Interestingly, C. F. Destefani *et al.* [75] report that in InSb dots where spin mixing is much stronger than in the system considered here, the inclusion of the cubic Dresselhaus terms (which has been neglected in this work) causes the emergence of additional, but almost imperceptible, anti-crossings in the Fock-Darwin energy spectrum.

5.2.3 The Anti-Crossings

In the previous section, we saw that the Dresselhaus spin mixing term given in Eq. 5.3 and discussed in section 5.2.1 leads to the emergence of anti-crossings in the energy spectrum. To explain this effect, we will consider a single particle HO system with a basis set restricted to include only the $L = \pm 1$ excited states of Eq. 2.1. This gives a 6×6 matrix which we are able to diagonalise analytically.

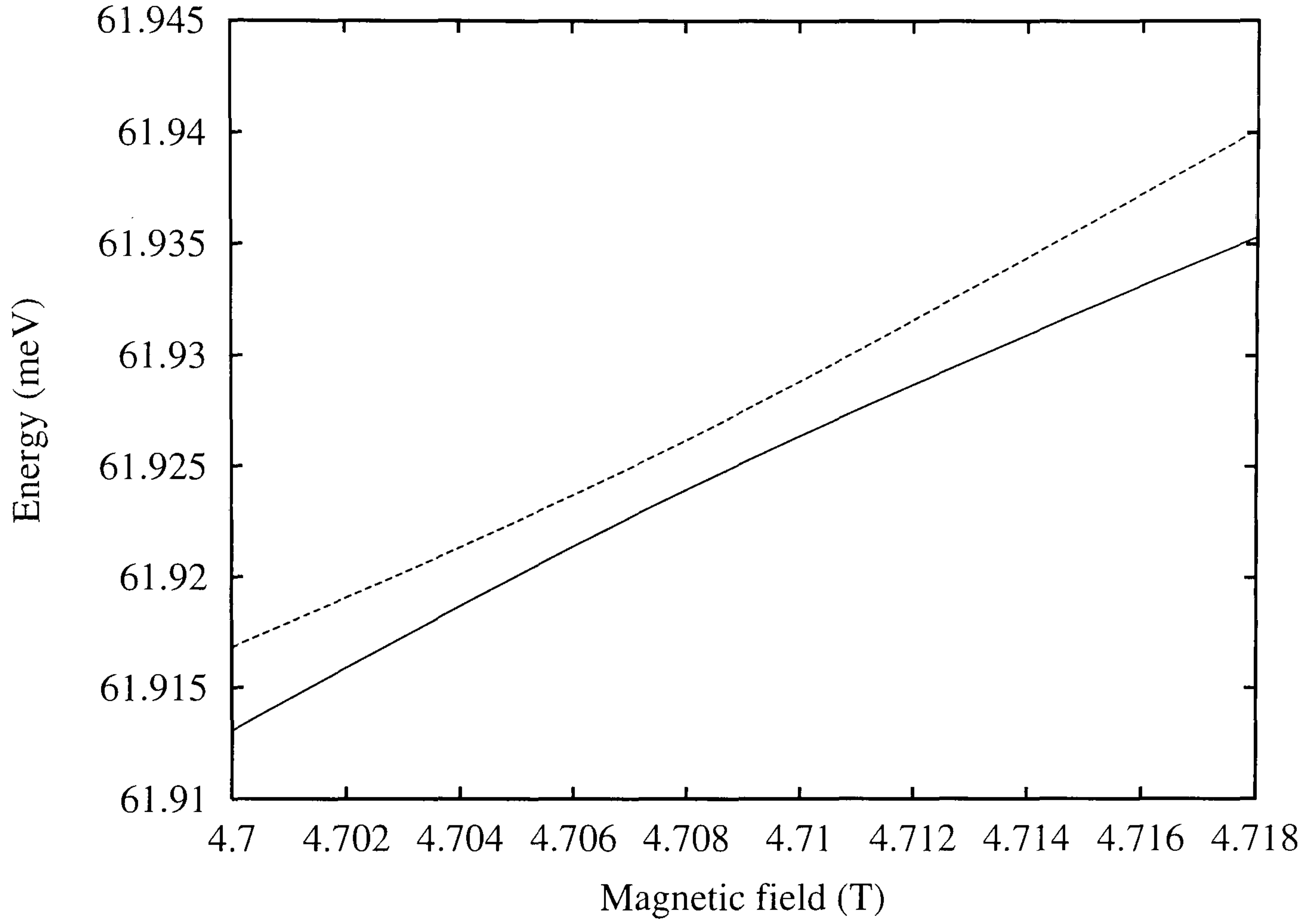

Figure 5.6: The anti-crossing that appears in the energy levels of state 0 and state 3 (defined in table 5.1) as a result of the Dresselhaus spin mixing mechanism.

The Hamiltonian of the single particle system is $\hat{H} = \hat{H}_0 + \hat{H}_D + \hat{H}_Z$ where the terms are defined as for Eq. 5.1. The matrix is then given by table 5.2 where the $\hat{H}_0$ matrix elements take three values given by $H_\pm = 2\hbar\Omega \pm \hbar\omega_c/2$ and $H_0 = \hbar\Omega$, and $H_Z = g^*\mu_B B/2$. The Dresselhaus matrix elements can be calculated from expression 5.12 and Eq. 5.13 and are $H_D^{(1)} =< p_z^2 > m^*\lambda(\Omega - \omega_c/2)$ and $H_D^{(3)} =< p_z^2 > m^*\lambda(-\Omega - \omega_c/2)$ where Ω is given by Eq. 2.3 and ω_c is the cyclotron frequency.

The matrix in table 5.2 has a block diagonal structure, which is due to the selection rule $\delta_{l_a - l_b,1}\delta_{a\uparrow}\delta_{b\downarrow} + \delta_{l_a-l_b,-1}\delta_{a\downarrow}\delta_{b\uparrow} \neq 0$ from expression 5.12. The eigenvalues of this matrix are found to be $\mu = H_- + H_Z$, $\mu = H_+ - H_Z$ and the

	$\vert -1\uparrow>$	$\vert -1\downarrow>$	$\vert 0\uparrow>$	$\vert 0\downarrow>$	$\vert 1\uparrow>$	$\vert 1\downarrow>$
$\vert -1\uparrow>$	$H_- + H_Z$					
$\vert -1\downarrow>$		$H_- - H_Z$	$iH_D^{(1)}$			
$\vert 0\uparrow>$		$-iH_D^{(1)}$	$H_0 + H_Z$			
$\vert 0\uparrow>$				$H_0 - H_Z$	$iH_D^{(3)}$	
$\vert 1\uparrow>$				$-iH_D^{(3)}$	$H_+ + H_Z$	
$\vert 1\downarrow>$						$H_+ - H_Z$

Table 5.2: Single particle 6 × 6 matrix including Dresselhaus spin mixing and Zeeman terms. Basis states are labeled by angular momentum quantum number and electron spin orientation.

solutions to:

$$\mu^2 - (H_- + H_0)\mu + (H_- - H_Z)(H_0 + H_Z) - H_D^{(1)2} = 0 \tag{5.17}$$

and

$$\mu^2 - (H_0 + H_+)\mu + (H_+ + H_Z)(H_0 - H_Z) - H_D^{(3)2} = 0. \tag{5.18}$$

The energy levels depend on magnetic field through the Zeeman term H_z and the individual particle term H_0. In this single particle case, the sign of the g^* factor appearing in the Zeeman term (H_Z) determines whether Eq. 5.17 gives rise to an anti-crossing. If the g^* factor is positive, we get an anti-crossing from the two solutions to Eq. 5.17. If the g^* factor is negative, the two energy levels from Eq. 5.17 move apart with increasing magnetic field and a crossing arises from one of the solutions to Eq. 5.18 and $\mu = H_- + H_Z$. For a negative g^* factor, the energy spectrum of the single particle system does not display an anti-crossing. In the two particle system, the sign of the g^* factor determines which branch of the $L \approx 1$, $S_z \approx \pm 1$ triplet state exhibits an anti-crossing. Both the crossing and anti-crossing energy levels from Eq. 5.17 are presented in figure 5.7 where we have used the unrealistic value of $g^* = \pm 10$ in order to artificially enhance the anti-crossing to make it more visible. The anti-crossing is shifted upwards in energy by 5meV for clarity. If the Dresselhaus term is neglected, the matrix is diagonal and the anti-crossings vanish.

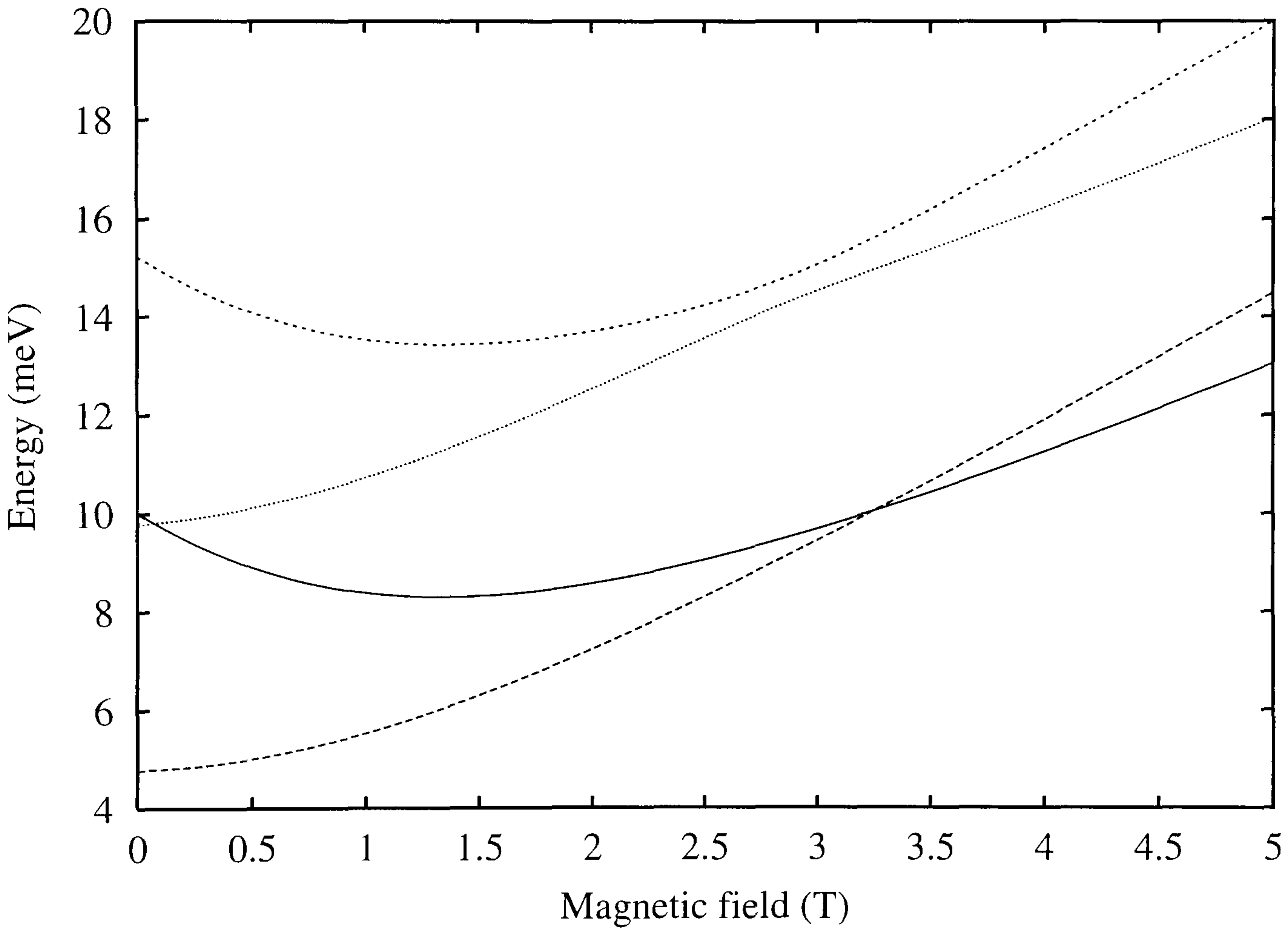

Figure 5.7: Anti-crossing in the single particle energy levels as a result of the Dresselhaus spin mixing mechanism. The energy levels displaying an anti-crossing arise from the solution to Eq. 5.17 with $g^* = 10$ and are shifted higher in energy by 5meV for clarity. The crossing is calculated with $g^* = -10$.

From the selection rule $\delta_{l_a - l_b, 1}\delta_{a\uparrow}\delta_{b\downarrow} + \delta_{l_a - l_b, -1}\delta_{a\downarrow}\delta_{b\uparrow} \neq 0$ (expression 5.12) that leads to the block diagonal structure of the matrix, we find there are two possibilities that can give rise to a non-zero Dresselhaus matrix element. First when $l_a = l_b + 1$ and $\delta_{a\uparrow}\delta_{b\downarrow}$=1; and second when $l_a = l_b - 1$ and $\delta_{a\downarrow}\delta_{b\uparrow}$=1. In either case it is possible to show that $l_a - s_a = l_b - s_b$. This suggests that $l_z - s_z$ might be conserved for the linear Dresselhaus spin-mixing term applied to single particles. Indeed, after some algebra we can show the commutator relation:

$$[\hat{l}_z - \hat{s}_z, (\sigma_y p_y - \sigma_x p_x)p_z^2] = 0, \tag{5.19}$$

and we have confirmed that this holds in the presence of a magnetic field when $\mathbf{p} \rightarrow \mathbf{p} + e\mathbf{A}$. This relationship can be generalised to two electron systems where it is found that the sum $l_{z_1} - s_{z_1} + l_{z_2} - s_{z_2}$ is conserved. Each block of the Hamiltonian is labelled by a different value of $L_z - S_z$, levels with the same value cannot cross but levels from different blocks can. The commutator relation given in Eq. 5.19 has not been published previously to the best of our knowledge. This commutator relation does not hold when the cubic Dresselhaus spin-orbit coupling terms are included.

5.3 Spin Relaxation Mechanisms

In order to calculate the spin flip relaxation rate in electrostatic dots we must first consider the possible mechanisms. If spin is no longer a good quantum number, any relaxation mechanism could theoretically provide energy relaxation between different quasi-spin states. However, there would appear to be a distinct lack of external carriers surrounding the electrostatic dot considered here, effectively ruling out Auger relaxation.

We may then consider phonon relaxation as a possible mechanism. Two main phonon-coupling mechanisms are deformation potential coupling and piezoelectric coupling. Since it is unclear which of these mechanisms is dominant, we shall consider both.

5.3.1 Deformation Potential Scattering

We begin by considering the deformation potential interaction Hamiltonian [76, 77] given by:

$$\hat{H}_D = iD\sqrt{\frac{\hbar q}{2V\rho c_s}}\exp\left(i\mathbf{q}\cdot\mathbf{r}\right) + c.c. \tag{5.20}$$

where D is the deformation potential, ρ is the mass density, c_s is the speed of sound which we assume to be isotropic and V is the volume of the sample.

Considering phonon emission, from Fermi's Golden Rule (expression 3.2) we have:

$$\frac{2\pi}{\hbar}\sum\left|\left\langle\Psi_f\left|\hat{H}_D\right|\Psi_i\right\rangle\right|^2\left[N\left(q\right)+1\right]\delta\left[E_f - E_i + \hbar c_s q\right], \tag{5.21}$$

where $N(q)$ is the Bose-Einstein distribution that gives the number of phonons that occupy a mode of the wave vector $\mathbf{q}$. The distribution function factor appears in the form $N(q)+1$ to allow for the possibility of spontaneous and stimulated emission. On substituting the RHS of Eq. 5.20 into expression 5.21 we find the matrix element in the expression is given by:

$$\begin{aligned}&\sum_{fi}\frac{a_f^* a_i'}{2}\int\left[\phi_{1f}^*\left(\mathbf{r}_1\right)\phi_{2f}^*\left(\mathbf{r}_2\right) - \phi_{1f}^*\left(\mathbf{r}_2\right)\phi_{2f}^*\left(\mathbf{r}_1\right)\right]\times\\&\left[\exp\left(i\mathbf{q}\cdot\mathbf{r}_1\right)+\exp\left(i\mathbf{q}\cdot\mathbf{r}_2\right)\right]\times\\&\left[\phi_{1i}\left(\mathbf{r}_1\right)\phi_{2i}\left(\mathbf{r}_2\right) - \phi_{1i}\left(\mathbf{r}_2\right)\phi_{2i}\left(\mathbf{r}_1\right)\right]d\mathbf{r}_1 d\mathbf{r}_2,\end{aligned} \tag{5.22}$$

where a_i' and a_f are the complex amplitudes for the eigenvectors of the initial and final two particle states (Eq. 4.3) found by the diagonalisation of the Hamiltonian matrix.

We can write the single particle states as $\phi(\mathbf{r}) = R(r)\Phi(\phi)Z(z)$. In this work $Z(z)$ is always the ground state because we truncate the basis set and do not consider the relatively high-energy excitations in the finite well. The matrix element then simplifies to:

$$iD\sqrt{\frac{\hbar q}{2V\rho c_s}}G\left(q_\perp\right)F\left(q_\parallel\right), \tag{5.23}$$

where

$$\begin{aligned}F(q_\parallel) = \quad & \sum_{fi} a_f^* a_i' \left\{\delta_{2f,2i}\left\langle\phi_{1f}\left(r\right)\left|e^{i\mathbf{q}_\parallel\cdot\mathbf{r}}\right|\phi_{1i}\left(r\right)\right\rangle + \delta_{1f,1i}\left\langle\phi_{2f}\left(r\right)\left|e^{i\mathbf{q}_\parallel\cdot\mathbf{r}}\right|\phi_{2i}\left(r\right)\right\rangle - \right. \\ & \left. \delta_{2f,1i}\left\langle\phi_{1f}\left(r\right)\left|e^{i\mathbf{q}_\parallel\cdot\mathbf{r}}\right|\phi_{2i}\left(r\right)\right\rangle - \delta_{1f,2i}\left\langle\phi_{2f}\left(r\right)\left|e^{i\mathbf{q}_\parallel\cdot\mathbf{r}}\right|\phi_{1i}\left(r\right)\right\rangle\right\} \end{aligned} \tag{5.24}$$

and

$$G\left(q_\perp\right) = \left\langle Z\left(z\right)\left|e^{iq_\perp z}\right|Z\left(z\right)\right\rangle. \tag{5.25}$$

Substituting expression 5.23 into the Golden rule (expression 5.21) we find the relaxation rate is given by:

$$\frac{2\pi}{\hbar}\frac{V}{8\pi^3}\frac{\hbar D^2}{2\rho V c_s}\int q\left|G\left(q_\perp\right)F\left(q_\parallel\right)\right|^2\left[N\left(q\right)+1\right]\delta\left[E_f - E_i + \hbar q c_s\right]d\mathbf{q}, \tag{5.26}$$

where

$$N\left(q\right) = \left[\exp\left(\frac{\hbar c_s q}{k_B T}\right) - 1\right]^{-1}. \tag{5.27}$$

We can simplify the delta function in expression 5.26 by making the substitutions $\delta[E_f - E_i + \hbar c_s q] = (\hbar c_s)^{-1}\delta[q_0 + q]$, where $q_0 = (E_f - E_i)/\hbar c_s$. The delta function is then removed by integrating in spherical polar coordinates over q and ϕ to give:

$$\frac{D^2 q_0^3}{4\pi\hbar\rho c_s^2}\left[N\left(q_0\right)+1\right]\int_0^\pi\left|G\left(q_0\cos\theta\right)F\left(q_0\sin\theta\right)\right|^2\sin\theta d\theta. \tag{5.28}$$

The rectangular well ground state $Z(z)$ is:

$$\begin{aligned} Z\left(z\right) &= \frac{A}{\sqrt{w}}\cos\left(\frac{az}{w}\right) & |z| \leq w \\ Z\left(z\right) &= \frac{A}{\sqrt{w}}\cos\left(a\right)\exp\left[-b\left(\left|\frac{z}{w}\right| - 1\right)\right] & |z| > w \end{aligned} \tag{5.29}$$

where

$$\begin{aligned} a &= \frac{w}{\hbar}\sqrt{2m^{*}E_{z}}, \\ b &= \frac{w}{\hbar}\sqrt{2m^{*}\left(V_{0}^{*}-E_{z}\right)}, \\ A &= \left[1+\frac{\sin\left(2a\right)}{2a}+\frac{\cos^{2}\left(a\right)}{b}\right]^{-\frac{1}{2}}, \end{aligned} \tag{5.30}$$

w is the well half-width, V_0^* is the effective barrier height and E_z is the z ground state energy. The expression for $G(q_\perp)$ is found by substituting these expressions into Eq. 5.25 to give:

$$\begin{aligned} G\left(q_{\perp}\right) = \quad & 2A^{2}\cos^{2}\left(a\right)\left[\frac{2b\cos\left(q_{\perp}w\right)-q_{\perp}w\sin\left(q_{\perp}w\right)}{4b^{2}+q_{\perp}^{2}w^{2}}\right]+ \\ & \frac{A^{2}}{2}\left[\frac{\sin\left(q_{\perp}w+2a\right)}{q_{\perp}w+2a}+\frac{\sin\left(q_{\perp}w-2a\right)}{q_{\perp}w-2a}+\frac{2\sin\left(q_{\perp}w\right)}{q_{\perp}w}\right]. \end{aligned} \tag{5.31}$$

5.3.2 Piezoelectric Scattering

In order to derive the piezoelectric potential for phonon relaxation, we begin with Poisson's equation:

$$\nabla^{2}\varphi = -\frac{\nabla\cdot\mathbf{P}}{\epsilon\epsilon_{0}} \tag{5.32}$$

where φ is the piezoelectric potential and $\mathbf{P}$ is the vector dipole moment per unit volume due to the deformation of the crystal lattice. From Eq. 5.32 we find the piezoelectric potential ($\varphi_{\iota,\mathbf{q}}$) due to a single ι-mode acoustic phonon with wave vector $\mathbf{q}$ as:

$$\varphi_{\iota,\mathbf{q}} = -i\frac{\mathbf{q}\cdot\mathbf{P}_{\iota,\mathbf{q}}}{\epsilon\epsilon_{0}q^{2}} \tag{5.33}$$

The ith component of the electric polarisation is $P^{i}_{\iota,\mathbf{q}} = \sum_{jk} h_{ijk}s_{jk}(\mathbf{r},t)$ where h_{ijk} is the piezoelectric tensor and $s_{jk}(\mathbf{r},t) = \frac{1}{2}(\frac{\partial u_j}{\partial x_k} + \frac{\partial u_k}{\partial x_j})$ is the strain tensor. We substitute the strain tensor for a phonon to give:

$$P^{i}_{\iota,\mathbf{q}} = i\sum_{jk}\frac{h_{ijk}}{2}\sqrt{\frac{\hbar}{2\rho c_{s}qV}}\left(d^{j}_{\iota,\mathbf{q}}q_{k}+d^{k}_{\iota,\mathbf{q}}q_{j}\right)\left\{\exp\left[i\left(\mathbf{q}\cdot\mathbf{r}\right)\right]-c.c.\right\} \tag{5.34}$$

where $d^j_{\iota,\mathbf{q}}$ is the polarisation vector of the ι-mode phonon. Now $\mathbf{q}\cdot\mathbf{P}_{\iota,\mathbf{q}} = \sum_i q_i P^i_{\iota,\mathbf{q}}$ so we can substitute Eq. 5.34 into Eq. 5.33. We then write the piezoelectric potential as $\hat{H}_P = e_0\varphi_{\iota,\mathbf{q}}$, where e_0 is the electronic charge. This gives the piezoelectric Hamiltonian for emission of a phonon to be:

$$\hat{H}_P = \frac{e_0 h_\iota}{2\epsilon\epsilon_0}\sqrt{\frac{\hbar}{2V\rho c_s q}}\exp\left(i\mathbf{q}\cdot\mathbf{r}\right), \tag{5.35}$$

where

$$h_\iota = \sum_{ijk} h_{ijk}\frac{q_i}{q}\left(d^j_\iota\frac{q_k}{q} + d^k_\iota\frac{q_j}{q}\right). \tag{5.36}$$

The piezoelectric tensor h_{ijk}, transforms as [78]:

$$h'_{ijk} = \sum_{lmn} a_{il}a_{jm}a_{kn}h_{lmn}, \tag{5.37}$$

where a_{il}, a_{jm} and a_{kn} are transformation matrices. Applying this transformation over various rotations leads to the standard result $|h_{ijk}| = |h_{14}|$ where $i \neq j \neq k$. Piezoelectric tensors with repeated indices vanish for crystals of a zinc-blende structure. The piezoelectric phonon polarisation vector $\mathbf{d}_\iota$ can have three different modes (one LA mode and two TA modes) depending on the polarisation of the emitted phonon. The vector $\mathbf{d}_\iota$ has the same form as the standard spherical polar coordinate unit vectors $\mathbf{r}_0$, θ_0 and ϕ_0 (see G. Arfken [79] for example).

We are now in a position to find an expression for the piezoelectric relaxation rate. With Eq. 5.35 as the perturbation operator in the Golden Rule (expression 3.2), the matrix element for piezoelectric relaxation is:

$$\sqrt{\frac{\hbar}{2\rho c_s V q}}\frac{e_0}{\epsilon\epsilon_0}h_\iota\left(\theta,\phi\right)G\left(q_0\cos\left(\theta\right)\right)F\left(q_0\sin\left(\theta\right)\right), \tag{5.38}$$

where $F(\mathbf{q}_{\|})$ is given by Eq. 5.24 and $G(q_\perp)$ is given by Eq. 5.29. Following the procedure described in section 5.3.1 results in the general piezoelectric relaxation rate given by:

$$\frac{e_0^2 q_0}{8\pi^2 \rho \hbar c_s^2 \epsilon^2 \epsilon_0^2} \left[N\left(q_0\right)+1\right] \times \\ \int_0^{2\pi} \int_0^{\pi} \left[h_\iota\left(\theta,\phi\right)\right]^2 \left|G\left(q_0 \cos\left(\theta\right)\right) F\left(q_0 \sin\left(\theta\right)\right)\right|^2 \sin\theta d\theta d\phi. \tag{5.39}$$

From Eq. 5.36 and the standard polar coordinate unit vectors [79] we find that h_ι is dependent on the phonon mode and is given by:

$$\begin{aligned} h_{LA} &= 6h_{14} \sin^2\theta \cos\theta \cos\phi \sin\phi, \\ h_{TA_1} &= 2h_{14} \cos\phi \sin\phi \sin\theta \left(3\cos^2\theta - 1\right), \\ h_{TA_2} &= 2h_{14} \sin\theta \cos\theta \left(\cos^2\phi - \sin^2\phi\right). \end{aligned} \tag{5.40}$$

If the relaxation rates for the two transverse modes are added together to give the total TA phonon rate, we find that $[h_\iota(\theta,\phi)]^2$ in expression 5.39 becomes $h_{TA}^2 = h_{TA_1}^2 + h_{TA_2}^2$. Eq. 5.40 can be substituted into this expression which is then integrated over ϕ to give the relaxation rate for transverse acoustic phonons as:

$$\frac{9 e_0^2 q_0 h_{14}^2}{8\pi \rho \hbar c_s^2 \epsilon^2 \epsilon_0^2} \left[N\left(q_0\right)+1\right] \times \\ \int_0^{\pi} \sin^4\theta \cos^2\theta \left|G\left(q_0 \cos\left(\theta\right)\right) F\left(q_0 \sin\left(\theta\right)\right)\right|^2 \sin\theta d\theta. \tag{5.41}$$

Similarly, the relaxation rate for longitudinal acoustic phonons is given by:

$$\frac{e_0^2 q_0 h_{14}^2}{2\pi \rho \hbar c_s^2 \epsilon^2 \epsilon_0^2} \left[N\left(q_0\right)+1\right] \int_0^{\pi} \sin^2\theta \left[\frac{1}{4}\left(3\cos^2\theta - 1\right)^2 + \cos^2\theta\right] \times \\ \left|G\left(q_0 \cos\left(\theta\right)\right) F\left(q_0 \sin\left(\theta\right)\right)\right|^2 \sin\theta d\theta. \tag{5.42}$$

5.3.3 Screening of the Piezoelectric Interaction

Screening of the piezoelectric field might be expected to reduce the electron-phonon coupling and reduce the relaxation rate. We will consider screening of the piezoelectric mechanism following the work of P. A. Maksym [80]. In the Thomas-Fermi approximation, the screening charge has the form $-\kappa_0^2\epsilon\epsilon_0\varphi$ where φ is the piezoelectric potential, $\kappa_0 = 2\pi/l_s$ is the Thomas-Fermi screening wave vector where $l_s = 10$nm is the screening length and ϵ is the relative dielectric constant. The Thomas-Fermi screening wave vector and the relative dielectric constant are functions of z because layers of different materials are used to construct the pillar dot considered here. In order to take screening into account, we must solve Poisson's equation as we did in section 5.3 but with the screening term included:

$$-\nabla \cdot (\epsilon\epsilon_0\nabla\varphi) + \kappa_0^2\epsilon\epsilon_0\varphi = -\nabla \cdot \mathbf{P}. \tag{5.43}$$

We expect this equation to have solutions of the form:

$$\varphi = \sum_{q_\parallel} \phi_{q_\parallel}(z)\exp\left(i\mathbf{q}_\parallel \cdot \mathbf{r}\right) + \phi^*_{q_\parallel}(z)\exp\left(-i\mathbf{q}_\parallel \cdot \mathbf{r}\right). \tag{5.44}$$

The piezoelectric interaction Hamiltonian for the emission of a phonon can be found by solving the Poisson equation with the electrostatic Green's function $g_{q_\parallel}$ which satisfies:

$$-\frac{d}{dz}\left(\epsilon\epsilon_0\frac{d}{dz}g_{q_\parallel}\right) + \epsilon\epsilon_0\left(q_\parallel^2 + \kappa_0^2\right)g_{q_\parallel} = \delta\left(z - z'\right). \tag{5.45}$$

Once the interaction Hamiltonian has been found, we use it to find the matrix element that appears in the Golden Rule in a similar way to that presented in section 5.3.2. The resulting expression for the transition rate is similar to that in expressions 5.39 and 5.42 except that the function $G(q_\perp)$ is replaced by:

$$\epsilon\epsilon_0 q^2 \int\int Z^2(z)\, g_{q_\parallel}(z - z')\exp\left(iq_\perp z'\right)dz'dz \tag{5.46}$$

where ϵ is the dielectric constant of the quantum well layer and $Z(z)$ is the ground state wave function of the finite well. The integrals are performed numerically by a subroutine provided by P. A. Maksym [70].

5.4 The Deformation Potential Relaxation Rate

In this section we present the phonon relaxation rates for transitions mediated by the deformation potential. Our results are obtained with the method detailed in section 5.3.1. The relaxation rate is dependent on the difference in energy between the initial and final states, so in order to understand some of the results in this section and section 5.5, we must refer to the energy spectrum of those states and especially the location of the (anti) crossing points.

We find that the finite well confinement of the electrostatic model leads to oscillations in the relaxation rates as a function of magnetic field. We investigate this by using a quasi-two dimensional model, comparing the results to the full three dimensional system. We then present results for a system where dot electrons interact via the Coulomb potential but there is no spin-orbit coupling, before finally presenting the results for the spin flip relaxation rate.

5.4.1 Non-Interacting System

First we will present the relaxation rates for a non-interacting quantum dot where the Dresselhaus spin orbit mixing is neglected.

In calculating the phonon relaxation rate for electrostatic quantum dots, we have considered the perpendicular confinement in two ways. First, the confinement is modelled as a rectangular finite well. The second is a quasi-2D model where we assume that the matrix element in Eq. 5.25 can be approximated as unity. In figure 5.8, the quasi-2D and 3D models are compared for deformation potential acoustic phonon relaxation from state 7 ($L = 1$, $S = S_z = 0$) to the ground state ($L = 0$, $S = S_z = 0$) corresponding to the energy spectrum shown in figure 5.2. The 3D model is found to give rise to an oscillation in the relaxation

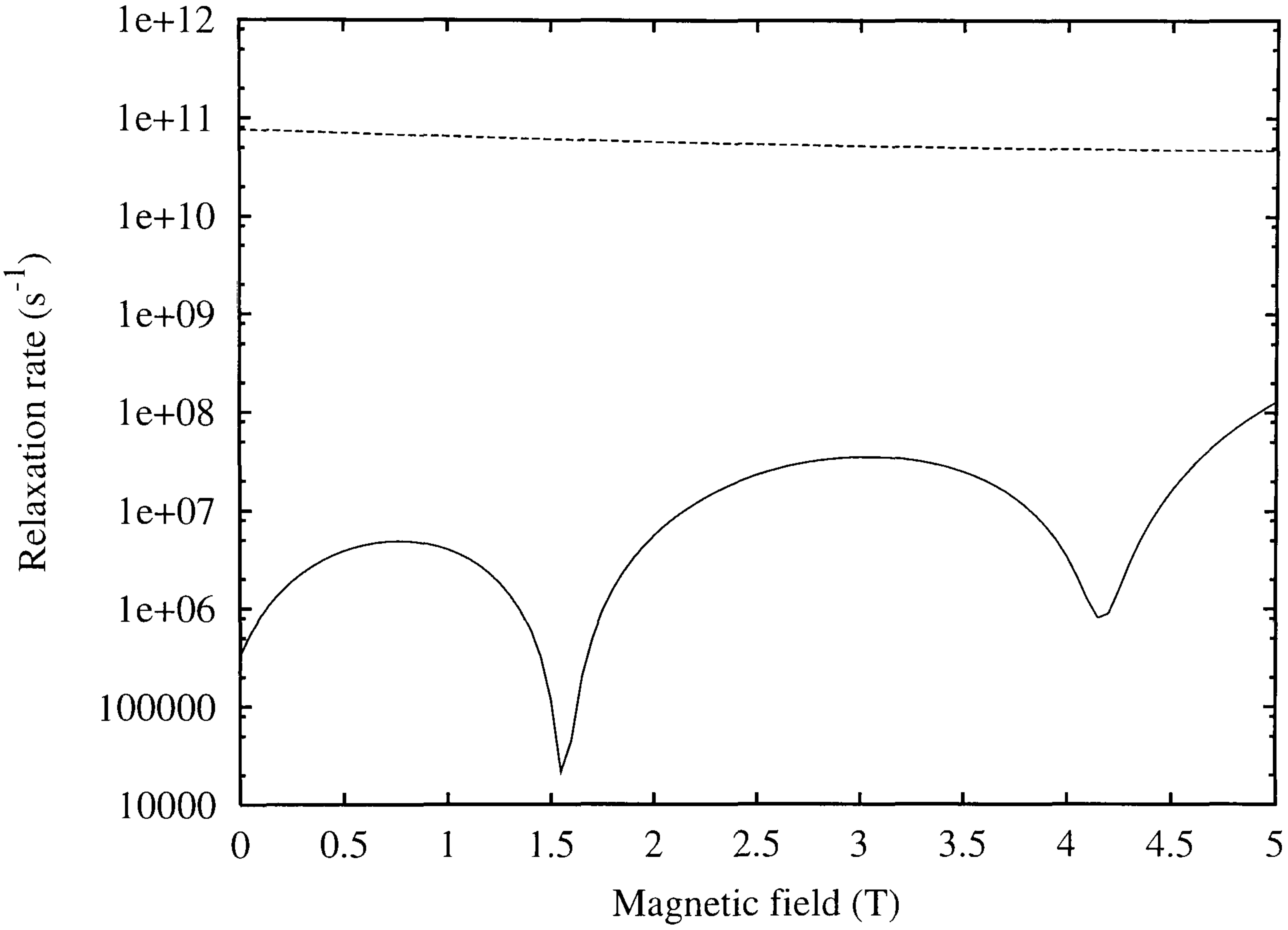

Figure 5.8: The relaxation rate for transition without a spin flip from state 7 ($L = 1$, $S = S_z = 0$) to the ground state ($L = 0$, $S = S_z = 0$) as a function of perpendicular external magnetic field (B_z) for a two-particle non-interacting electrostatic quantum dot. Phonon coupling is via the deformation potential. Lateral confinement energy is 5meV. The dotted line shows the quasi-2D model where it is assumed that the matrix element in Eq. 5.25 can be approximated as unity. The solid line shows the oscillations attributed to the perpendicular finite well confinement. Rates are calculated for a temperature of 1K.

rate. To explain these oscillations we consider $G(q_\perp)$ (Eq. 5.31) in the limit where the potential well depth $V_0 \to \infty$. $G(q_\perp)$ is then given by:

$$\frac{1}{w}\int_{-w}^{w} \cos^2\left(\frac{\pi z}{2w}\right) \exp\left(iq_\perp z\right) dz = \frac{\sin(q_\perp w)}{q_\perp w}\left[1 - \frac{q_\perp^2 w^2}{q_\perp^2 w^2 - \pi^2}\right] \tag{5.47}$$

where w is the well half width. This is the same result as given by U. Bockelmann [51]. This function vanishes when $|q_\perp w| = n\pi$ where $n = 2, 3, 4, \ldots$.

To explain the oscillation in the relaxation rate it will be useful to deduce the direction in which the phonon is emitted. We do this by considering the single particle matrix element for transitions from the $l = \pm 1$ excited state to the $l = 0$ ground state of Eq. 2.1. By differentiating this matrix element with respect to $q_\|$, we find that the peak value occurs when $\lambda q_\| = \sqrt{2}$ where λ is the length parameter of the Fock-Darwin states given by Eq. 2.2. From conservation of energy, we also know that $q\hbar c_s = \Delta_E$ and can therefore deduce that for a transition of sufficiently large energy, $q_\perp = \hbar^{-1}(\Delta_E^2 c_s^{-2} - 2m^*\Delta_E)^{\frac{1}{2}} \approx \Delta_E[\hbar c_s]^{-1}$. This suggests that the phonon is emitted close to the z direction in agreement with Khaetskii *et al.* [25].

The $q_\|$ dependent factor of the integrand, $F(q_\|)$ in expression 5.28, takes the form of a Gaussian multiplied by a polynomial because of the Fock-Darwin wave functions used in this calculation. The position and width of the peak in this Gaussian effectively picks out the small range where the integrand in expression 5.28 is significant. If the peak position on the Gaussian in $F(q_0 \sin\theta)$ coincides with a minimum in $G(q_0 \cos\theta)$, the relaxation rate will be suppressed. Conversely, if the peak of the Gaussian in $F(q_0 \sin\theta)$ coincides with a maximum in $G(q_0 \cos\theta)$, then the relaxation rate will be large.

From this simplified model we can see that the finite perpendicular confinement of the system is clearly responsible for the oscillations in the relaxation rate. We

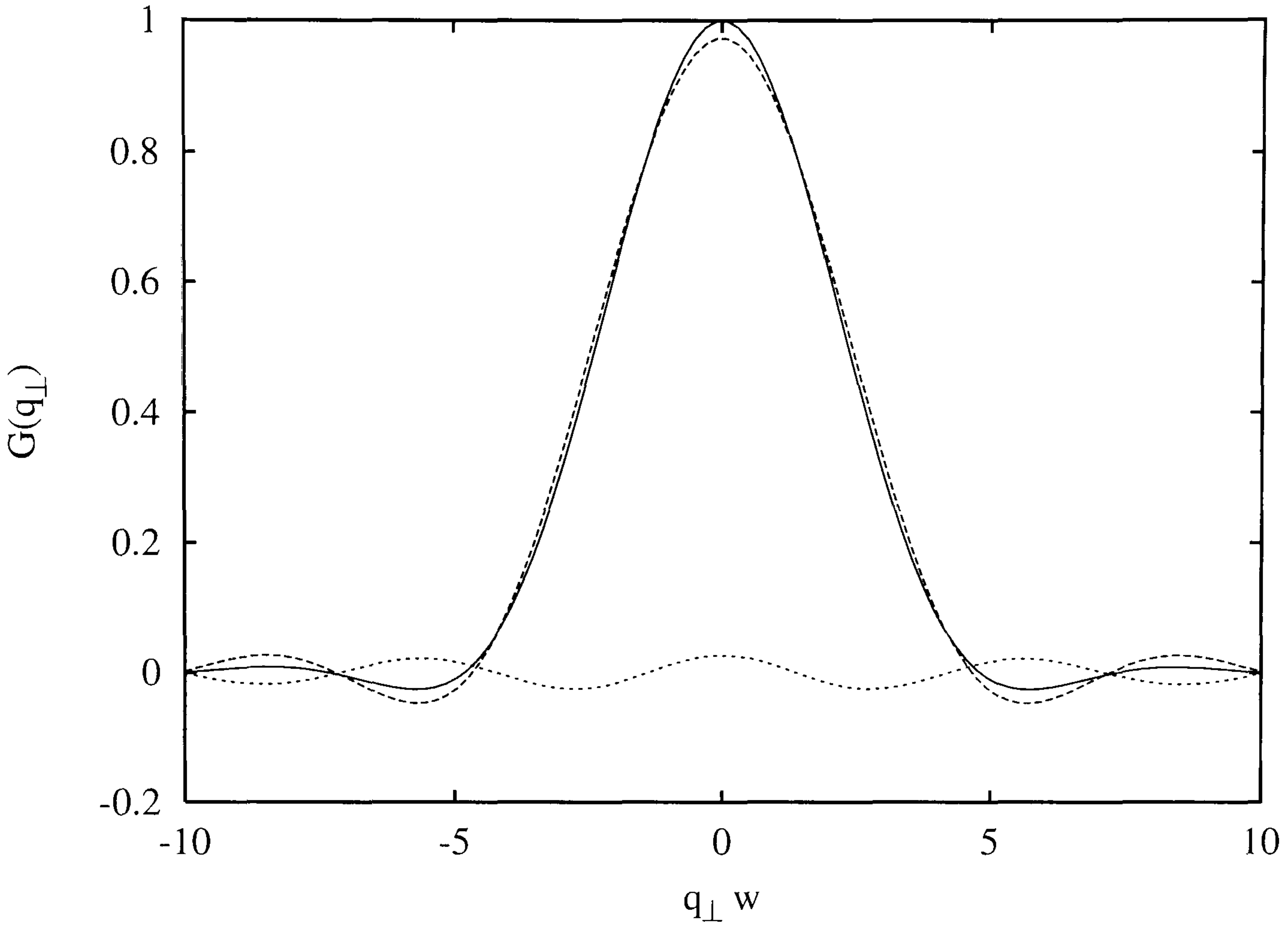

Figure 5.9: The perpendicular component of the matrix element given by Eq. 5.31 against the dimensionless $q_\perp$ for the parameters used in figure 5.8. The solid line is the sum of both terms in Eq. 5.31, the fine dotted line is the first term and the coarse dotted line the second term in Eq. 5.31.

now return to the real $G(q_\perp)$ given by Eq. 5.31. If we were to set the RHS of Eq. 5.31 equal to zero we could locate the values of $q_\perp$ for which this expression vanishes. Unfortunately it is impossible to solve the resulting equation in terms of elementary functions, but we can locate the zeros graphically. Figure 5.9 shows the complete function (solid line), the first term (fine dotted line) and the second term (course dotted line) for the parameters used in figure 5.2. To a first approximation, the assumption that the first term can be neglected would seem to be confirmed at least for the parameters discussed in this work.

5.4.2 Spin-Mixed System

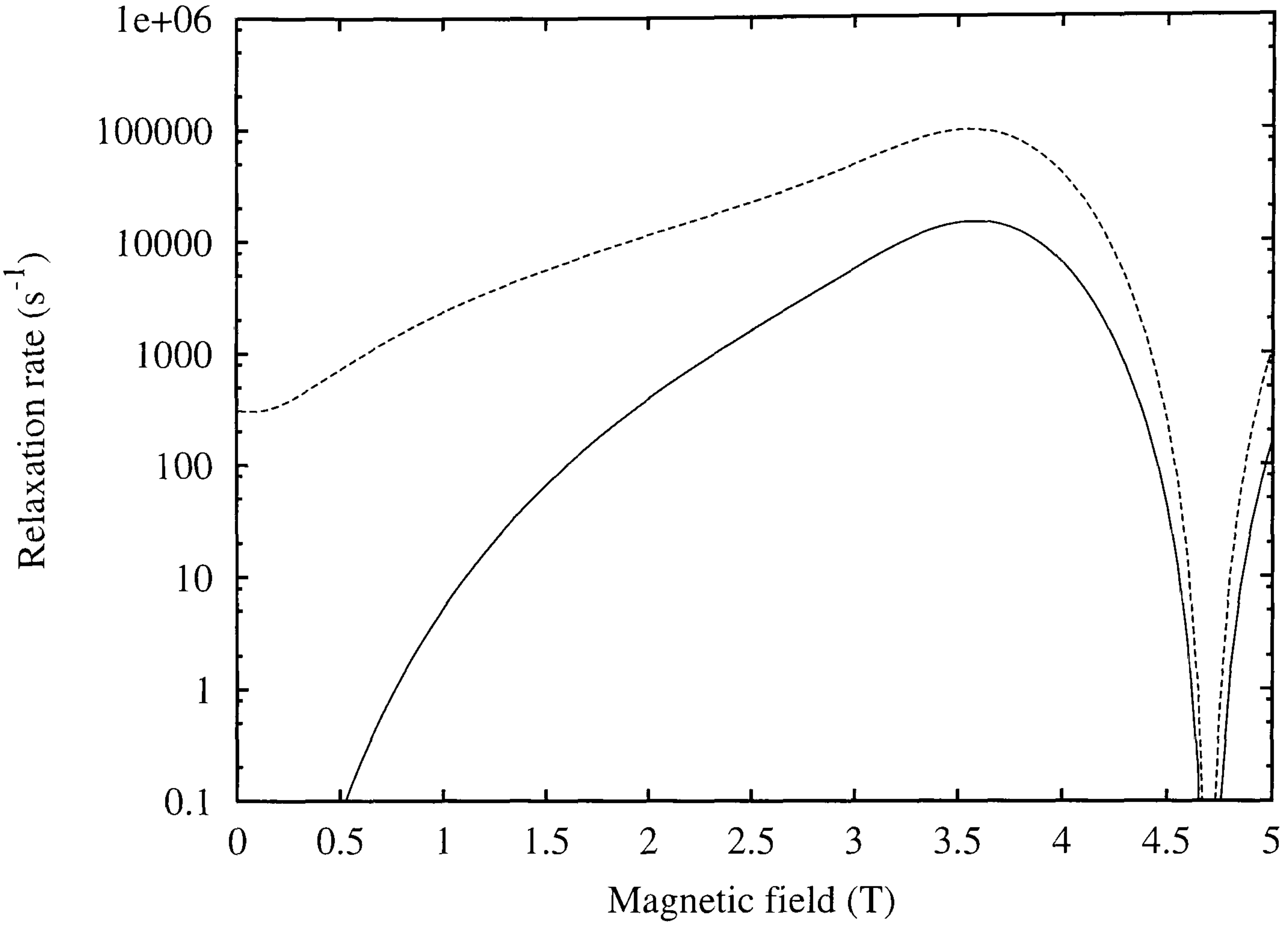

Figure 5.10: Relaxation rates for 3D (solid line) and quasi-2D (dotted line) dots including the Coulomb interaction between dot electrons. Transitions involve spin flip scattering between state 3 and the ground state as given in table 5.1 with energy levels shown in figure 5.3.

We now include the Coulomb interaction between the dot electrons and the Dresselhaus spin-orbit mixing term given by Eq. 5.3. This corresponds to the energy level diagram given in figure 5.3. We consider spin flip relaxation from state 3 to the ground state as defined using quasi-quantum numbers and table 5.1. The relaxation rate for this transition is shown in figure 5.10 for the 3D electrostatic dot (solid line) and the quasi-2D dot (coarse dotted line). The suppression of the relaxation rate due to the finite well z confinement of the 3D model is clearly visible at $B < 0.5$T (compare the 2D and 3D results). At

$B \approx 4.7$T the rate falls dramatically. This is due to the anti-crossing of the ground and excited state energy levels shown in figure 5.3.

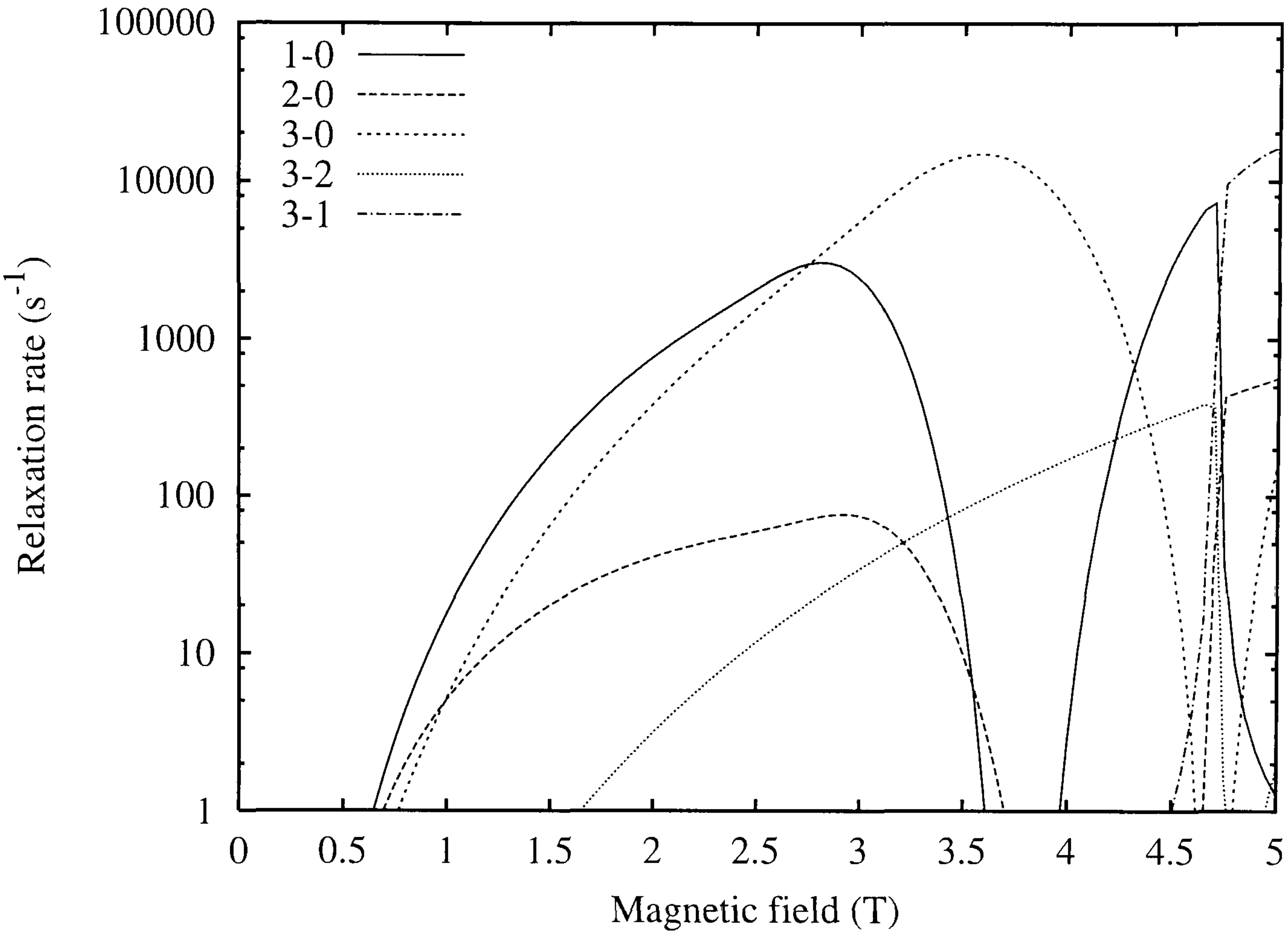

Figure 5.11: Relaxation rate against magnetic field for transitions requiring a spin flip. The key denotes transitions from the higher numbered state to the lower numbered state for the 3D model using quasi-quantum numbers as defined in table 5.1. The relaxation rate 2-1 is indistinguishable from the relaxation rate from 3-2 and has been omitted.

The spin flip relaxation rates for several transitions are shown in figure 5.11 where the labels given in the key refer to the state numbers given in table 5.1. The suppression of all the relaxation rates due to the finite well confinement is again visible at $B < 0.5$T although the exact magnetic field at which the minimum occurs varies for each transition because the energy difference depends on the states involved. At higher magnetic fields ($B = 3.5 - 4.2$T), the energy levels for states 1 and 0 given in figure 5.3 cross at $B = 3.75$T and the relaxation rate goes through a minimum.

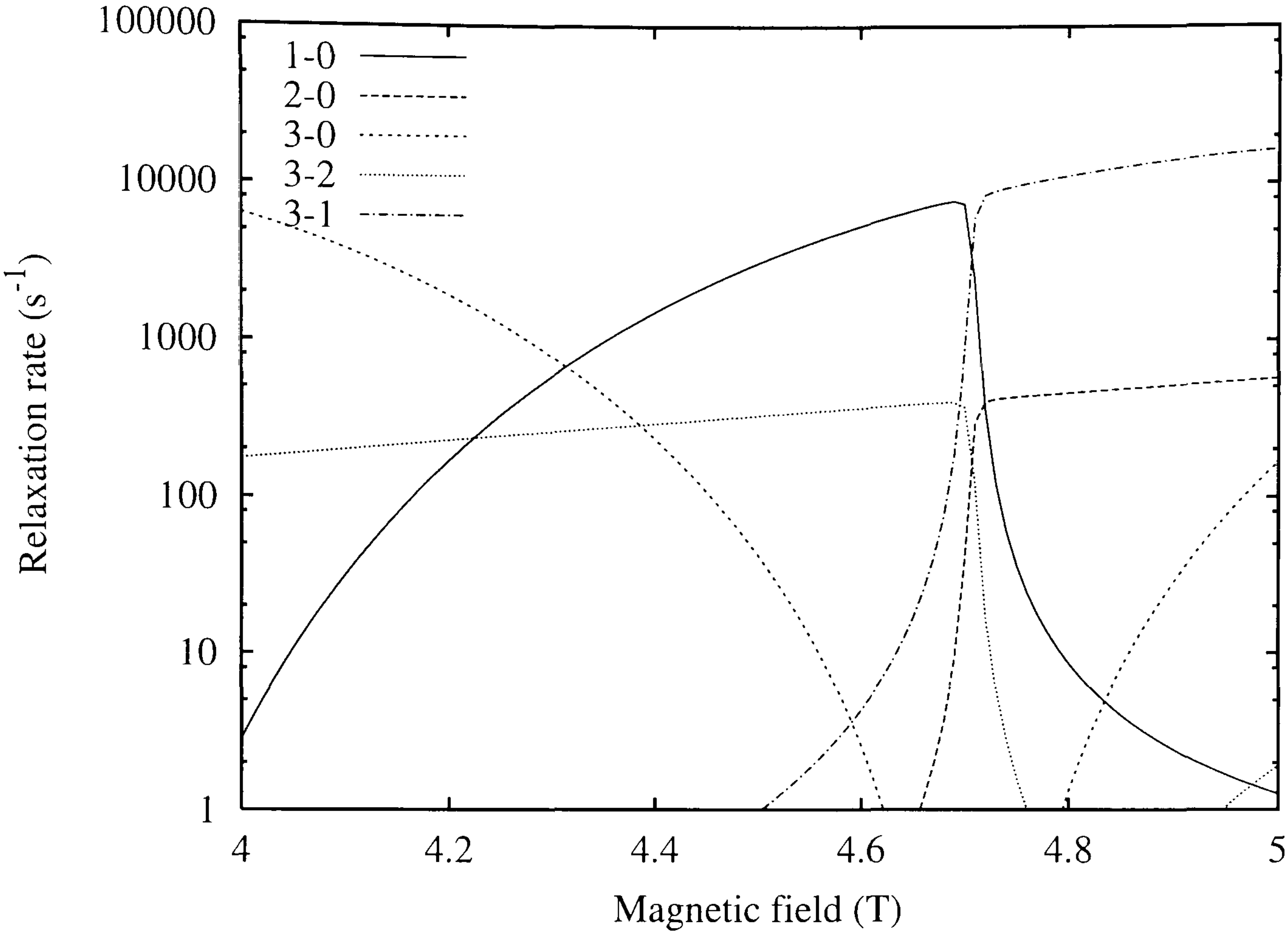

Figure 5.12: A close up of the spin flip relaxation rate presented in figure 5.11 for a magnetic field of between 4 and 5 T. The key denotes transitions from the higher numbered state to the lower numbered state for the 3D model. Quasi-quantum numbers are defined in table 5.1.

The anti-crossing manifests itself at $B \approx 4.7$T and results in some complicated behaviour in the relaxation rates. A closer view of this behaviour is shown in figure 5.12. As we have seen, the energy levels of states 3 and 0 exhibit an anti-crossing at $B = 4.7$T but the quasi-quantum numbers behave as though there was a crossing. This means that the quasi-quantum numbers for states 3 and 0 effectively swap over at the magnetic field corresponding to the anti-crossing. The swapping of the quasi-quantum numbers does not affect the relaxation rate from state 3 to state 0 which displays a strong reduction in the rate caused by the reduction in the size of the energy gap. However, for transitions involving only one of those states, the abrupt change in the quasi-quantum numbers causes the relaxation rates to also change abruptly. For example at $B = 4.7$T, state 3 takes on the quasi-quantum numbers of state 0 and *vice versa.* The transition rate from state 3 to state 2 (fine dotted line in figure 5.12) falls dramatically and the transition rate from state 2 to state 0 (course dotted line) increases just as dramatically as the energy levels pass through the anti-crossing.

We now consider the route by which an excited electron can relax. Relaxation from state 1 to the ground state must be direct since there are no intermediate states to occupy. Relaxation from state 3 to the ground state is found to be relatively fast suggesting that this may also be a direct transition. The relaxation rate from state 2 to state 0 becomes slower than the state 2 to state 1 relaxation rate at $B \approx 3.2$T. Below this field the transition may also be direct, but above this field a direct transition may no longer preferable. Instead, it may be favourable for a cascade transition via state 1 before relaxing to the ground state. However, above $B = 3.55$T, relaxation from state 1 to state 0 is strongly suppressed. We are then in the situation where a transition to state 1 is faster than the direct transition to state 0, but transition from state 1 to state 0 is slow. This could feasibly cause the electron to become "lodged" in state 1, where further relaxation would be slow.

We now return to further examine the oscillations due to the finite well confinement and especially the effect of increasing the width of the dot. In their abstract from the Quantum Dot 2004 Conference in Banff, Canada, A. Bertoni *et al.* [81] present results showing oscillations in the magnetic field dependent relaxation rate for two vertically coupled quantum dots. They also comment that this effect is not found in a single quantum dot and cite U. Bockelmann [51]

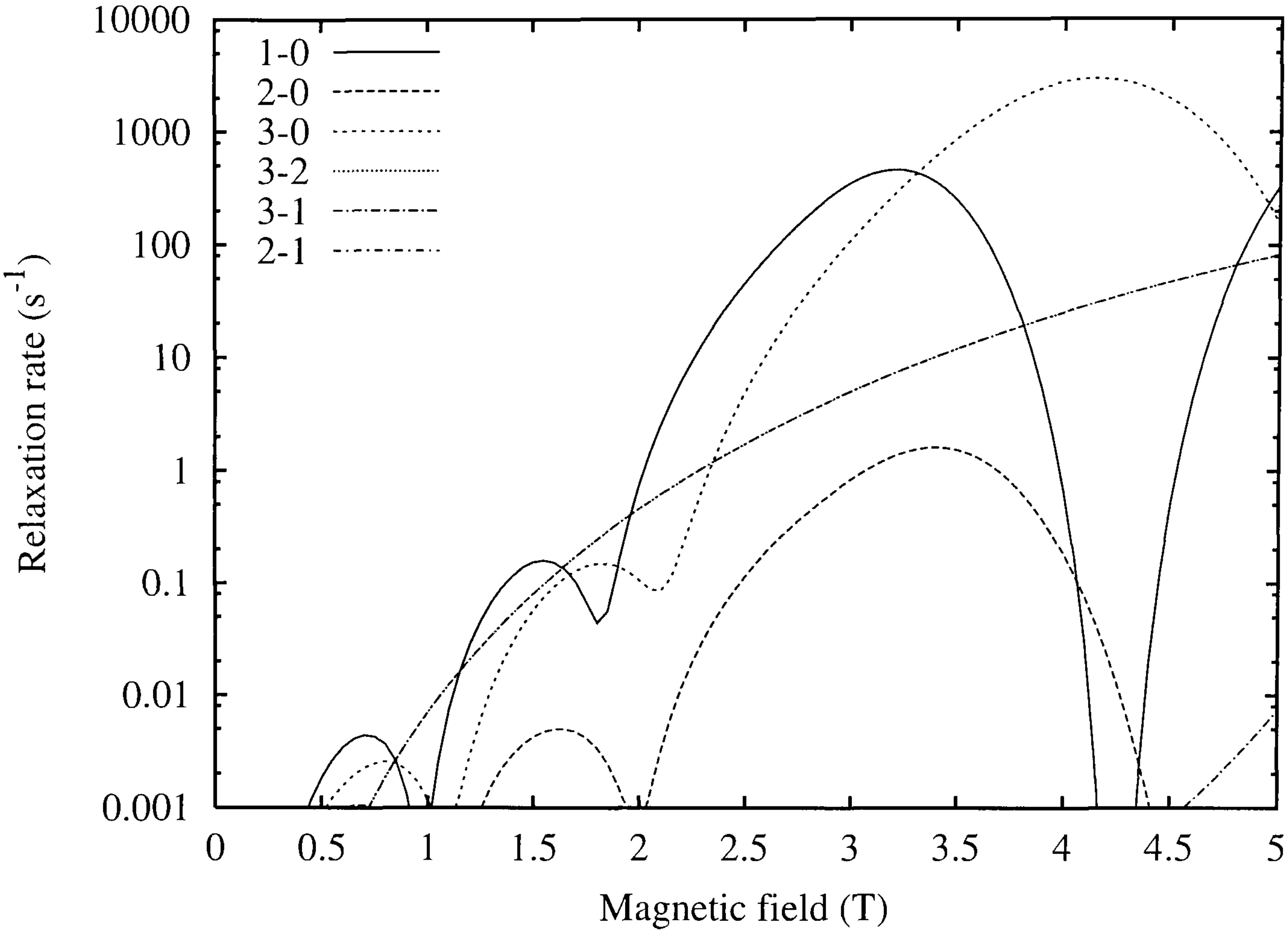

Figure 5.13: Relaxation rate against magnetic field for transitions requiring a spin flip for a wide dot. Transitions as given in the key from the higher numbered state to the lower numbered state for the 3D model. Quasi-quantum numbers are given in table 5.1.

as the justification for this comment. This is a surprising statement considering that Bockelmann's relaxation rate contains the factor $\sin(x)/[x - x^3/\pi^2]$ and we have already shown this causes oscillations in the relaxation rate (section 5.4.1, Eq. 5.47). Bertoni *et al.* suggest that the oscillations in the relaxation rate are an effect found only in coupled quantum dots. In fact we have shown that this effect *is* found in single dots and is caused by the perpendicular finite well confinement. We have also found that this effect can be manipulated by changing the applied magnetic field and the dot thickness.

Figure 5.13 shows the spin flip relaxation rates given previously in figure 5.11 except that instead of the 12nm thick dot used in figure 5.11, the thickness is doubled to 24nm. The oscillations which arise from the finite well confinement (see expression 5.29) are clearly visible at $B < 2.5\text{T}$. This shows that the oscillations found in the relaxation rate are a single dot effect that can be manipulated by altering both the applied magnetic field and the thickness of the heterostructure used to manufacture the quantum dot. This result will be of benefit in quantum computing applications where a slow relaxation rate is required.

5.5 The Piezoelectric Potential Relaxation Rate

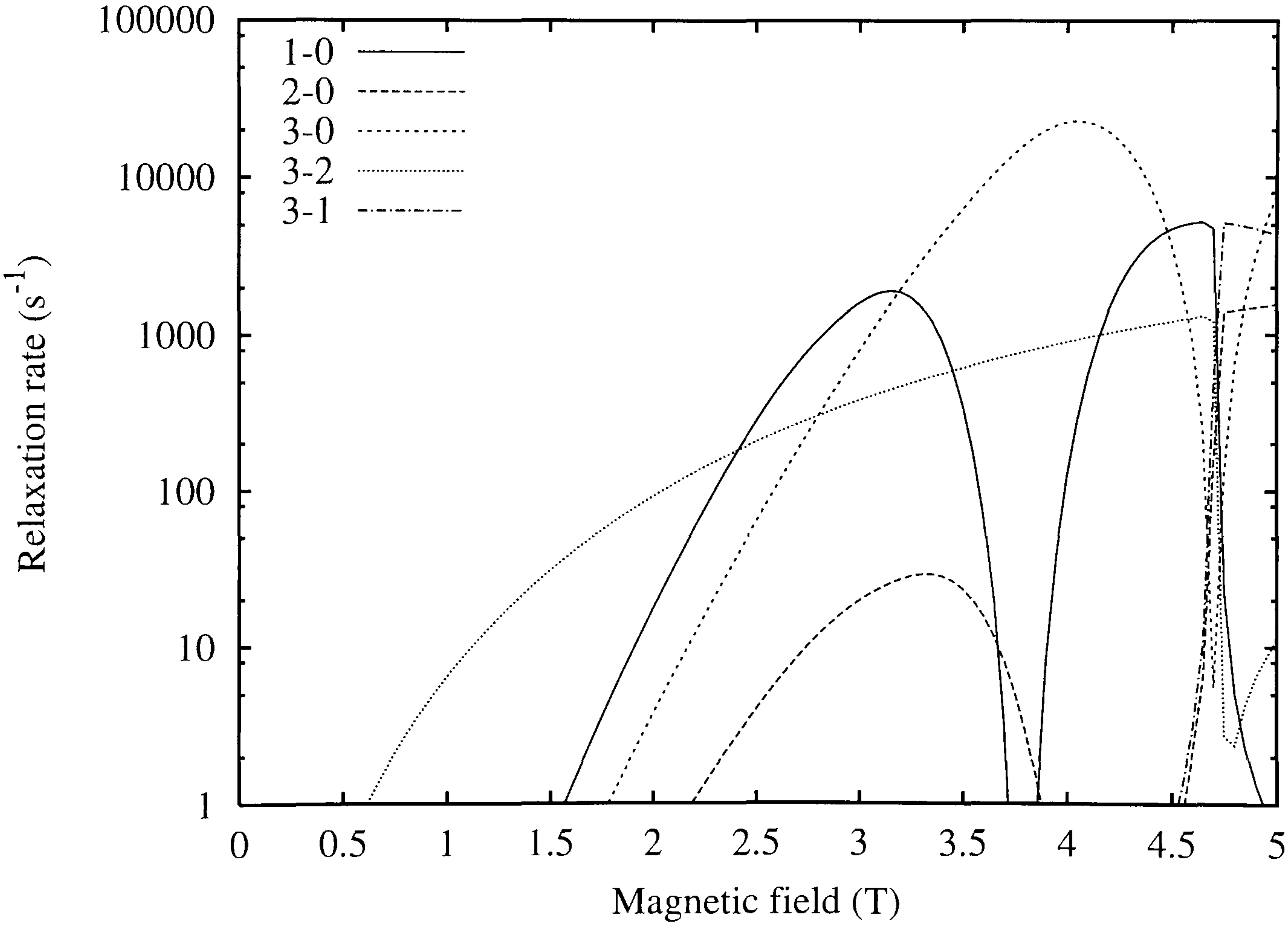

Figure 5.14: The total unscreened piezoelectric relaxation rate against magnetic field for transitions requiring a spin flip. Transitions as given in the key from the higher numbered state to the lower numbered state. Quasi-quantum numbers are given in table 5.1.

We now turn our attention to the piezoelectric scattering mechanism discussed in section 5.3.2. Figure 5.14 shows the unscreened piezoelectric relaxation rate for transitions requiring a spin flip from the sub-levels of the $S \approx 1$, $L \approx 1$ triplet state. The relaxation rates for these transitions were previously presented for deformation potential phonon scattering in figure 5.11. In transitions from the triplet state to the singlet ground state, the piezoelectric relaxation rate dominates over the deformation rate only at points where the energy difference between initial and final states is close to a crossing point and therefore small (less than ≈ 0.75meV). For the transition from state 1 to state 0, this occurs between $B \approx 3.5$T and $B \approx 4$T, for transitions from state 3 to state 0, the range is $B \approx 4$T to $B \approx 5$T. The transitions between triplet sub-levels which require only 1 electron to complete a spin flip (states 3 to 2 and states 2 to 1) are dominated by the piezoelectric mechanism, again the energy difference between the initial and final states is small. The relaxation rates for transitions between states 3 and 1 (where both electrons make a spin flip, see table 5.1) are negligible for both mechanisms except close to the anti-crossing where the piezoelectric potential rate is dominant. The dominance of the deformation rate at larger energy gaps can be explained by its q_0^3 dependence whereas the piezoelectric rate has only a linear q_0 dependence.

Figure 5.15 shows the total screened piezoelectric relaxation rate (see section 5.3.1). The addition of screening to the piezoelectric electron-phonon coupling mechanism has the effect of lowering all of the piezoelectric relaxation rates slightly. The transitions between triplet sub-levels which require only 1 electron to complete a spin flip (states 3 to 2 and states 2 to 1) are again the only transitions that are dominated by the piezoelectric mechanism.

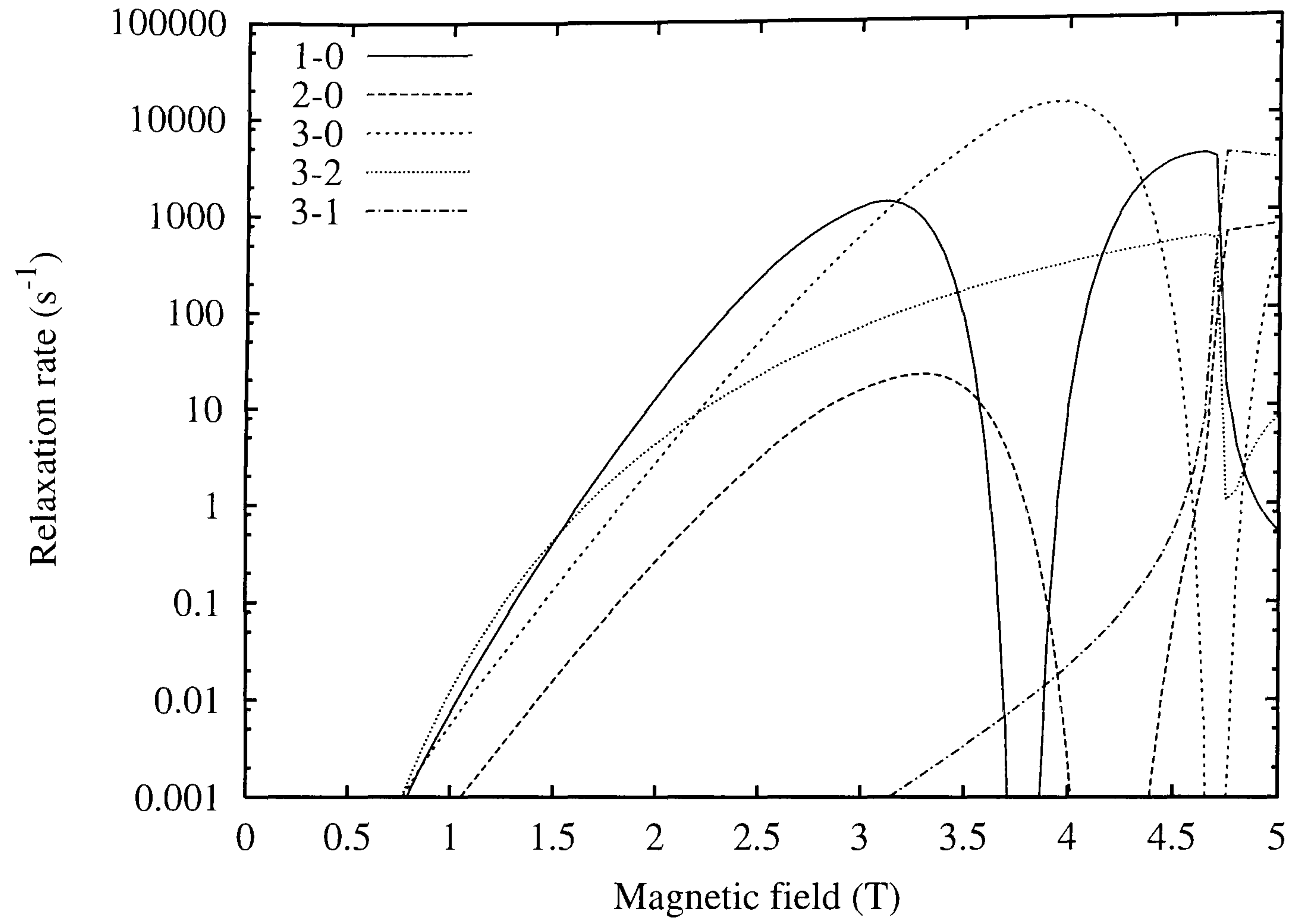

Figure 5.15: The total screened piezoelectric relaxation rate against magnetic field for transitions requiring a spin flip. Transitions as given in the key from the higher numbered state to the lower numbered state. Quasi-quantum numbers are given in table 5.1.

5.6 The Total Relaxation Rate

Figure 5.16 shows the total relaxation rate for both deformation and screened piezoelectric potentials plotted against magnetic field. The matrix elements of the deformation potential (expression 5.23) and the piezoelectric potential (expression 5.38) are shifted in phase by $\pi/2$. Therefore, the two scattering mechanisms do not "interfere" with each other and can be treated as independent mechanisms. The square magnitude of the matrix elements can be added together thus $|M_T|^2 = |M_D|^2 + |M_P|^2$ (where M_T is the total, M_D is the deformation potential and M_P is the piezoelectric potential). Comparing figure 5.16 with

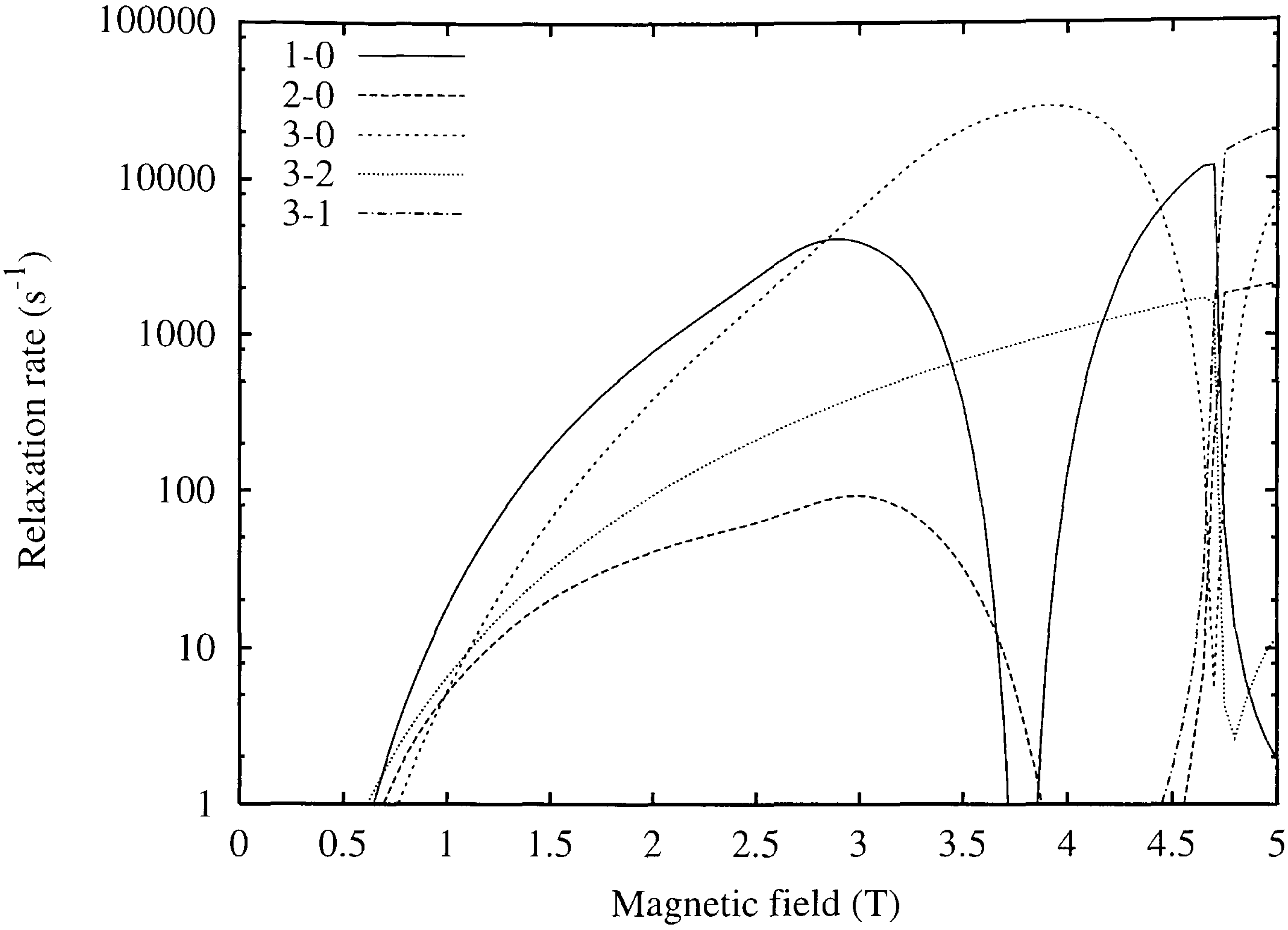

Figure 5.16: The total relaxation rate for deformation and piezoelectric potentials against magnetic field for transitions requiring a spin flip. Transitions as given in the key from the higher numbered state to the lower numbered state. Quasi-quantum numbers are given in table 5.1.

figure 5.11, we see that the the piezoelectric relaxation rate only adds significantly to the total relaxation rate where the energy difference between initial and final states is less than about 0.75meV.

5.7 Comparison with Previous work

We will now consider some of the previous work in this area. In their calculation of piezoelectric-phonon relaxation rates in quantum dots, A. V. Khaetskii and Y. V. Nazarov [25, 26] make the approximation that $q_\perp \gg q_\parallel$ so that $q \approx q_\perp$. This enables the piezoelectric anisotropy factor for transverse acoustic phonons (see Eq. 5.40) to be approximated as $4h_{14}^2 q_{\|}^2/q_{\perp}^2$. The anisotropy factor and the factor of q^{-1} arising from the piezoelectric Hamiltonian (expression 5.35) lead to a divergent integral over the phonon wave vector $q_{\|}$. At this point Khaetskii *et al.* also appear to have neglected the possibility of the phonon being emitted in both positive and negative $q_{\perp}$ directions so the relaxation rate is underestimated by a factor of 2. The divergence in the $q_{\|}$ integral is only lifted by approximating the q^{-1} factor as $q_{\perp}^{-1}$. This second approximation also has an effect on the limits of the $q_{\|}$ integral such that the range is changed from $0 \leq q_{\|} \leq q_0$ to $0 \leq q_{\|} \leq \infty$ or in other words, $q_{\|}$ is integrated over values that exceed the maximum allowed by energy conservation. This approximation will be acceptable provided the Fourier transform of the QD wave function decays sufficiently quickly.

S. Dickman, P. Hawrylak [67] and M. Florescu *et al.* [68] (members of the same group) published spin flip relaxation rate studies in a two-electron quantum dot as this work was being completed. These authors chose to use a highly truncated basis set which does not appear to give converged energy eigenvalues or quantum states (see section 5.1) and as such, the relaxation rates are unlikely to be accurate. Comparing the relaxation times/rates given in [67] and [68] we find that the two papers are inconsistent. Florescu *et al.* [68] gives a maximum in the relaxation rate at the singlet-triplet transition whereas Dickman [67] gives a minimum. The matrix element goes as $< F|\exp(i\mathbf{q}\cdot\mathbf{r})|I >$ where $\mathbf{q}$ depends on the energy difference (ΔE) between initial (I) and final (F) states. As $\Delta E \rightarrow 0$ at the singlet triplet transition, the matrix element must vanish by orthogonality if $F \neq I$ and we should observe a minimum as described by Dickman [67].

Spin flip relaxation processes in electrostatic quantum dots have been studied experimentally by T. Fujisawa *et al.* [19, 20, 21] (see figure 5.1). Fujisawa *et al.*

used asymmetric tunnelling barriers so that tunnelling into the dot (through the thin lower barrier with time constant Γ_s) is much faster than the tunnelling out of the dot (through the thick upper barrier with time constant Γ_d). A series of pulses is applied to the side gate to allow the Fermi levels of the source (μ_s) and drain (μ_d) to align with the energy levels in the dot. If the low-voltage phase of the pulse is such that the $S \approx 0$ ground state of the dot is aligned with the Fermi energy of the drain contact for a sufficiently long time, the dot will be emptied. A single electron is then allowed to tunnel into the ground state of the dot. The high-voltage phase of the pulse then aligns the $S \approx 1$ excited dot state with the transport window. The asymmetric barriers mean that an electron can tunnel into the dot quickly but out of the dot more slowly. The tunnelling current can be interrupted by the electron in the dot excited state making the transition to the ground state by performing a spin flip before it has time to tunnel out through the drain. The relaxation rate can then be deduced from the average number of electrons tunnelling per pulse.

Whereas the dot considered in this work has circular symmetry and a confinement energy $\hbar\omega_0 = 5$meV, Fujisawa's dot is asymmetric with confinement energies of $\hbar\omega_x = 2.5$meV and $\hbar\omega_y = 5.5$meV. The energy spectrum of Fujisawa's dot has a single particle excitation energy as 2.5meV at $B = 0$T compared with 5meV for the dot considered here. Fujisawa *et al.* report that the singlet-triplet energy crossover occurs at a magnetic field of $B = 2.5$T, although they were unable to resolve individual Zeeman levels in the triplet states [20]. By comparison the energy crossover found in this work occurs at $B \approx 4$T (see figure 5.3). Fujisawa *et al.* report a triplet-singlet relaxation time in two electron dots of 200μs at $B = 0$ and states that the relaxation time shows only weak magnetic field dependence at least over the range $B = 0\text{T}$ ($E_i - E_f \approx 0.6\text{meV}$) to $B = 2\text{T}$ ($E_i - E_f \approx 0.24\text{meV}$) in that it is always longer than about $100\mu\text{s}$. Fujisawa *et al.* attribute the small energy spacing in the two electron quantum dot to be a result of the Coulomb interaction between the two electrons. In the dot considered in this work, the energy spacing between singlet and triplet states is 2.8meV at $B = 0\text{T}$ and 1.2meV at $B = 2\text{T}$.

Since the dot considered by Fujisawa *et al.* does not closely match the dot considered above, we cannot make a direct comparison. However, we can compare the range of energy gaps considered by Fujisawa *et al.* ($0.24 - 0.6\text{meV}$) with a comparable range of energy gaps in the work above (corresponding to $B = 3.3 - 3.65\text{T}$ in figures 5.3 and 5.11), if we assume that the matrix elements are similar. In this case, we find a relaxation time of $50 - 100\mu\text{s}$ which appears to be only weakly dependent on magnetic field and in tentative agreement with the work of Fujisawa *et al.*

5.8 Conclusions

We have studied the effects of the Coulomb interaction and the Dresselhaus spin-orbit coupling mechanism on the energy levels and phonon-assisted relaxation rates in electrostatic quantum dots. The inclusion of the Dresselhaus term removes spin as a good quantum number and therefore makes spin flip transitions possible. The spin-orbit mixing introduced by the Dresselhaus mechanism also results in the emergence of anti-crossings in the energy spectrum. These anti-crossings result from the coupling of the energy levels by the off diagonal spin-orbit mixing matrix elements. The block diagonal structure of the matrix can be linked to the commutator relation $[\hat{l}_z - \hat{s}_z, (\sigma_y p_y - \sigma_x p_x)p_z^2] = 0$. This commutator relation is found to be valid for the linear Dresselhaus spin-orbit interaction but breaks down if the cubic Dresselhaus terms are included.

Two mechanisms for electron-phonon coupling have been considered. The first is the deformation potential due to the band bending caused by the emitted phonon. The deformation potential is found to be dominant for transitions of larger energy due to the q_0^3 dependence of the relaxation rate. The second mechanism for electron-phonon coupling is the piezoelectric effect due to the strain produced by the emitted phonon. The piezoelectric rate has a linear dependence on q_0 and is dominant only for transitions between states of small energy difference.

For transitions that require a spin flip, the Coulomb interaction increases the energy of the $S \approx 1$ states less than it does for the $S \approx 0$ states. As a result, the energy difference between the initial $S \approx 1$ and final $S \approx 0$ states ($\Delta E = \hbar c_s q_0$) which affects the relaxation rate, is smaller than for transitions where spin is polarised. In addition to this, the mixing of spin states is a small effect that results in a small matrix element. The small mixing of spin states is the primary reason why transitions that require a spin flip are slow.

The matrix element needed to calculate the relaxation rate oscillates with magnetic field. This is due to the finite well confinement of the heterostructure, from which the dot is fabricated. These oscillations lead to a strong reduction in the relaxation rates at certain magnetic fields. The minima in the relaxation rate can be located by adjusting the applied magnetic field and during the dot manufacturing process by altering the thickness of the heterostructure.

In calculating the spin flip relaxation rates in an electrostatic quantum dot, we have highlighted the existence of minima in the relaxation rate. We have also found that this does not require two coupled dots in contrast to the results of A. Bertoni *et al.*[81]. The well thickness and the applied magnetic field are found to affect the relaxation rate and this will be particularly useful for applications such as quantum computing, where a low relaxation rate is necessary.

In this work we have considered only the Dresselhaus spin-orbit coupling mechanism and found the existence of oscillations in the relaxation rate. These oscillations do not depend on the spin of the dot states, the only requirement is that the matrix element in the Golden rule has the form of the Fourier transform of finite (or infinite) well wave functions. We therefore expect these oscillations to appear for any system where spin-orbit coupling is due to the admixture of different spin states and where phonon emission provides only energy conservation. Systems where the phonon couples directly to the electron spin are thought to display extremely low relaxation rates ($10^{-1} - 10^{1}\text{s}^{-1}$) [25] but it is unknown if these systems will exhibit similar relaxation rate oscillations.

Chapter 6

Summary and Conclusions

The analysis undertaken during the course of this work has led to the discovery of some new and interesting physics relating to relaxation processes in semiconductor quantum dots. We have concentrated our discussion on two types of quantum dot in which the dominant relaxation mechanisms are markedly different. The first, considered in chapters 3 and 4, is the self-assembled quantum dot in which the dominant relaxation mechanism is thought to be Auger scattering. The second considered in chapter 5 is the electrostatic dot in which the dominant relaxation mechanism is thought to be phonon emission. In studying these two different systems, we have investigated the mechanisms responsible for the relaxation process and examined the parameters that may be used to influence the relaxation rate. We believe our work will serve as a basis for future work in this field.

The work presented in chapter 3 is concerned with Auger relaxation in single particle self-assembled quantum dots and follows on from the work of A. V. Uskov *et al.* [9]. Uskov *et al.* considered only the scattering of dot electrons with electrons located in the two-dimensional wetting layer. In this work we have considered scattering of the dot electrons with electrons located in both the wetting layer and the surrounding bulk material. We find that for the parameters considered here, the bulk scattering rate is dominant by over 2 orders of magnitude due to the relative electron densities of the wetting layer and the bulk material. However, it must be stated that the parameters used will have an effect on the magnitudes of these rates. Electron densities are calculated based on rate equations and parameters presented by B. Liu *et al.* [28]. While it is unlikely that any minor changes in the parameters proposed by Liu *et al.* will seriously affect the conclusions drawn here, it is not impossible to conceive of a system where wetting layer scattering may become the dominant relaxation mechanism.

In Ref. [9], A. V. Uskov *et al.* assumed that the Auger relaxation matrix element could be calculated by using the dipole approximation to the Coulomb potential. In chapter 3 we consider the Auger relaxation rate calculated in the dipole approximation and compare this result with the relaxation rate calculated exactly. We find that the relaxation rate calculated in the dipole approximation consistently exceeds the exact relaxation rate by a factor of approximately 3. This is caused by the energy levels of the dot spreading apart as the dot size is reduced (or equivalently as confinement energy is increased) and we find that the dipole approximation is unlikely to be correct for quantum dots of any realistic size. The comparison between the dipole approximation and the exact result is given in section 3.5.1.

In chapter 3 we perform relaxation rate calculations for the truncated pyramid self-assembled quantum dot states calculated by M. Roy *et al.* [17]. We find that the composition gradient in the truncated pyramid dot has only a small affect on the relaxation rate. The composition variation alters the effective mass of the dot electron, affecting the relaxation rate slightly for the bulk scattering mechanism.

For the 2D scattering mechanism, the electrons are confined marginally higher in the graded material dot and further away from the wetting layer thus decreasing the wave function overlap and reducing the relaxation rate. We also calculate the relaxation rates for the harmonic oscillator wave functions given by expression 2.4. Although this model does not accurately predict the relaxation rates of a self-assembled dot, it does provide a relatively simple model with which to examine the physics of the system. The accuracy with which the HO model can predict the relaxation rates for the SAQD models depends heavily on the choice of length parameters used. We have attempted to fit the HO model to the SAQD models by two methods. The first is to match the lateral confinement energy $\hbar\omega$ to the excitation energy and then use the vertical confinement energy $\hbar\omega_z$ to match the ground state energy. The second method is to match the length parameters to the RMS displacement using the relation $\lambda = \sqrt{< r^2 > - < r >^2}$. Although the energy fit method provides the closest fit, both methods are found to consistently underestimate the exact relaxation rate for the pyramidal SAQD models. This is due to the geometry of the HO model not being consistent with real SAQDs. The relaxation rate for the SAQD models when compared to either of the HO models are found to be up to 6 times larger for 3D scattering and up to 3.5 times larger for 2D scattering.

In chapter 4 we consider two electron self-assembled quantum dots. In this system the additional "spectator" electron might be expected to modify the Auger mechanism and therefore affect the relaxation rate. In order to solve the Schrödinger equation for the two particle system we must take into account the Coulomb interaction between the dot electrons. This interaction will be screened by the electrons in the surrounding bulk material.

If the screening length is much smaller than the size of the quantum dot, the two electrons in the quantum dot are approximately non-interacting. As the screening length becomes comparable to the size of the quantum dot, the Coulomb interaction becomes more important. However, the relative strength of the Coulomb interaction is size dependent and to a reasonable approximation, sufficiently small self-assembled dots can be considered only weakly interacting even if the screening length is of the order of the size of the quantum dot. The maximum difference between the relaxation rates calculated with wave functions where the dot electrons are either screened or unscreened from each other is only 3.3% for the SAQDs considered here. The relatively small effect screening has on the relaxation rate suggests that the dot electrons are indeed only weakly interacting and that screening can be neglected with only a small loss of accuracy. This result is particularly useful since taking this screening mechanism into account for all the electron densities considered in this work is found to be extremely computationally expensive.

Comparing the two particle relaxation rates for transitions between states of total spin 0 and those with total spin 1 we find that the spin 0 relaxation rate is larger by a factor of approximately 2. In the case of the spin 0 ground state, the two electrons reside in the lowest energy states and have opposite spins. In the spin 0 excited state, only one electron occupies the lowest energy state. For any of the four terms in the non-interacting two particle matrix element (expression 4.25) to be non-zero, at least one of the electrons in the initial state must occupy the same quantum state as one of the electrons in the final state. In the case of spin 0 relaxation, the double occupancy of the ground state means that two terms are non-zero. In the case of relaxation between states of total spin 1, there is no double occupancy of spatial states and only one term contributes to the matrix element. This is a consequence of the two possible spin orientations and the Pauli exclusion principle. The relatively weak Coulomb interaction between the two dot electrons introduces a small mixing of other states that subsequently appear in the two-particle matrix element. The slight deviation from the factor of 2 in the non-interacting case is a result of this mixing.

In chapter 5 we have focused on a different type of system and investigated phonon-assisted spin-flip relaxation in electrostatic quantum dots. The selection rules on the allowed transitions imposed by conservation of spin will block spin-flip relaxation unless spin can be removed as a good quantum number. After reviewing previous work, we settled on Dresselhaus spin-orbit mixing as the dominant mechanism to achieve this.

The Dresselhaus spin-orbit mixing Hamiltonian can be written as three terms (see Eq. 5.6), the first is linear in the in-plane momentum but proportional to p_z^2, the second term is independent of p_z but cubic in the in-plane momentum and the third term vanishes since $< p_z >= 0$. The confinement in the z direction is restricted over a very much smaller length scale than the in-plane confinement, so the term proportional to p_z^2 will be dominant at the low magnetic fields considered here. For this reason we have neglected the cubic Dresselhaus term.

The Dresselhaus mechanism removes spin as a good quantum number by mixing different spin and angular momentum states and although the effect this has on the magnitude of the energy is relatively small, it does introduce certain anti-crossings in the energy spectrum. This mixing also means that individual states will no longer have a definite spin orientation or angular momentum quantum number. However, we can find the quasi-spin and quasi-angular momentum of the state by calculating the $< S_z >$ and $< L >$ expectation values. Since spin mixing is a very subtle effect, the resulting expectation values are all close to the values gained for the non-spin mixed states, except at certain magnetic fields where an anti-crossing appears in some of the energy levels.

These anti-crossings appear when two of the non-interacting energy levels are coupled by the off diagonal matrix elements of the Dresselhaus Hamiltonian. For the spin-orbit coupling mechanism considered here, $L_z - S_z$ is conserved so that levels with different values of $L_z - S_z$ cross whereas levels with the same value of $L_z - S_z$ anti-cross. We find that the commutator relation (and the two-particle extension, see section 5.2.3) $[\hat{l}_z - \hat{s}_z, (\sigma_y p_y - \sigma_x p_x)p_z^2] = 0$ holds for the linear, in-plane momentum term of the Dresselhaus mechanism but does not hold for the cubic term. This conservation law is relevant to any situation where spin-orbit coupling is considered at fields low enough for the cubic order Dresselhaus terms to be neglected. To the best of our knowledge, this particular result has not been published previously. Interestingly, C. F. Destefani *et al.* [75] report that in InSb dots where spin mixing is strong, the level crossings in the Fock-Darwin energy spectrum that we have found are unaffected by the linear Dresselhaus term, become anti-crossings when the cubic Dresselhaus term is included. These authors comment that the effect is almost imperceptible.

The anti-crossings also result in some complicated behaviour in the relaxation rates (see figure 5.12). States with the same value of $L_z - S_z$ display an anti-crossing in the energy levels but the quasi-quantum numbers behave as though there were a crossing. Since we identify our states by tracking continuous energy levels, the quasi-quantum numbers for states that exhibit an anti-crossing effectively swap over at the magnetic field where the anti-crossing appears. For transitions involving only one of the states involved in the anti-crossing, the abrupt change in the quasi-quantum numbers causes the relaxation rates to also change abruptly.

The perpendicular finite well confinement used in the electrostatic dot model is found to give rise to a magnetic field dependent oscillation in the relaxation rate. The z dependent factor of the matrix element (Eq. 5.31) contains a factor which behaves very approximately as a sinc function with the argument $q_\perp w$, where $q_\perp$ is the perpendicular component of the phonon wave vector and w is the well half-width. The phonon is found to be emitted in a direction approximately perpendicular to the plane of the dot. The well thickness w and the applied magnetic field both affect the factor $G(q_\perp)$ (Eq. 5.31) and may provide a method of manipulating the relaxation rate. In contrast to the result of A. Bertoni *et al.* [81] we find that these oscillations are a consequence of the perpendicular confinement potential and do not only appear in systems where two quantum dots are coupled together.

We have considered two mechanisms for electron-phonon coupling in chapter 5. The first is the deformation potential due to the band bending caused by the emitted phonon. The deformation potential is dominant for the higher energy transitions due to the q_0^3 ($q_0 = \Delta E/\hbar c_s$) dependence of the relaxation rate. The second mechanism for electron-phonon coupling is the piezoelectric field due to the phonon-induced strain. The piezoelectric relaxation rate has a linear dependence in q_0 and is dominant only for transitions where the energy difference between initial and final states is small.

Screening the piezoelectric electron-phonon coupling mechanism lowers all of the piezoelectric relaxation rates slightly. The deformation potential is found to be the dominant relaxation mechanism with the exception of transitions between triplet sub-levels that require only 1 electron complete a spin-flip. These transitions are dominated by the piezoelectric scattering mechanism over the magnetic field range considered here. This is due to the small energy gap between initial and final triplet sub-levels.

6.1 Future Work

There has been a significant amount of interest in the electron spin dynamics of quantum dots recently, due in part to proposals for manipulating the electron spin to form a quantum computer [22, 23, 24]. In chapter 5 of this thesis, we have addressed some of the physics relating to the spin dynamics of a quantum dot system but there remains a substantial amount of work to be done before this system can be said to be completely understood. In chapter 5 we considered the Dresselhaus spin-orbit mixing mechanism but neglected the terms that were cubic in the in-plane momentum. Whilst we believe that this approximation makes little difference to the magnitude of the relaxation rate at least in the magnetic field range considered here, the work of C. F. Destefani *et al.* [75] suggests that the including the neglected terms will lead the emergence of further anti crossings in the energy spectrum. This may lead to more of the complicated behaviour in the relaxation rates described in section 5.4.2.

The electrostatic dot considered in chapter 5 is modeled with a finite well confinement in the perpendicular direction. This confinement potential leads to the emergence of magnetic field dependent oscillations in the spin-flip relaxation rate. We have found that the thickness of the heterostructure affects the oscillations in the relaxation rate. It would be beneficial to calculate the relaxation rate as a function of well thickness since this parameter might be used to manipulate the relaxation rate. These oscillations are found to be unaffected by spin-mixing in systems where the phonon only provides energy conservation during relaxation. However, it is unknown if systems where the phonon couples directly to the electron to provide the spin-flip will also exhibit this feature.

Electron spin resonance spectroscopy (ESR) is a technique similar to nuclear magnetic resonance spectroscopy (NMR) except that it is electron spin instead of nuclear spin that is investigated. The degeneracy of the spin states for an unpaired electron is lifted by the presence of a magnetic field. A resonant microwave signal can then be used to induce transitions between these two spin states. This particular technique can be used to manipulate the spin of an electron in a quantum dot. By applying a suitable microwave signal for a short time, an arbitrary superposition of spin-up and spin-down states can be created. The creation and decoherence time of this superposition is of particular interest due to the potential applications in quantum computing. The prediction of long-lived spin states in this work could be of use in developing such an ESR experiment where the manipulation of spin states is the objective. The $L_z - S_z$ conservation rule found in this work might be of benefit in calculating the decoherence times for a superposition of spin-up and spin-down states created during an ESR experiment. Indeed, the conservation law could be useful in all calculations where SO coupling is taken into account.

Relaxation processes in self-assembled quantum dots has been considered in this and other work, but calculations have been limited to the low lying energy levels. Consequently, very little is known about the relaxation rates of other transitions. Certainly for the more realistic self-assembled dot models this calculation would be difficult to perform due to the complicated form of the wave functions, which require the inclusion of many basis states to achieve converged results. Calculations of this type would be of interest in optoelectronics applications.

To the author's knowledge, spin flip relaxation in self-assembled quantum dots has not been discussed. Since the dominant relaxation mechanisms in self-assembled dots differs from that found in electrostatic dots, we may expect that the relaxation rate will also differ. As far as the author is aware, the efficiency of the Auger relaxation mechanism for spin flip processes in self-assembled dots is unknown. It is also conceivable that longitudinal optic phonons may provide a mechanism capable of mediating spin flip relaxation in self-assembled dots with a suitable energy gap, especially in cases where Auger relaxation is small. However, the complicated form of the self-assembled dot wave functions would pose some significant challenges in calculating the two particle electronic states when spin-orbit mixing is included. The vertical confinement potential in a self-assembled dot is somewhat similar to that of an electrostatic dot in that it has a sharp interface between the dot and the external material. This might suggest that the magnetic field dependent oscillations due to the perpendicular finite well confinement of the electrostatic dot may also appear in self-assembled quantum dots. However, the $\mathrm{In}_x\mathrm{Ga}_{1-x}\mathrm{As}$ self-assembled dot model considered in this work has a composition gradient, which may alter the confinement potential. What effect this may have on any magnetic field dependent oscillations is unknown. Performing spin flip calculations in self-assembled quantum dots would provide an exciting opportunity to further understand these remarkable structures.

APPENDIX A

Glossary of mathematical terms

A glossary of the frequently used mathematical notation in this thesis.

B - Applied magnetic field.

E_n - Energy of the nth state.

$f(k)$ - Boltzmann distribution function for states with wave vector k.

$\mathbf{k}_n$ - Wave vector of the nth state.

κ - Debye screening wave number (see Eq. 3.3).

κ_x - $p_x(p_z^2 - p_y^2)$ and cyclic permutations (see Eq. 5.5).

l, L - Angular momentum quantum number.

λ - Radial length parameter for the HO model (see Eq. 2.2).

λ_z - Vertical length parameter for the HO model.

m^* - Effective mass.

n_p - Injected carrier density.

$\mathbf{q}, \mathbf{Q}$ - Change in wave vector of the external electron.

q_0 - $(E_f - E_i)/\hbar c_s$ where c_s is the speed of sound (see section 5.3.1).

$\mathbf{r}$, $\mathbf{R}$ - Vector describing the position of the dot electron.

$\mathbf{r}_0$, $\mathbf{R}_0$ - Vector describing the position of the external electron.

s, S - Spin quantum number.

$\boldsymbol{\sigma}$ - Pauli spin matrices.

Bibliography

[1] P. M. Petroff, A. Lorke, A. Imamoglu, Physics Today, **54**, Is. 5, 46, (2001).

[2] P. Auger, J. Phys. Radium, **6**, 205 (1925).

[3] I. N. Stranski, V. L. Krastanow, Akad. Wiss. Lit. Maintz Math.-Natur. Kl. IIb **146**, 797, (1939).

[4] Y. Arakawa, H. Sakaki, Appl. Phys. Lett. **40**, 939, (1982).

[5] U. Bockelmann, G. Bastard, Phys. Rev. B, **42**, 8947, (1990).

[6] H. Benisty, C. M. Sotomayor-Torres, C. Weisbuch, Phys. Rev, B, **44**, 10945, (1991).

[7] B. Ohnesorge, M. Albrecht, J. Oshinowo, A. Forchel, Y. Arakawa, Phys. Rev. B, **54**, 11532, (1996).

[8] D. Morris, N. Perret, S. Farrad, Appl. Phys. Lett., **75**, 3593 (1999).

[9] A. V. Uskov, F. Adler, H. Schweizer, M. H. Pilkuhn, J. Appl. Phys., **81**, 7895, (1997).

[10] R. Ferreira, G. Bastard, Appl. Phys. Lett., **74**, 2818, (1999).

[11] D. Leonard, M. Krishnamurthy, C. M. Reeves, S. P. Denbaars, P. M. Petroff Appl. Phys. Lett. **63**, 3203 (1993).

[12] S. Rumimov, P. Werner, K. Scheerschmidt, U. Gösele, J. Heydenreich, U. Richter. N. N. Ledentsov, M. Grundmann, D. Bimberg, V. M. Ustinov, A. Yu. Egorov, P. S. Kop'ev, Zh. I. Alferov, Phys. Rev. B., **51**, 14766, (1995).

[13] N. Liu, J. Tersoff, O. Baklenov, A. L. Holmes, C. K. Shih, Phys. Rev. Lett. **84** 334, (2000).

[14] D. M. Bruls, J. W. A. M. Vugs, P. M. Koenraad, H. W. M. Salemink, J. H. Wolter, M. Hopkinson, M. S. Skolnick, Fei Long, S. P. A. Gill, Applied Physics Letters, **81**, 1708, (2002).

[15] M. Grumdmann, O. Stier, D. Bimberg, Phys. Rev. B **52** 11969, (1995).

[16] M. A. Cussack, P. R. Briddon, M. Jaros, Phys. Rev. B, **54**, R2300, (1996).

[17] M. Roy, P. A. Maksym, Phys. Rev. B., **68**, 235308, (2003).

[18] L. P. Kouwenhoven, D. G. Austing, S. Tarucha, Rep. Prog. Phys., **64**, 701, (2001).

[19] T. Fujisawa, D. G. Austing, Y. Tokura, Y. Hirayama, S. Tarucha, Nature, **419**, 278, (2002).

[20] T. Fujisawa, D. G. Austing, Y. Tokura, Y. Hirayama, S. Taraucha, Phys. Rev. Lett., **88**, 236802, (2002).

[21] T. Fujisawa, Y. Tokura, Y. Hirayama, Phys. Rev. B, **63**, R81304, (2001).

[22] A. Barenco, C. H. Bennett, R. Cleve, D. P. DiVincenzo, N. Margolus, P. Shor, T. Sleator, J. A. Smolin, H. Weinfurter, Phys. Rev. A, **52**, 3457, (1995).

[23] D. Loss, D. DiVincenzo, Phys. Rev. A, **57**, 120, (1997).

[24] X. Li, Y. Wu, D. G. Steel, D. Gammon, T. H. Stievater, D. S. Katzer, D. Park, C. Piermarocchi, and L. J. Sham, Science, **301**, 809, (2003).

[25] A. V. Khaetskii, Y. V. Nazarov, Phys. Rev. B, **61**, 12639 (1999).

[26] A. V. Khaetskii, Y. V. Nazarov, Physica E, **6**, 470, (2000).

[27] A. V. Khaetskii, Y. V. Nazarov, Phys. Rev. B, **64**, 125316, (2001).

[28] B. Liu, Q. li, Z. Xu, W. E. Ge, J. Phys: Condens. Matter **13** 3923, (2001).

[29] A. I. Ekimov, A. A. Onuschenko, JETP lett., **34**, 345, (1981).

[30] R. Rossetti, L. Brus, J. Phys. Chem. **86**, 4470, (1982).

[31] M. A. Reed, R. T. Bates, K. Bradshaw, W. M. Duncan, W. R. Frensley, J. E. Lee, H. D. Shih, J. Vac. Sci. Technol. B., **4**, 358, (1986).

[32] J. Cibert, P. M. Petroff, G. J. Dolan, S. J. Pearton, A. C. Gossard, J. H. English, Appl. Phys. Lett., **49**, 1275, (1986).

[33] T. P. Smith III, K. Y. Lee, C. M. Knoedler, J. M. Hong, D. P. Kern, Phys. Rev. B, **38**, 2172, (1988).

[34] T. J. Thornton, M. Pepper, H. Ahmed, D. Andrews, G. J. Davies, Phys. Rev. Lett., **56**, 1198, (1986).

[35] U. Meirav, M. A. Kastner, S. J. Wind, Phys. Rev. Lett., **65**, 771, (1990).

[36] Ch. Sikorski, U. Merkt, Phys. Rev. Lett. **62**, 2164, (1989).

[37] T. Demel, D. Heitmann, P. Grambow, K. Ploog, Phys. Rev. Lett. **64**, 788, (1990).

[38] B. Meurer, D. Heitmann, K. Ploog, Phys. Rev. Lett. **68**, 1371, (1992).

[39] R. C. Ashoori, H. L. Stormer, J. S. Weiner, L. N. Pfeifer, S. J. Pearton, K. W. Baldwin, K. West, Phys. Rev. Lett., **68**, 3088, (1992).

[40] S. Tarucha, D. G. Austing, T. Honda, R. J. Van Der Hage, L. P. Kouwenhoven, Phys. Rev. Lett. **77**, 3613, (1996).

[41] D. J Eaglesham, M. Cerullo, Phys. Rev. Lett., **64**, 1943, (1990).

[42] C. W. Snyder, B. G. Orr, D. Kessler, L. M. Sander, Phys. Rev. Lett., **66**, 3032, (1991).

[43] J. Oshinowo, N. Nishioka, S. Ishida, Y. Arakawa, Appl. Phys. Lett. **65**, 1421, (1994).

[44] M. Grundmann, J. Christen, N. N. Ledentsov, J. Böhrer, D. Bimberg, S. S. Ruvimov, P. Werner, U. Richter, U. Gösele, J. Heydenreich, V. M. Ustinov, A. Yu. Egorov, A. E. Zhukov, P. S. Kop'ev, Zh. I. Alferov, Phys. Rev. Lett. **74**, 4043, (1995).

[45] L. Landau, Zeits. F. Phys., **64**, 629, (1930).

[46] V. Fock, Z. Physik, **47**, 1140, (1928).

[47] C. G. Darwin, Proc. Cambridge. Philos. Soc., **27**, 86, (1930).

[48] M. Roy, Private communication.

[49] NAG ltd., Wilkinson House, Jordan Hill Road, Oxford, OX2 8DR, UK. http://www.nag.co.uk

[50] E. E. Vdovin, A. Levin, A. Patane, L. Eaves, P. C. Main. Yu. N. Khanin, Yu. V. Dubrovskii, M. Henini, G. Hill, Science, **290**, 122, (2000).

[51] U. Bockelmann, Phys. Rev. B, **50**, 17271, (1994).

[52] S. Marcinkevičius, A. Gaarder, R. Leon, Phys. Rev. B, **64**, 115307, (2001).

[53] T. Inoshita, H. Sakaki, Phys. Rev. B, **46**, 7260, (1992).

[54] X. Li, H. Nakajyama, Y. Arakawa, Phys. Rev. B, **59** 5069, (1999).

[55] P. Hawker, A. J. Kent, M. Henini, Appl. Phys. Lett., **75**, 3832, (1999).

[56] U, Bockelmann, T. Egeler, Phys. Rev. B., **46**, 15574, (1992).

[57] M. Yukawa, Proc. Phys. Math. Soc. Jpn. **17**, 48 (1935)

[58] W. H. Press, S. A. Teukolsky, W. T. Vetterling, B. P. Flannery, *Numerical Recipes in C* (Cambridge University Press), 1999.

[59] P. W. Fry, I. E. Itskevich, D. J. Mowbray, M. S. Skolnick, J. J. Finley, J. A. Barker, E. P. O'Reilly, L. R. Wilson, I. A. Larkin, P. A. Maksym, M. Hopkinson, M. Al-Khafaji, J. P. R. David, A. G. Cullis, G. Hill, J. C. Clark , Phys. Rev. Lett. **84**, 733 (2000).

[60] J. L. Pan, Phys. Rev. B, **46**, 3977, (1992).

[61] A. Franceschetti, H. Fu, L. W. Wang, A. Zunger, Phys. Rev. B, **60**, 1819, (1998).

[62] L. W. Wang, M. Califano, A. Zunger, A. Franceschetti, Phys. Rev. Lett. **91**, 56404, (2003).

[63] M. Valin-Rodriguez, A. Puente, L. Serra, PRB **66**, 45307, (2002).

[64] M. Valin-Rodriguez, A. Puente, L. Serra, PRB **66**, 165302, (2002).

[65] M. Valin-Rodriguez, A. Puente, L. Serra, E. Lipparini, **66**, 235322, (2003).

[66] M. Valin-Rodriguez, A. Puente, L. Serra, Phys. Rev. B, **69**, 85306 , (2004).

[67] S. Dickman, P. Hawrylak, JETP Lett. **77**, 30, (2003).

[68] M. Florescu, S. Dickman, M. Ciorga, A. Sachrajda, P. Hawrylak, Proceedidngs of the EP2DS-15 conference, Nara, Japan, PA55, p407.

[69] S. E. Laux, D. J. Frank, F. Stern, Surf. Sci. **196**, 101, (1988).

[70] P. A. Maksym, Private communication.

[71] G. E. Pikus, A. N. Titkov, *Optical Orientation*, North Holland (1984).

[72] T. Hassenkam, S. Pedersen, K. Baklanov, A. Kristensen, C. B. Sorensen, P. E. Lindelof, F. G. Pikus, G. E. Pikus, Phys. Rev. B., **55**, 9298, (1997).

[73] B. H. Bransden, C. J. Jochain, *Physics of Atoms and Molecules* ,Longman (1983).

[74] Y. Nishi, Private communication.

[75] C. F. Destefani, Sergio E. Ulloa, G. E Marques, Phys. Rev. B., **69**, 125302, (2004).

[76] J. H. Davies, *The Physics of Low-Dimensional Semiconductors*, Cambridge University Press, (1998).

[77] U. Bockelmann Phys. Rev. B, **48**, 17637, (1993).

[78] A. D. Boardman, D. E. O'Connor, P. A. Young, *Symmetry and its Applications in Science*, McGraw-Hill, (1973).

[79] G. Arfken, *Mathematical Methods For Physicists*, Academic Press, (1985).

[80] P. A. Maksym, unpublished.

[81] A. Bertoni, M. Rontani, G. Goldoni, F. Troiani, E. Molinari, Appl. Phys. Lett., **85**, 4729, (2004).